Kamal Raj Chapagain

Integration of Electronics and Mechanics in Next Generation Ultrasound Transducers in Medical Imaging

Thesis for the degree of Philosophiae Doctor

Trondheim, Mars 2014

Norwegian University of Science and Technology
Faculty of Information Technology,
Mathematics and Electrical Engineering
Department of Electronics and Telecommunications

Abstract

Capacitive micromachined ultrasonic transducer (CMUT) has been emerging technology in the field of medical imaging after its first demonstration in early 90s. CMUTs are fabricated on silicon substrates using micromachining techniques. They can generate high frequencies due to the smaller dimensions feasible with microfabrication. CMUTs for immersion applications could be easily designed to provide fractional bandwidths exceeding 100%. Therefore, they are promising for applications like intravascular ultrasound (IVUS) where high resolution is required at short range. In this domain it may perform better than the existing piezoelectric ultrasound transducers. But there are certain issues that need to be taken care of before they can be used as commercial ultrasound transducers. One is echoes due to the acoustic wave propagation in the silicon substrate, and another is resonances caused by cross coupling between the neighboring elements in the CMUT arrays.

In this thesis we investigate an acoustic backing structure that is to be added on the back side of the CMUT. The backing should absorb incident acoustic waves across a wide frequency band, and it must effectively suppress structural resonances and vibrations. To achieve this, the backing of a CMUT should have an acoustic impedance that matches with the silicon substrate, and it should be lossy. A good candidate for the backing is a tungsten filled epoxy. If the backing structure is thick enough, it will absorb the acoustic wave reflected back to the transducer and thus will remove any trailing echoes. In many cases the transducer is intended for applications where there is little room for a thick backing. Various approaches has been suggested to reduce the extra volume and weight added by a thick absorbing backing, one approach is to use a grooved backing structure. The grooves at the bottom of the backing provide an extra attenuation by scattering the waves in different directions so that a thinner backing would be sufficient. The scattering removes power from the specular reflection from the back surface which otherwise degrades the image quality. It has

been shown that this type of structure reduces the specular reflection for a range of frequencies. When CMUTs are used in practical applications, the propagation of waves from a fluid medium into the backing or vice versa is blocked to some degree by total reflection, except for a range of steering angles around broadside. This is due to the difference in acoustic velocities of silicon and the fluid medium. This blocking is accompanied by the generation of surface waves in the silicon substrate, which also may impact the imaging and therefore must be controlled. In the present work we investigate the acoustic signal transmitted into the backing relative to the signal transmitted into the fluid medium when CMUT arrays on top of the silicon substrate are excited. This gives us an estimation of how much attenuation is needed from the acoustic backing layer.

The purpose of the grooves on the backing structure is to provide an attenuation due to scattering which is in addition to the absorption loss in the epoxy tungsten composite. Experiments performed on the grooved backing structures show that such structures provide a satisfactory performance for the waves traveling normal to the bottom of the backing structure. But the acoustic waves propagating into the backing structure may not always be normal to the bottom of the structure. Therefore, the performance of the grooved backing structure is also studied for the waves traveling in oblique directions to the bottom surface of the backing. From our simulations we know that the performance of grooved structures for oblique incidence is not significantly different from that of normal incidence when the incident angle is within $\pm 30°$ to the surface normal to the bottom of the structure. We have also shown that for a CMUT-backing stack immersed in a fluid medium, waves that reach into the backing from the fluid medium with significant power mostly lie within this range of angles. It means that a CMUT transducer with grooved backing structure always provide extra attenuation for the waves propagating into the substrates when it is used in practical applications.

In this work we have also investigated acoustic properties of some polymers. The polymers, RTV 615 and Sylgard 160, have acoustic properties such that a thin layer of these polymers could be used to minimize the acoustic cross coupling in the CMUT arrays significantly. These materials could also be used as lens material for CMUT transducers together with stiff polymers such as TPX.

Preface

This thesis is written as part of the PhD programme at the Norwegian University of Science and Technology (NTNU). This work was supported by BONDCMUT project (171099/V30) of the Research Council of Norway. This work was carried out at Department of Electronics and Telecommunications with professor emeritus Arne Rønnekleiv as main supervisor and professor Dag T. Wang as co-supervisor.

Panthi and their families. Thank you for nice time throughout the years.

Finally, and most of all, I would like to thank my family for their support and help throughout life; they never failed in encouraging me. Special thanks to my wife Anita for always being patient and being there for me during these years of hard work. I could not have done this without you.

Kamal Raj Chapagain,
September 2013.
Trondheim, Norway

List of papers

1. **Minimizing the bottom reflection in Ultrasonic CMUT Transducer backing using low profile structuring**

   Kamal Raj Chapagain and Arne Rønnekleiv

   Proceedings of IEEE Ultrasonics Symposium 2009, Rome, Italy, September 20-23, pages 430-433

2. **Measurement of the loss due to grooved bottom structure intended for use as a backing in Capacitive Micromachined Ultrasonic Transducers**

   Kamal Raj Chapagain and Arne Rønnekleiv

   Proceedings of 34th Scandinavian Acoustics Symposium 2011, Geilo, Norway, 20 January -2 February

3. **Measurement of the added specular reflection attenuation by using a grooved bottom surface in the backing of CMUTs**

   Kamal Raj Chapagain and Arne Rønnekleiv

   Proceedings of IEEE Ultrasonics Symposium 2011, Orlando, Florida, USA, October 18-21, pages 1004-1007

4. **Grooved Backing Structure for CMUTs**

   Kamal Raj Chapagain and Arne Rønnekleiv

   IEEE Transactions on Ultrasonics, Ferroelectrics and Frequency control, Volume 60, Issue 11, November 2013, pages 2440-2452

Author's contribution

All the papers included in this work were written by the author. The simulations and the measurements presented in this thesis were performed by the author. The only exceptions are the anisotropic etching and the polymer deposition on the silicon wafers described in Chapter 6, which was performed by research scientist Jon Due Hansen at SINTEF MiNaLab in Oslo.

Contents

List of Figures

List of Tables

List of Abbreviations

CMUT	Capacitive Micromachined Ultrasonic Transducer
CT	Computed Tomography
DRIE	Deep Reactive Ion Etching
EDM	Electric Discharge Machining
FEM	Finite Element Method
IVUS	Intravascular Ultrasound
LAM	Laser Assisted Machining
LPCVD	Low Pressure Chemical Vapor Deposition
MEMS	Microelectromechanical System
MRI	Magnetic Resonance Imaging
NDT	Non Destructive Testing
OCT	Optical Coherence Tomography
PECVD	Plasma Enhanced Chemical Vapor Deposition
PET	Positron Emission Tomography
PML	Perfectly Matched Layer
PZT	Lead Zirconate Titanate
SAW	Surface Acoustic Wave
SOI	Silicon On Insulator
TMAH	Tetramethyl Ammonium Hydroxide

Part I

Overview

Chapter 1

Motivation

Medical diagnosis is a process of identifying nature and extent of an illness or a disease. Different diagnostic procedures have been used for many centuries by our ancestors for this purpose. Due to rapid development in electronics and availability of a large variety of diagnostic tools, health care professionals today are able to narrow down the original diagnosis to a specific level more quickly and easily than before. Ultrasonic imaging is one of the important and widely used medical diagnostic tools we have today. Ultrasound refers to the sound waves that have frequencies above human hearing range, which is about 20 kHz. Medical diagnostic ultrasound usually operates in the frequency range from 2-15 MHz and can resolve objects of millimeter size. Higher frequencies (30 MHz and beyond) have also been used in specific applications, and may provide even better resolution.

1.1   Lateral resolution and axial resolution

The spatial resolution of an ultrasound imaging system is the ability of the ultrasound beam to distinguish between two points in space. The axial resolution is along the ultrasound beam and, is determined by the pulse duration or the bandwidth of the transducer. For a fixed number of cycles per pulse, an increase in frequency would reduce the pulse duration and hence improve the axial resolution of the system.

The lateral resolution, on the other hand, is along the direction that is perpendicular to the central portion of the ultrasound beam. It is determined by the product of the wavelength and the f-number of the transducer, f-number being the ratio of the focal distance to the transducer diameter. For example, with a conventional ultrasonic imaging frequency of 3 MHz, a transducer with f-number 2.5 can resolve objects of the order of 1 mm.

If the frequency is increased to 30 MHz, the lateral resolution improves to one tenth. But the penetration depth will be smaller as the acoustic attenuation in most materials increases with the frequency. This means that the resolution of an ultrasound imaging system can be improved with the high frequency and wide bandwidth transducers with expense of the penetration depth.

1.2   High frequency ultrasound imaging

High frequency ultrasound transducers are useful in applications where the penetration depth is limited but high resolution is needed. Although technologies like magnetic resonance imaging (MRI), computed tomography (CT), and positron emission tomography-computed tomography (PET-CT) exist for high resolution imaging, ultrasound imaging offers low cost and better portability compared to these technologies.

Typical high frequency imaging applications includes eye imaging, skin imaging, catheter based intravascular imaging, high frequency flow imaging, and imaging of small animals [LTCF96].

High frequency (HF) ultrasound imaging is very useful to get high resolution images of blood vessels. Among the blood vessels, coronary arteries are of high importance as they deliver oxygen rich blood to the heart muscle. Coronary artery disease is usually caused by the formation of atherosclerotic plaques in the coronary arteries. The vulnerable plaque, which is at increased risk of rupture, may trigger blood clots and block the blood flow. Most heart attacks and strokes are caused by ruptured plaques [Sto04]. The most commonly used imaging technique to visualize the blood in the coronary artery is angiography which is based on x-ray and contrast agents. The image resolution of such a system is not very high. But a major drawback is difficulty in visualizing the plaques, which may be improved by the use of high frequency ultrasound imaging. The acoustic attenuation in human tissues is very high at high frequencies, therefore the transducer needs to be very close to the plaque to get satisfactory images of the artery. The transducer can be guided to the blood vessel with the help of a catheter through the vascular system for this purpose. This is called intravascular ultrasound imaging (IVUS). Catheter based intravascular imaging with frequencies higher than 20 MHz is used to characterize the artery wall geometry, and presence and distribution of the atherosclerotic plaques [PBG+90]. It has also been used to guide stent placement and in angioplastic procedures.

HF ultrasound imaging can also provide high resolution images of skin

tumors and allow noninvasive measurements of skin thickness with much greater accuracy than existing technology. This could also reduce the number of biopsies needed in this group of patients. HF ultrasound imaging also has a potential to visualize cartilage with high resolution which could be helpful in the patients suffering from osteoarthritis [Iag10]. Osteoarthritis is a degenerative arthritis which is associated with the abnormalities of joints.

HF ultrasound imaging is also useful is eye imaging. In the human eye, all clinically important tissues lies within a few millimeters of the surface which makes high frequency ultrasound imaging very suitable for those applications.

Beside these, HF ultrasound can be used in imaging of small animals. Small animals like mice and zebra-fish could be used as the animal model to study and to understand the function of many genes that are important for embryonic developments of mammals [LTCF96]. This could also be useful in preclinical imaging, for instance within cancer research.

Optical coherence tomography (OCT) is an emerging technology for high resolution imaging. It uses near infrared light instead of sound. It offers lateral resolution which is comparable to IVUS, but the penetration depth may be somewhat lower. Recently this technology has been used for high resolution imaging of coronary arteries [BCG$^+$09]. An important limitation of OCT in such applications is the limited precision in discriminating the different kind of tissues [BAS$^+$13]. Also unlike IVUS, OCT is obstructed by blood.

1.3 Choice of ultrasound transducers

The development of high frequency ultrasound imaging depends on the availability of high frequency transducers. The characteristics of the transducers determine the image quality. Current HF ultrasound imaging devices, also known as ultrasonic biomicroscopes, use mechanically scanned single element transducers which has a poor resolution and can only achieve a frame rate of 30 frames/second [Shu09]. These problems can be solved by using HF linear array technology which can be focused electronically. Such HF transducers should have a large bandwidth to improve the axial resolution of the system. Piezoelectric polymer (PVDF) transducer operating at frequencies around 50 MHz or more has been fabricated with a 6 dB bandwidth of 60-80% [LTCF96]. These transducers have been used for skin and eye imaging. But due to the low dielectric constant of polymer transducers, they are unsuitable for intravascular imaging, where the transducer area must be small. This is due to electrical impedance mismatch of PVDF

to the cable and electronics which limits the output pressure and signal to noise ratio (SNR). PZT (Lead Zirconate Titanate) ceramics could be an alternative for such polymer transducers as the dielectric constant of PZT is much higher than that of PVDF. But it is a challenging task to manufacture high frequency PZT transducers with sub-wavelength element dimensions [SCZ07].

Capacitive transducer, also known as capacitive micromachined ultrasonic transducers (CMUT), is an alternative for such imaging applications [YOE+05] [DGK06]. As the CMUT is based on micromachining of silicon, it may be easier to manufacture transducers with small sizes that can operate at high frequencies. Also this technology may offer two dimensional arrays with several thousand elements, and thus it may more rapidly take advantage of future wafer bonding techniques in development by the microelectronics industry. CMUT transducers with fractional bandwidth of more than 100% can be made to improve the axial resolution of the imaging system. Due to use of a vacuum cavity and a thin membrane in a CMUT transducer, it can be designed with a low acoustic impedance that matches with the operating medium. This makes CMUT transducers attractive for future high frequency ultrasound imaging applications.

Chapter 2

CMUT: An Introduction

2.1 History

Modern acoustics started with the famous publication, *The Theory of sound*, by Lord Rayleigh and with the discovery of the piezoelectric effect by the Curie brothers, both around 1870. Lewis Richardson and Alexander Behm first proposed the use of sound waves for the detection of icebergs after the Titanic disaster, but it was not until World War I that it was realized in practice to detect submarines by the French scientist Paul Langevin [EFJ74]. This was the foundation of the SONAR (Sound Navigation and Ranging) technology. The technology was not used for medical applications then as it was difficult to get frequencies above 100 kHz. Piezocrystals like quartz were good candidates for generating higher frequencies, but the electromechanical coupling was weak thus making them unsuitable. With the discovery of the ceramic piezoelectric material Barium Titanate in 1947, stronger electromechanical coupling was obtainable. This technology, initially used for non-destructive testing (NDT) of materials, subsequently paved the way for medical diagnostic applications of ultrasound. In the early 50s use of ultrasound for medical application was focused on therapy and high intensity applications like tissue heating. Although the basic principles of ultrasound for medical application were demonstrated in the 50s and 60s, the first useful instrumentation becomes available in the 70s with the development in electronics and integrated circuits. Since then, there have been rapid developments in medical ultrasonics [Ang96] [EYOKY06].

Although the piezocrystals and piezoceramics have always been a popular choice for generation and detection of ultrasound, magnetostrictive and electrostatic techniques have been used for some time. The main reason piezoelectric transducers were more popular was due to its high electrome-

chanical coupling coefficient and its high permittivity which eased electrical match. Electrostatic capacitors have also been used as receivers for audio applications, but for a long time they were not used in medical applications as such applications also need a transmitter. Electrostatic transducers need a very high electric field for their operation, which has been the limitation for many decades. But due to the recent development in microfabrication techniques, sub-micron gap heights are possible to fabricate. This opened the door for CMUT transducers in ultrasound applications [HKY94][SLA$^+$96][LJS$^+$98].

The CMUT transducers promise some advantages compared to piezoelectric transducers. It may potentially become a low cost technology as it is a batch fabrication process based on micromachining of silicon. This makes it easy to create large 1-D or 2-D arrays using this technology. It is also easy to fabricate CMUTs that offer high bandwidths which makes them useful in applications requiring good axial resolution. Due to the smaller dimension feasible with microfabrication, it could generate high frequencies, which is desirable in applications like intravascular ultrasound. And thanks to its fabrication process, it may be easier to integrate with electronics [DWB$^+$05][MRW06].

2.2 Introduction

The operating principle of CMUT is based on electrostatic transduction. The transduction element is a parallel plate capacitor which consists of a thin membrane suspended over a vacuum cavity. A conducting layer in the membrane acts as one electrode whereas a properly doped silicon substrate acts as the other electrode. When the capacitor is biased with a DC voltage, the electrostatic force attracts the membrane to the substrate. The mechanical tension due to stiffness of the membrane acts as a restoring force. There is an essential difference between the vibration of a membrane and a thin plate. In a membrane, the restoring force is entirely due to the tension applied to the membrane, whereas it is mainly due to the stiffness in a thin plate [KFCS00]. In this sense, a membrane is considered to be a special case of the thin plate when the thickness of the plate is very small compared to its lateral dimensions. Even though we have considered the stiffness together with the tension in our case, we have used the term membrane instead of thin plate throughout this work.

If an alternating voltage is applied to such a biased capacitor, ultrasonic waves are generated from the vibration of the membrane. Such a CMUT structure in transmitting mode is shown in Figure 2.1. On the other hand,

if acoustic pressure waves are incident upon a biased capacitor like this, the membrane is displaced and the capacitance of the device changes. This gives rise to a current which could easily be detected, hence the CMUT operates as a receiver.
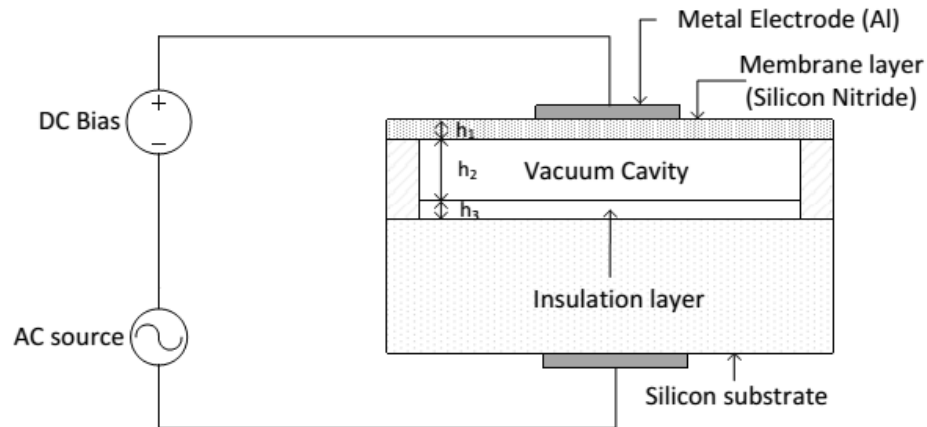
Figure 2.1: Simple CMUT structure in a transmitting mode, with silicon nitride as a membrane layer, aluminum as top electrode and silicon substrate as bottom electrode.

Although the structure is a parallel plate capacitor, it could not simply be represented by a parallel plate capacitor as the membrane is supported at all the sides by a supportive structure. The behavior of the membrane becomes complex with the application of voltage. For a proper understanding of such devices, finite element analysis may be performed. But FEM modeling with high precision can be time consuming, so there exists different models for CMUTs which analyze the operation in a simpler way and which can be used for transducer design. This will be discussed in the following section in more detail. The frequency of operation of a CMUT is determined by its dimension, the shape and the stiffness of the membrane. It also depends on the height of the vacuum cavity, the thickness and properties of insulating layer, and the bias voltage applied to it. A CMUT transducer normally consists of an array of many CMUT cells; the actual response is, therefore, due to all the capacitors in combination. Due to the use of vacuum gap in the design and the thin membrane on top of it, a CMUT could easily be designed with its acoustic impedance closer to that of a gaseous medium. When such devices are used in immersion, the acoustic impedance

becomes smaller than the loading impedance over a wide frequency range, resulting in broadband operation. This is one of the main advantages of using CMUT transducers. There exist different methods for the fabrication of CMUTs, such as the sacrificial release process on a solid substrate, and the wafer bonding process. These processes will be discussed in more detail in Section 2.4.

2.3   CMUT modeling

A transducer that converts energy between the electrical and the mechanical domain can be represented as a *two-port network* with one electrical port and one acoustic port. This is shown in Figure 2.2. The different parameters of the two port network are defined as

$V =$ the voltage across the electrical inputs to the transducer,

$I =$ the current at the electrical inputs,

$F =$ the force on the radiating surface,

$u =$ the speed of the radiating surface,

where all these parameters are root mean square (rms) quantities.

Since electrostatic transducers are reciprocal transducers, the *canonical equations* for the electromechanical behavior of such a transducer are given by the following equations [KFCS00]:

$$
\begin{aligned}
V &= Z_{EB}I + \phi Z_{EB}u \quad , \\
F &= \phi Z_{EB}I + Z_{mo}u \quad ,
\end{aligned}
\tag{2.1}
$$

where

$\phi =$ Transformation factor,

$Z_{EB} =$ Blocked electrical impedance $(u = 0)$,

$Z_{mo} =$ Open circuit mechanical impedance $(I = 0)$,

$Z_{ms} = Z_{mo} - \phi^2 Z_{EB} =$ Short circuit mechanical impedance $(V = 0)$.

CMUTs are modeled in a similar fashion as other transducers. Mason's model for capacitive transducers which, with some restrictions, is valid for small signal conditions, is widely used for the modeling of CMUTs. Since the model is one dimensional, a requirement for a Mason's model to be valid is that the shape of the membrane deflection does not change. Based

Figure 2.2: Electrostatic transducer modelled as a two-port network.

on Mason's model, various models have been published. Khuri-Yakub *et al.* [EYOKY06] have developed a simple model of a CMUT with a circular membrane while Ladabaum *et al.* [LJS+98] considered a plate in tension model for the CMUT membrane. The major source of loss in a CMUT is due to acoustic radiation of waves into the medium of interest and acoustic loss in the substrates. However, there are some additional losses such as squeeze film gas damping, heating of part of the CMUT due to deformation, and subsequent heat conduction, including heat loss due to conduction from the compression of gas in the cavity. There will also be losses at the CMUT-fluid interface due to viscosity in the fluid. The models mentioned earlier do not account for these additional losses. Caliano *et al.* [CFM+06] have developed an improved model including some of these factors and an even more accurate models for CMUTs have been developed by Rønnekleiv *et al.* [RLJEY97].

The CMUT model presented in this work is largely based on the model of a CMUT array developed by Rønnekleiv [Røn05]. This model describes the CMUT through its free acoustic vibration modes, assuming no direct coupling between individual CMUTs. It combines free acoustic modes of the CMUT membrane with self and mutual acoustic impedances that gives coupling between these modes due to the fluid medium [Røn08]. The calculation is done in the spatial Fourier domain. The CMUTs are assumed to be arranged in an infinite periodic pattern of rectangular cells in x and y directions. The advantage of using spatial Fourier domain is that we need to calculate self/mutual impedance between the modes in only one period of the structure, for each frequency and k-vector in the excitation. To describe an excitation over a finite region of the array, a large range of k-vectors must be included. However, this could be made computationally efficient by interpolating parameters in frequency and k-vectors. Another

feature of the analysis is that the losses in the CMUT-fluid interface may easily be included. Due to the viscosity of the fluid, not all the power received by CMUTs is radiated into the fluid. The viscosity of the fluid modifies the tension on the membrane surface, which will also change the self and mutual coupling impedances of the modes.

To make the calculations simpler, CMUTs are assumed to be circular with a thin metalized electrode on top of it. The different acoustic vibrational modes for CMUTs are calculated using a simple plate theory. The radial mode profiles for a vibrating circular membrane with fixed rim for different modes are shown schematically in Figure 2.3. The vibration modes of interest here are the modes with vertical deflection (z-direction here) of the membrane as only these modes will couple to the fluid. These modes also have the lowest resonance frequencies as the membrane is usually thin. The following assumptions are made for the modeling of CMUT arrays using this method:

- The bottom surface and the membrane support structure are both stiff.

- CMUTs loaded with a fluid are operated in a linear regime, meaning that vibration amplitudes are small.

- CMUTs are biased with hydrostatic pressure and electrostatic force due to a fixed DC electric bias.

The forces acting on the membrane give a small signal deflection profile of the membrane in mode n, denoted by $w_n(x, y)$ which is normalized to have a peak amplitude of one (dimensionless). The electrostatic forces on the membrane are derived using a small signal capacitance of the CMUT, C_m, which is given by parallel plate approximation as

$$C_m = \int_{electr.} \frac{\epsilon_0 dA}{\sum \frac{h_i}{\epsilon_r{}^{(i)}} - w_0} \quad , \qquad (2.2)$$

where h_i is the height of the layer i with relative permittivity $\epsilon_r^{(i)}$ in the undeflected case, w_0 is the static deflection of the membrane and integration is taken over the extent of the overlapping capacitor electrodes. The different layers mentioned here are membrane, vacuum cavity, and insulation layer which can be seen in Figure 2.1 for a simple CMUT structure.

As explained earlier, for small deflections, the operation of CMUT will be linear and it will have a number of vibrational eigenmodes. These eigenmodes of particle displacement are orthogonal for loss-less materials in the
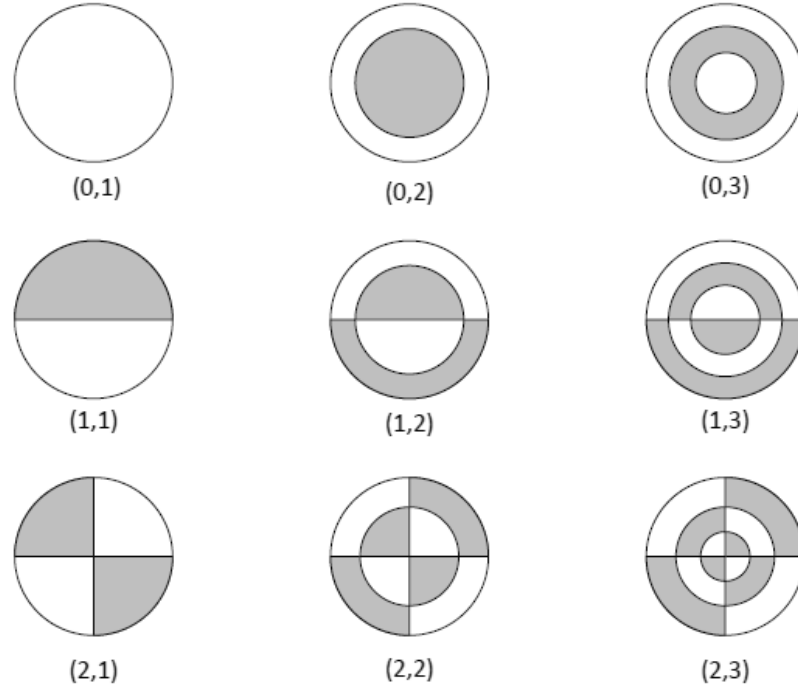
Figure 2.3: Vibrational modes of a circular membrane with a fixed rim, defined by (m,n) where m determines the radial nodal lines and n determines the number of nodal circles, from [KFCS00]. The shaded areas denotes sections of the membrane that vibrates 180° out of phase with the unshaded areas.

structure and they have different resonant frequencies. Only with degeneration is there a choice in the mode shapes, and then they should be chosen orthogonal. The modes m and n are orthogonal meaning that the force corresponding to eigenmode n will not do any work when acting on a displacement of mode m when integrated over the total volume of the structure. This gives the possibility to define effective forces on different modes from a given force field. This also gives effective membrane masses and stiffness for the modes as described in more detail in [Røn05].

Electrical forces are developed due to small signal voltages as well as due to small signal deflections. The effective force on mode n from a small signal voltage v is written as $vK_n^{(v)}$. If W_m is a scalar peak amplitude of the deflection in mode m, the effective force on mode n from a small signal

deflection $w_m W_m$ is written as $W_m K_{n,m}^{(w)}$. Here m may be different from n. This gives the values for $K_n^{(v)}$ and $K_{n,m}^{(w)}$ as:

$$K_n^{(v)} = \int_{electr.} \frac{\epsilon_0 V_0 w_n dA}{\left(\sum \frac{h_i}{\epsilon_r^{(i)}} - w_0 \right)^2} \quad , \qquad (2.3)$$

$$K_{n,m}^{(w)} = \int_{electr.} \frac{\epsilon_0 V_0^2 w_n w_m dA}{\left(\sum \frac{h_i}{\epsilon_r^{(i)}} - w_0 \right)^3} \quad . \qquad (2.4)$$

From equation (2.4), it is clear that $K_{n,m}^{(w)}$ is symmetric with respect to integers m and n. As the value of $K_{n,m}^{(w)}$ is different from zero in general, we may get coupling between different free acoustic modes in the membrane due to the electrostatic forces caused by membrane deflections.

In the analysis, all modes of all the CMUTs within one element is taken as a set of orthogonal modes without fluid loading, and then the coupling between all the modes due to the output pressures in the fluid is calculated. Consider a case when all CMUTs within an element number (n_x, n_y) are excited by a periodic excitation voltage, $v(n_x, n_y) = v_0 exp(-jK_x L_x n_x - jK_y L_y n_y)$, where K_x and K_y are k-vectors along the array surface, L_x and L_y are the periods in x and y directions of the structure and v_0 is a constant voltage with time dependence $e^{j\omega t}$. For this periodic structure with periodic excitations, all equal CMUT modes n with the same relative position within the elements (referred to as a *collective mode* in this work), will have membrane velocities $v_n(n_x, n_y)$ with the same change from element to element. The excitation is given by

$$v_n(n_x, n_y) = v_{n,0} exp(-jK_x L_x n_x - jK_y L_y n_y) \quad , \qquad (2.5)$$

where $v_{n,0}$ is a constant. To determine the velocities $v_{n,0}$ for all modes within the element, the pressures on the membrane surface from the liquid due to the velocities of (2.5), the excited collective mode, need to be calculated. The equations used to calculate the pressure in the plane wave in the fluid with k-vector components K_x and K_y along the array surface is described in [Røn05]. This pressure gives the self and the mutual coupling impedances, $Z_{m,n}^{(me)}$ for equivalent force on mode m from velocity in mode n, valid for a periodic excitation given in (2.5). These impedances are found by integrating the surface pressure from mode n times the deflection profile of mode m over the element surface as

$$Z_{m,n}^{(me)} = \frac{1}{j\omega W_n} \int_{electr} t_{zz,n}^{(me)} w_m dA \quad , \qquad (2.6)$$

where $j\omega W_n w_n$ is the small signal velocity of the membrane that leads to a normal tension $t_{zz,n}^{(me)}(x,y)$ on the membrane surface. As the normal tension defined in equation (2.6) changes if the viscosity of the fluid is taken into account, the self and mutual coupling impedances also depend on the viscosity of the fluid medium [Røn08]. This leads to a matrix representation of the equation for the excitation amplitudes W_n of the acoustic eigenmodes of the membrane in response to an applied small signal voltage, v, as follows:

$$[diag(M_n(w_n^2 - w^2)) - K_{n,m}^{(w)} + j\omega Z_{m,n}^{(me)}]W_n = vK_n^{(v)} \quad , \qquad (2.7)$$

where M_n is the effective mass of eigenmode n.

To complete the equations for the CMUT, the electric current is calculated in terms of voltage v and the amplitudes W_n. For this, we need the derivative of the membrane capacitance with respect to amplitude W_n of the various modes of the membrane. The current i into the membrane capacitor can be found as the time derivative of the charge on the CMUT capacitor, $i = \dfrac{dQ}{dt} = \dfrac{d}{dt}(C_m(v + V_0))$ giving

$$i = j\omega C_m v + j\omega \sum_n W_n K_n^{(v)} \quad . \qquad (2.8)$$

Because the membrane mode excitation amplitudes determined from equation (2.7) are proportional to the voltage v, equations (2.7) and (2.8) together determine the CMUT admittance.

2.3.1 Equivalent circuit of a CMUT

Equations (2.7) and (2.8) are the basis for the equivalent circuit of a CMUT. In the following calculation, a CMUT membrane deflected in only one mode, denoted by n here, is considered. The different forces acting in this case are defined as follows:

The effective force that is required to accelerate the membrane for this mode is given by

$$F_{eff,a} = M_n \ddot{W}_n \quad , \qquad (2.9)$$

where M_n is the effective mass, and $\ddot{W}_n$ gives the particle acceleration of the n-th mode.

Electrical forces are developed from the small signal voltage, v, as well as from the small signal deflection, w, denoted by $F_{eff,qv}$ and $F_{eff,qw}$ and are given respectively by $vK_n^{(v)}$ and $W_n K_n^{(w)}$. The values of $K_n^{(v)}$ and $K_n^{(w)}$ are the same as given by equations (2.3) and (2.4), except that there is only one active mode.

If the membrane is driving a fluid as a transmitter, the effective force due to pressure on the membrane at a given frequency is given by

$$F_{eff,p} = -Z_a \dot{W}_n \quad , \tag{2.10}$$

where Z_a is the acoustic impedance of the mode it couples to, which, in most of the cases, is the radiation impedance including a reactance from moving fluid mass, and the effect of losses at the CMUT fluid interface.

For a given deflection, there is an elastic restoring force that will attempt to pull the membrane back to the equilibrium position, which is given by

$$F_{eff,res} = -W_n F_s \quad , \tag{2.11}$$

where F_s is an equivalent spring constant of the mode. It is given by $M_n \omega_{on}^2$, ω_{on} being unloaded resonance frequency of the particular mode.

The force balance equation of the membrane for this mode is thus given by:

$$F_{eff,a} = F_{eff,p} + F_{eff,qv} + F_{eff,qw} + F_{eff,res} \quad ,$$
$$-\omega^2 M_n W_n = -j\omega Z_a W_n + W_n K_n^{(w)} + v K_n^{(v)} - W_n F_s \quad . \tag{2.12}$$

The equation (2.12) is, in fact, equation (2.7) reduced to a single mode. The current flowing through the device in this case is given by

$$i = \frac{dQ}{dt} = j\omega C_m v + V_0 \frac{dC_m}{dW_n} j\omega W_n = j\omega C_m v + j\omega K_n^{(v)} W_n \quad , \tag{2.13}$$

where $\frac{dC_m}{dW_n}$ is calculated to be $\frac{K_n^{(v)}}{V_0}$ using equation (2.3).

Combining equations (2.12) and (2.13), the electrical admittance of the CMUT for the n-th mode may be written as:

$$Y(\omega) = \frac{i}{v} = j\omega C_m + \frac{K_n^{(v)2}}{Re(Z_a) + j\omega M_n + jIm(Z_a) + \frac{1}{j\omega}(F_s - K_n^{(w)})} \quad . \tag{2.14}$$

From equation (2.14), we derive the equivalent circuit of the CMUT as shown in Figure 2.4. Since the CMUT is a reciprocal transducer, only the transmitting circuit is shown in the figure. The notations used in the equivalent circuit is based on the two port model of the electrostatic transducer described earlier in this section. The blocked impedance Z_{EB} includes not
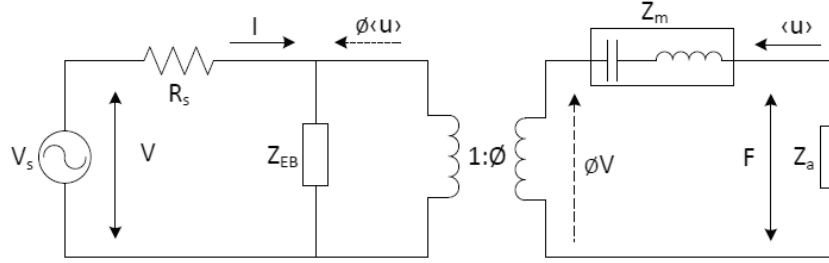
Figure 2.4: CMUT equivalent circuit for transmission of acoustic signal.

only the CMUT capacitance, C_m, but also a bias resistor, a parasitic capacitance and a loss resistor which is due to current flow in the device. The membrane motion is determined by the transformation factor ϕ, which in this model is given by the factor $K_n^{(v)}$. Z_m is the acoustic impedance of the mode and Z_a is the acoustic impedance the mode couples to. Z_m also includes the spring softening of the membrane due to electrostatic coupling given by the factor, $K_n^{(w)}$. In fact, Z_m is equal to $j\omega M_n + \dfrac{1}{j\omega}(F_s - K_n^{(w)})$. Here the first term, $j\omega M_n$, is the inertia force caused by the acceleration of the membrane mass, and the second term, $\dfrac{1}{j\omega}(F_s - K_n^{(w)})$, is the restoring force composed of the mechanical stiffness reduced by the electrostatic softening. The impedances Z_m and Z_a are connected in series in the equivalent circuit since they both give forces that are proportional to the velocity of the membrane, and their sum acts on the membrane. This also means that zero impedance is avoided when the model is used in air or vacuum. From the equivalent circuit, it is clear that the operation of the transducer for immersion application would normally be broadband as the acoustic impedance of the load, Z_a, could easily be made higher than the acoustic impedance of the membrane, Z_m, over a large bandwidth for reasonably designed CMUTs.

For the modeling of CMUTs with complex geometries, finite element analysis is required as it is otherwise difficult to define the vibration modes needed for the analysis of such CMUTs. Parameters obtained using finite element analysis could then be used for the analytical model presented in this section.

2.4 Fabrication technologies

Because CMUTs utilize microelectromechanical systems (MEMS) technology, most of the processes used for fabrication of MEMS devices could also be adapted to the fabrication of CMUTs. One such process used is bulk micromachining where the bulk of a substrate is removed in order to create microstructures. Another method is surface micromachining where the microstructures are created near the surface of the substrate. Most commonly used standard in surface micromachining is the sacrificial release (etching) process. For the fabrication of CMUTs, surface micromachining was mostly used until the wafer bonding process for fabricating CMUTs was demonstrated. In this section we describe different techniques used to fabricate CMUTs.

2.4.1 Sacrificial release process

The fabrication of CMUTs using surface micromachining was first demonstrated at Stanford University [LKYSH95], and since then this method was dominant for more than a decade. The basic principle is to form a cavity underneath a thin membrane by depositing a sacrificial layer on the carrier substrate and selectively remove the layer by using an etchant. The etchant material is chosen such that it removes the sacrificial layer but not the membrane layer or the other layers. Different materials can be used as substrate, membrane and sacrificial layer, but low pressure chemical vapor deposition (LPCVD) poly-silicon as a sacrificial layer and silicon nitride as a membrane layer has been a popular choice while properly doped silicon is usually chosen as a substrate.

The method described here is based on the fabrication steps used in [LJS$^+$98] and [EYOKY06]. The process starts with a silicon wafer which when appropriately doped acts as a conductor and is used as a bottom electrode for the CMUTs. LPCVD silicon nitride is deposited to form an etch stop layer which prevents the etching of the silicon wafer during the membrane release process. A layer of LPCVD poly-silicon is deposited and patterned to define the cavity, the membrane shape, and the etch channels. Etch channels are used so that the etchants flow through it during membrane release. If these channels are properly designed, the cavity size will not change during the sealing process. The membrane can be of any shape but circular and hexagonal shapes are widely used. The parameters like shape and size are very important as they are critical in determining the frequency response of such devices.

A LPCVD silicon nitride is then deposited which is used as a membrane.
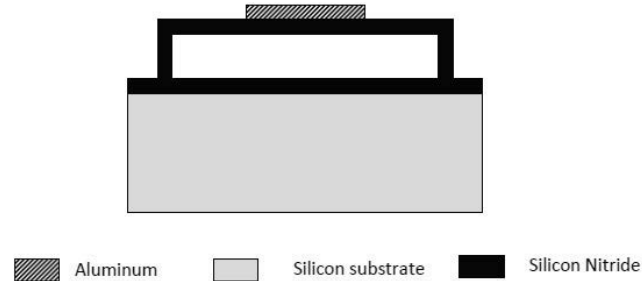
Figure 2.5: Sacrificial release process for the fabrication of CMUT showing the cross section of the final CMUT.

As there will be one more deposition of such a layer to seal the cavity after the membrane release process, the nitride deposited at this step will not define the final membrane thickness. This first layer is patterned to create small holes which is used to etch the sacrificial layer using wet etching. The choice of etchants would again depend on the sacrificial layer used beneath the membrane. In this particular case, potassium hydroxide (KOH) is used to etch the LPCVD poly-silicon layer. The etched holes are then sealed by another layer of LPCVD silicon nitride. The final step would then be providing electrical connections for top and bottom electrodes which is done by sputtering of aluminum, patterning with lithography followed by wet etching.

Some versions of this fabrication process also use through-wafer via interconnections from the front side of the substrate to the backside, for which deep reactive ion etching (DRIE) is used to get high aspect ratio vias in silicon [EYOKY06].

The sacrificial release method has been used for a long time, but the drawback of this method is poor control over the uniformity, thickness and material properties of the deposited layers. Slow sacrificial layer etching and unwanted material deposition on the faces of the gap make it difficult to control the gap height [HEH+03]. Also etch holes used in this process utilize large area between the adjacent membranes which limit the active cells per unit area, reducing the *fill factor* which is an important property that affects the radiation impedance and the efficiency of the transducers [CFM+06].

2.4.2 Wafer bonding process

Wafer bonding processes have also been used in the fabrication of CMUTs along with the surface micromachining process. There are three basic wafer bonding techniques: anodic bonding, fusion bonding, and adhesive bonding. Silicon fusion bonding is used for the fabrication of CMUTs since this is a stable process and it is easier to fabricate complex structures from single crystal silicon. Compared to the sacrificial release process, the process control and repeatability is improved with this method.

The method described here is based on the fabrication steps used in [HEH$^+$03] and [MRW06]. The wafer bonding starts with two wafers: a prime quality silicon wafer and a silicon-on-insulator (SOI) wafer. Before bonding, both top and bottom wafers are prepared separately. A thin silicon dioxide layer is thermally grown on the top wafer before an additional layer of silicon nitride is deposited by LPCVD. Cavities are etched on the bottom silicon wafer by Reactive Ion Etching (RIE). After standard wafer cleaning steps, the two wafers are brought together in vacuum and annealed at high temperature (1100°C) to form strong covalent bonds. After bond annealing, a thick silicon oxide is grown on the bottom silicon wafer to protect the wafer during etching of the prime wafer, leaving a nitride membrane with oxide suspended over the etched cavities. The thick silicon oxide is removed and the nitride membrane is finally exposed after patterning and etching of the thin oxide layer. A metal layer is then deposited using sputtering of aluminum and patterned for electrical connections.
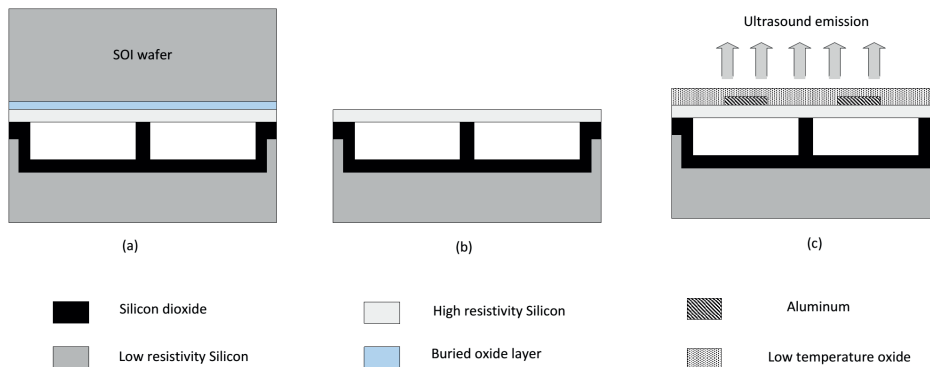
Figure 2.6: Wafer bonding process for CMUT based on [HEH$^+$03], (a) Fusion bonding of SOI wafer and wafer with cavity (b) Removal of silicon and oxide layer by etching (c) Electrode deposition and sealing.

Because wafer bonding is a high temperature process which is not compatible with IC processing, this process does not allow the integration of electronics and transducers on the same CMUT wafer prior to bonding [CFM+06].

For our research work, the CMUTs are fabricated at SINTEF MiNaLab in collaboration with NTNU using the wafer bonding process. The process is based on [BCD+10] and it is further described by Due-Hansen *et al.* in [DHMP+12]. The main feature of this CMUT is that the electrical connections to the array elements are achieved by via-holes through a thinned silicon wafer. The membrane side is uniform and electrically grounded. The transducer elements are organized in groups of two by two CMUT cells and the connection is made through a via hole in one of the four cells. The membrane comprises different layers forming a stack. For a particular case shown in Figure 2.7, the membrane stack consists of silicon dioxide, silicon, aluminum and plasma enhanced chemical vapor deposition (PECVD) nitride. With the interconnection pads on the back side of the CMUT, it may be easier to bond with electronics by flip chip bonding.
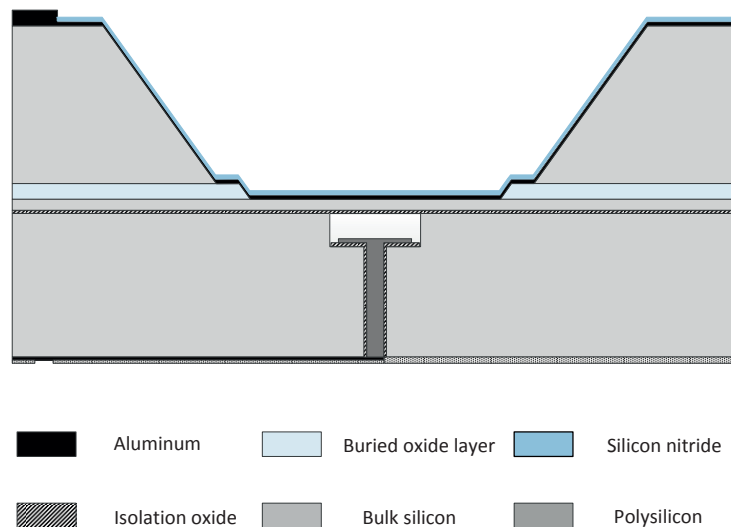
Figure 2.7: Wafer bonding process for CMUT with through-silicon vias.

Beside this, other varieties of wafer bonding techniques namely the LOCOS (local oxidation of Silicon) process, the thick buried oxide process, and

the piston CMUT structure and process have also been used for the fabrication of CMUTs [KYO11]. The LOCOS process provides good gap height control which is achieved by patterning of the silicon substrate inside the cavity via thermal oxidation and forming oxide posts by local oxidation. In the piston CMUT structure and process, the structure is designed so that the resulting membrane motion resembles the ideal piston like motion.

2.4.3   Reverse fabrication process

Although most of the CMUTs today are fabricated using either the sacrificial release method or the wafer bonding process, another process known as the reverse fabrication process has been proposed by Caliano *et al.* [CCS$^+$05]. An advantage of this technology is that it provides interconnection pads directly on the back side of the die, making it easier to connect the device in practical circuits. Other processes have also used technologies like deep trenches or via holes to allow connection to elements from the back side of the CMUTs, but it complicates the design and may increase parasitic capacitance [BCD$^+$10] [ISC11].

The reverse fabrication process starts with a silicon wafer which is coated on both sides by a LPCVD silicon nitride layer. Aluminum is deposited to form the ground electrode and passivation is done with PECVD nitride which is followed by deposition of a sacrificial chromium layer. The sacrificial layer is patterned by lithography to define the cavity of the CMUT and then covered by a thin nitride layer. Aluminum is then sputtered and patterned using a second mask. The chromium layer is removed using etch holes, and the holes are sealed using PECVD nitride, whereas patterning is done to open the contact pads. Acoustic backing material is then added for mechanical support as shown in Figure 2.8. Finally, the bottom LPCVD nitride layer and bulk silicon is removed by etching to release the membrane.

It is difficult to define the acoustic backing for CMUTs on silicon because it needs a high acoustic impedance that should match with the acoustic impedance of the silicon substrate. In the reverse fabrication process bulk silicon is removed leaving only a thin nitride membrane. Defining the acoustic backing would not be difficult in this case because the acoustic impedance need not be very high. This is one of the main advantages of the reverse fabrication process. We will discuss the backing requirements for CMUTs in more detail in Chapter 3.

Figure 2.8: Reverse Fabrication process for CMUT. Only final steps are shown, (a) Cavity formation using deposition of sacrificial chromium, Al deposition and sealing by PECVD nitride layer (b) Casting of acoustic backing material at backside (c) Removal of LPCVD nitride layer and bulk silicon using wet etching.

2.5 Applications

A CMUT could easily be designed with a low acoustic impedance which makes it easy to match to gaseous and/or fluid media. Air applications are useful for non-destructive testing (NDT), and ultrasonic speed measurement whereas the most important immersion application is medical imaging. These applications will be described in brief in this section.

2.5.1 Air applications

For efficient transmission and reception of ultrasound into a medium, the acoustic impedance of the medium should be matched with the acoustic impedance of the transducer. Piezoelectric transducers are commonly used ultrasound transmitters. But the acoustic impedance of such transducers are very high as they are made up of ceramic composites. The acoustic impedance is about 33.7 MRayl for a ceramic PZT. This causes large impedance mismatch when used in air. The problem is solved in such transducers using PZT/epoxy composite and matching layer/s. Although piezoelectric MUT transducers have been shown to give good matching and

are applicable at high frequencies, they may be difficult to manufacture [AMF$^+$04]. CMUTs on the other hand, uses a very thin membrane over a cavity, which can easily be designed to provide reasonably good match with the acoustic impedance of air. Due to reasonable acoustic matching and electromechanical coupling in air, CMUTs are proposed for ultrasonic ranging, gas flow metering and non-destructive testing (NDT) of solids. Because CMUT cavities are sealed, they are also tolerant to humidity and particles when used in air applications. As it is fairly easy to fabricate arrays using CMUTs, beam shaping and steering could also be possible with CMUTs.

2.5.2   Immersion applications: medical imaging

When CMUTs are loaded with a fluid or a mechanically equivalent solid, it is an immersion application [EYOKY06]. All the applications that are mentioned in air are also possible in immersion such as ultrasonic ranging, flow metering and NDT. The acoustic impedance of fluids are generally higher than the membrane impedance in most of the CMUT designs, thus fluid loading overdamps the resonant membranes of the CMUTs resulting in wide band operation. This is one of the major advantages of using CMUTs in immersions. Because the acoustic impedance of most human tissues are close to that of water, medical imaging is an important immersion application for CMUTs.

CMUT transducers may be useful in producing ultrasound waves of high frequencies as their dimensions may be made very small. High frequency transducers are able to resolve the small structures, however the penetration depth will be low. The acoustic attenuation in most materials increases with frequency, for most human tissues the attenuation is about 0.5 dB/cmMHZ [Ang96]. Together with the maximum allowed acoustic power in tissue, this gives a maximum limit on the frequency that could be used in ultrasound for medical imaging with a given penetration depth. There are different medical applications where range is short and better resolution is needed as discussed in Chapter 1. As the dimensions of piezoelectric transducer elements are scaled with wavelength (quarter wavelength or half wavelength depending upon the design), high frequency broadband transducers are difficult to manufacture using piezoelectric materials. High frequency transducers up to 80 MHz have been fabricated with PMN-PT (Lead Magnesium Niobate-Lead Titanate) as the active piezoelectric material [ZXG$^+$07] [LWC$^+$11]. However, the fractional bandwidth of such transducers is relatively low. CMUTs could be a very good alternative for such cases. High frequency transducers using CMUTs could easily be designed to provide wider bandwidth in immersion. This makes it a good choice for

applications like tissue harmonic imaging where the energy is transmitted at a fundamental frequency and the image is formed from the energy at second harmonic formed in the medium. However nonlinear operation of CMUT which easily gives a second harmonic content in the transmitted pulse should be taken into account.

Although CMUTs have not been much used commercially for medical imaging purposes, they have been demonstrated for medical purposes by several research groups. Oraklan *et al.* [OEJ+02] have demonstrated an imaging experiment using 128-element CMUT. Caliano *et al.* [CCC+05] reported images of an ultrasound phantom consisting of nylon wires, immersed in a uniform parenchyma mimicking human tissue using CMUTs. The obtained images were comparable with images obtained using commercial piezoelectric probes. A commercial CMUT probe that could be used for breast imaging was announced by *Hitachi* in 2009 [Cor09]. This probe known as *Mappie* uses the sacrificial release process for the manufacturing of CMUTs.

Beside these applications, CMUTs could be useful for other applications like microfluidics, generation of lamb waves, microphones with RF detection etc [EYOKY06].

2.6 Advantages and challenges of CMUTs

Piezoelectric transducers have been used for many decades for the generation and reception of ultrasound waves. Although electrostatic transduction was demonstrated quite early, the large electric field required for such a transducer was very difficult to achieve during that period. After the introduction of microfabrication techniques, creating sub-micron gaps became much easier; thus CMUTs transducers could be realized with moderate bias voltages.

One advantage of CMUT is that being a micromachined device which is usually made on silicon substrates, it may be easily integrated with electronics. Due to its batch fabrication technology, production cost of CMUT transducers could be small compared to the piezoelectric transducers. For integration with electronics, electronic circuits and CMUT arrays made on separate wafers can be bonded together to form a 3D stack. But a problem is that the stack assembly procedures are not yet developed for CMUT transducers. Another problem with CMUT transducers is acoustic crosstalk between neighbor elements at the fluid structure interface. This may excite local resonances in the interface region and may affect the overall transmission from the CMUT arrays for frequencies well within 100% bandwidth of

the transducer. There have been some suggestions to use double periodicities and a lossy layer on top of the CMUT membrane to minimize this effect [BR06] [BR07].

An important figure of merit of ultrasound transducers is the electromechanical coupling coefficient, k. It is a basic index of energy-conversion capability of the transducer [Woo57]. In the case of CMUT, the coupling coefficient is given in terms of two Q-factors, the electrical Q-factor, Q_{el}, and the mechanical Q-factor, Q_m as [Røn09]

$$k^2 = \frac{1}{1 + Q_m Q_{el}} \quad . \tag{2.15}$$

The values for the mechanical and the electrical Q-factors should be low for the CMUT transducers in order to provide broad band operation with a low insertion loss. This gives the coupling coefficient for such transducers to be close to unity. A simpler way of obtaining the coupling coefficient is given in [CCP03] in terms of fixed (C_m) and free (C_T) capacitance of CMUT as

$$k^2 = 1 - \frac{C_m}{C_T} \quad , \tag{2.16}$$

where C_m is the fixed capacitance given by equation (2.2) and C_T is the capacitance defined as the slope of the charge voltage curve when the membrane is allowed to deform.

The coupling coefficient for a typical piezoelectric ceramic can be 0.3 to 0.7 at low input frequencies [Cer02]. A high value of the coupling coefficient is desirable for efficient energy conversion but it does not guarantee high efficiency as there are other losses as well. In well designed piezoceramics, efficiencies more than 90% can be achieved. In the case of CMUTs, the coupling coefficient increase with the bias voltage. To obtain a high coupling coefficient in a conventional mode, it must be operated near the collapse voltage. The conventional mode is a commonly used CMUT operation regime where the electrostatic forces due to the biasing voltages are lower than the available restoring forces in the membrane, and the membrane is never in contact with the substrate. Thus to operate the CMUT in the conventional mode, the bias voltage should be sufficiently low in order to prevent collapse [YEB+03]. It has been reported that operation of CMUTs in collapsed mode yields higher output pressure and improved coupling coefficients compared to the conventional mode [HHB+06]. But there is a possible problem with charging of the membrane when it is in contact with the substrate, as is required in the collapsed mode.

Although CMUTs have a lot of promising offers, it will not be able to replace the piezoelectric transducers in many applications. Both technologies will probably compliment each other in the future. CMUTs will probably be used in the applications where high frequencies and large bandwidth are needed for example in invasive ultrasound applications. Its potential advantages such as low production cost, small size and compatibility with electronics will obviously be helpful in this regard.

Chapter 3

Backing for CMUT Transducers

Ultrasonic transducers, whether they are piezoelectric or CMUTs, need an acoustic backing to provide satisfactory performance. The backing requirements could be different for different types of ultrasonic transducers. In this chapter we discuss the backing requirements for ultrasonic transducers in general with particular attention to CMUT transducers. We also discuss different types of materials that could be used as backing.

3.1   Backing used for ultrasonic transducers

Most of the ultrasonic transducers today use ceramic piezoelectric materials such as PZT as an active element. Acoustic waves are generated when an alternating voltage is applied to electrodes deposited on opposite sides of such piezoelectric materials. At some particular frequencies, the plate will have thickness resonances, and the conversion from electric to acoustic energy is more efficient at these frequencies. The first resonance will occur when the thickness of the plate is close to half a wavelength if it is loaded with a low acoustic impedance.

As discussed in Chapter 2, such transducers have very high acoustic impedance (e.g. 33.7 MRayl for ceramic PZT). These transducers have a large impedance mismatch when they are used in air or immersion applications. One of the important applications of ultrasonic transducers is in medical diagnostic. As the acoustic impedance of most human tissues are close to that of water, the acoustic impedance mismatch is large when these transducers are used for medical imaging [Wel99]. Since the piezoelectric transducer operates at resonance, it will ring for some oscillations even after

the voltage source is removed. This ring-down in the response of the transducer increases its pulse duration which will directly affect the bandwidth of the transducers giving poor axial resolution. There exists different solutions to minimize this effect.

- One solution is to use a matching layer between the transducer and the load which has a thickness of $\lambda/4$, where λ is the wavelength in the matching material. This layer transforms the acoustic impedance of the load and thus are referred to as *quarter wavelength transformer*. If the impedance mismatch is very large, it is difficult to find a matching layer with the desired value of the acoustic impedance. In such cases, multiple matching layers could be used. The use of such multiple matching layers may result in broadband and efficient piezoelectric transducers [DFK78].

- Another solution is to use an acoustically absorbing backing layer at the bottom of the transducer where the ringing is damped because energy is transmitted into the backing layer. This backing material should provide high attenuation and it should match the acoustic impedance of the transducer for efficient coupling of waves [SC84]. If its acoustic impedance is matched with the transducer, the pulse duration would be short but the efficiency of the transducer would be small since a substantial part of the power is lost in the backing. The bandwidth, however, will increase due to a shorter pulse duration. So there is a trade off between efficiency and the pulse duration using this method. The relation between pulse duration and bandwidth is illustrated in Figure 3.1. It shows that the decreased pulse duration due to use of a lossy backing material could provide wider bandwidth.

As the use of a backing material introduces losses which can reduce the efficiency of the ultrasonic transducer, this method is not preferred; instead $\lambda/4$ matching layer/s are used for efficient coupling of waves. However, acoustic backing is needed for the mechanical support of the transducer. The energy loss into the backing is minimized by using either a very low impedance backing or a very high (infinite) impedance backing. When the backing impedance is much larger than the transducer plate impedance, the resonance of the transducer changes from half-wave resonance to quarter-wave resonance. It is not commonly used as it is difficult to achieve a sufficiently high backing impedance. But there have been some suggestions to use rigid materials like rolled copper (Z=44.6 MRayl), yellow brass (Z=40.6 MRayl), or rolled aluminum (Z=17.3 MRayl) as high impedance
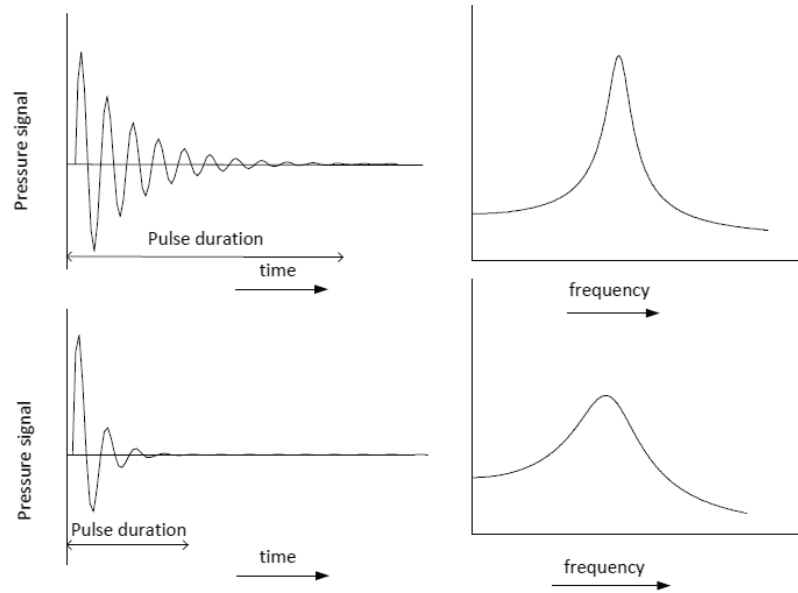
Figure 3.1: Relation between pulse duration and resulting bandwidth showing that the bandwidth increases when the pulse duration is shorter, from [Ang96].

backing. These materials can also serve as one of the electrodes for the transducer. But the main challenge here is to get a very thin adhesive layer so as to maintain the resonant frequency at quarter wavelength. Recently some transducers have been fabricated where the piezoelectric material is deposited directly on aluminum electrodes by sputtering that serves both as high impedance backing as well as electrode [CWZ$^+$07]. But this technique is more suitable for piezoelectric polymer transducers [Bro00][CL10].

In medical imaging applications, it is better to reduce the energy flow into the backing to increase the efficiency and the sensitivity of the transducer. Thus a transducer with quarter wave matching with no backing or low impedance backing is preferred for this case [Ang00]. A typical piezoelectric transducer with both matching and backing layer is shown in Figure 3.2.
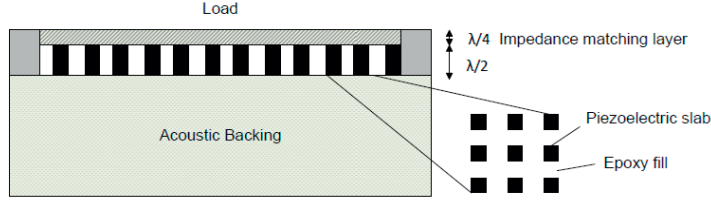
Figure 3.2: Typical piezoelectric transducer made by a composite material with quarter wavelength impedance matching layer and acoustic backing layer.

3.2   Need for backing in CMUTs

CMUT transducers also need an acoustic backing structure for satisfactory performance similar to other ultrasonic transducers. As we have already explained in Chapter 2, CMUTs are fabricated on silicon substrates. Figure 2.1 shows a simple CMUT circuit in transmission mode where an aluminum electrode on top of a silicon nitride membrane acts as a top electrode and the bulk silicon substrate acts as a bottom electrode.

When an AC voltage is applied to the biased electrodes, the CMUT membrane vibrates. This generates an ultrasound wave in the medium of interest. Since the electrostatic force is experienced by both the membrane and the bulk substrate carrying the CMUT, the substrate will also experience the same amount of force as the membrane although the particle motion in the substrate is smaller than the particle motion in the medium of interest. This energy coupled into the substrate generate bulk waves that may be reflected from the bottom of the substrate. This is referred to as *silicon substrate ringing* [LW00]. If the back surface is free, the waves reflected from the bottom of the substrate are out of phase with the excitation signal except at frequencies where resonant modes are excited. This occurs at the frequencies where the substrate thickness is an integer multiple of half of the wavelength given by

$$f = n \left(\frac{v}{2t} \right) \quad , \tag{3.1}$$

where n is an integer, v is the longitudinal velocity in the silicon substrate, and t is the thickness of the substrate. For example, if the substrate thickness is 500 μm, and the longitudinal velocity of sound in silicon is 8000 m/s, the ringing will occur at integer multiples of 8 MHz. The excitations will appear as notches in the frequency response of the transducer at the thickness

resonances.

Such ringing will significantly degrade the performance of the transducer. It will reduce the usable bandwidth of the transducer and will lead to higher levels of mechanical cross-coupling between adjacent transducer elements [LW00]. To suppress the ringing, various solutions have been proposed [KEY05] [LW01]. One of them uses acoustic backing behind the silicon substrate that absorbs the backward radiated energy. The acoustic backing then should fulfill two requirements. The acoustic impedance of the backing should be perfectly matched with the acoustic impedance of the silicon substrate meaning that no acoustic energy would reflect back to the transducer from the transducer-backing interface. The other requirement is that the acoustic backing layer should be lossy. This means that all the acoustic energy coupled into the backing from the substrate should be absorbed. If such a backing material of sufficient thickness is added to the silicon substrate, it will suppress the substrate ringing in CMUT transducers.
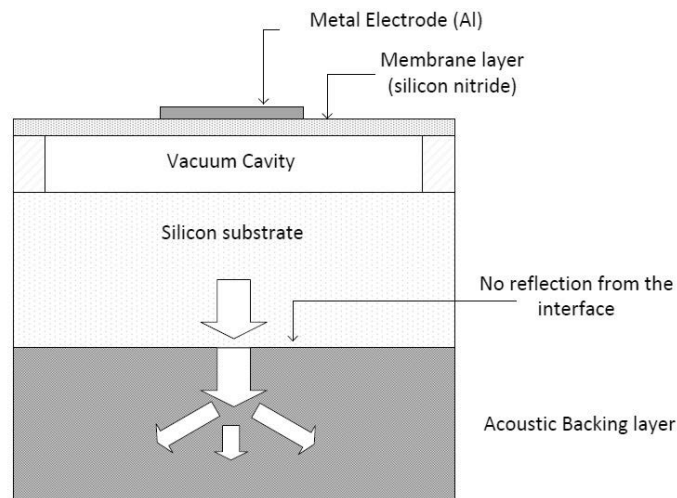
Figure 3.3: CMUT with acoustic backing layer that fulfills the requirements discussed in the text; a lossy backing layer matched to the substrate gives no reflection back to the transducer and all the acoustic energy would be dissipated in it.

Another approach is thinning down the silicon substrate so that the first ringing mode lies outside the operating frequency range and does not significantly affect the performance of the transducer. But acoustic backing should be used in this case also to provide mechanical support and to prevent the propagation of bending waves transversely in the substrate. However, the backing requirements would not be as strict for this case as in the earlier one.

Khuri-Yakub *et al.* [KEY05] suggested to use a parallel groove structure in the substrate to suppress such ringing modes. Such grooves should have a height equal to a quarter wavelength at frequencies where the ringing would appear. This give the cancellation of ringing at particular frequencies. The effective use of this method for a broad frequency range is described further by the present author in papers [CR09] and [CR11]. This is more applicable for the case where there is limited space available under the transducer such as in intravascular ultrasound (IVUS) imaging. This method will be described in detail in Chapter 4, where an improved backing structure for CMUT is discussed.

In Section 2.4.3 of Chapter 2, we discussed the reverse fabrication process that have been used to fabricate CMUTs. In this design, the bulk silicon substrate is removed and only a few micron thick layer of silicon nitride is present under the cavity. Thus the ringing effect, which is due to the thickness resonances in the silicon substrate, is minimized. Acoustic backing, however, is needed to provide the mechanical support for the device. Such a backing layer does not have as strict a requirement to match acoustically to silicon as earlier, so they are fairly easy to define. But there are still possible echo problems which must be removed for satisfactory performance of CMUTs.

CMUT transducers open the door for 3D imaging since it is possible to fabricate 2D transducer arrays operating at high frequencies offering wide bandwidth using this technology. For this purpose, electronic circuits and CMUT arrays made on separate wafers can be bonded together with acoustic backing to form a 3D stack. Surface acoustic waves (SAW) might be generated when such devices are used in a fluid medium with off axis beam steering as suggested by Berg *et al.* [BR09]. These waves can increase the total acoustic crosstalk in CMUT arrays. As the SAW is exponentially damped into the silicon substrate, the substrate should be thin compared to the characteristic wavelength in order to allow the acoustic backing layer at the bottom of the substrate to absorb these waves. A thin intermediate layer of an absorbing material between the CMUT substrate and the electronic wafers could also be used to dissipate such surface acoustic waves.

The response of a CMUT array may be degraded not only due to SAW waves but also due to excitation of bulk waves that propagates through the substrate and the backing and reflects back. Berg *et al.* [BR09] have shown that for a stack of CMUTs including wafer electronics and different bonding layers, an acoustic backing layer that provides 20 dB loss at the top of the backing layer for the specular reflection, can reduce the ringing resulting from the propagation of such bulk waves to acceptable levels.

3.3 Materials used for backing

3.3.1 Use of composite materials

The acoustic backing for CMUT transducers should have a high acoustic impedance, and it should be lossy to absorb the acoustic energy effectively. Polymers like epoxy resin or rubber are often chosen as the lossy material, but their acoustic impedances are quite low. Different filler materials are added in a polymer matrix to increase the density and hence the acoustic impedance of the mixture. Such composite materials fulfill both requirements of the backing material. Choice of filler materials in a polymer matrix also depends on the backing requirements for the ultrasonic transducers. If a backing with low acoustic impedance is desired, fillers like wood, glass, etc. are added whereas heavy fillers like tungsten or alumina are added for high impedance backing. In either case, composite materials that consist of fillers in an epoxy resin or rubber can be used as a backing material.

The main cause of attenuation in composite materials is the loss of acoustic energy which is mainly due to two mechanisms; one is the scattering of acoustic energy and other is the absorption losses in the material. These causes will be discussed in more detail in Section 3.4. Acoustic loss in the polymers is dependent on the degree of crystallinity and cross linkage of the material. In case of solid materials or ceramics, the inhomogeneities in the material will also cause scattering of ultrasonic waves which depends upon the difference of densities and elastic moduli from point to point in the medium. In a similar way, fillers in a polymer matrix contributes to attenuation of ultrasonic waves. This attenuation also depends on the particle shape, size and acoustic impedance of the fillers [GGR90]. Wang *et al.* [WRC01] have suggested that poor adhesion between the filler and the polymer matrix may also contribute to attenuation.

Depending upon the requirements, a backing material could be made conducting or non-conducting. The composite materials discussed here contains fillers in an epoxy matrix. Connectivity is an important factor

in multiphase materials as they can highly influence the material properties. Fillers in an epoxy matrix is a two phase composite where each phase in the composite may be self-connected in zero, one, two or three dimensions. In two phase composites, there can be ten possible connectivities: (0-0), (1-0), (2-0), (3-0), (1-1), (2-1), (3-1), (2-2), (3-2), and (3-3) [NSC78]. The connectivity depends upon the volume of filler particles present in the epoxy matrix in this case. For lower volume fraction of fillers, it behaves like a (0-3) composite material which is a common choice for an intermediate layer or a backing layer for ultrasonic transducers. As the volume fraction increases, the connectivity may change. This will also change the conductivity of the composite material. The conductivity of the material could also be improved by using fillers with larger particle sizes, by adding powder or flakes of electrically conducting metals (silver or copper) or by applying high pressure [MMS00].
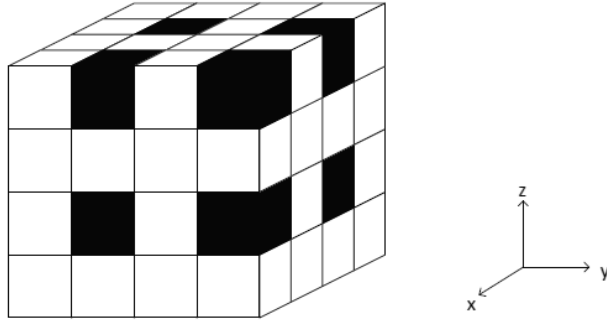
Figure 3.4: Connectivity pattern for (0-3) composite structure, from [NSC78]. In this particular case, black color represents the filler particle tungsten with 0-connectivity whereas the white color represents the epoxy matrix with connectivity 3.

For CMUTs, a high impedance backing material is needed as the acoustic impedance of the silicon substrate is high (about 19.6 MRayl). We have chosen epoxy filled with tungsten powder for this purpose. The epoxy chosen is a two part epoxy, EPO-TEK 301-2, from *Epoxy Technology* because of its high attenuation, low viscosity, and long pot life. A spherical tungsten powder with particle sizes varying from less than 1 μm to 5 μm from *Alpha Aesar* is chosen as filler material. The material properties of the epoxy and the tungsten powder used in this work are taken to be as shown in Table 3.1. It is known that in the case of solid specimens of metal or

ceramics, the inhomogeneities in the material will cause scattering of acoustic energy determined by the difference in the density and elastic modulus from the surrounding media. Thus the materials are chosen as they have large difference in their acoustic impedances. The optimum choice of particle size of tungsten powder depends on the wavelength used. It is related to the scattering of acoustic energy in the composite structure. The acoustic impedance of such a composite structure may be controlled over a wide range by changing the volume fraction of tungsten in the mixture. The volume fraction, VF, of the tungsten in the composite can be determined using the following relation:

$$VF = \frac{M_t/\rho_t}{M_t/\rho_t + V_e} \quad , \quad (3.2)$$

where M_t and ρ_t are respectively the mass and the density of the tungsten powder and V_e is the volume of the epoxy.

Table 3.1: Material properties of epoxy resin and tungsten.

Material	Density (g/cc)	Longitudinal velocity (m/s)	Shear velocity (m/s)
EPOTEK 301-2	1.150	2650	1230
Tungsten	19.3	5200	2900

For lower volume fractions of tungsten, the composite behaves as a (0-3) composite whereas for volume fractions above 40%, it may behave differently. Different theoretical models have been proposed to predict the mechanical properties of such composite structures. Experimental verification of these properties have also been demonstrated [WRC01] [SNI05]. Based on the different models which will be discussed in the following section, we know that a backing layer that matches acoustically to the silicon substrate requires a high volume fraction of tungsten in the composite. Such a backing layer of sufficient thickness will be able to damp out most of the acoustic energy that appears in the substrate.

3.3.2 Theoretical models for composite materials

It is already mentioned that (0-3) composites are widely used in ultrasonics either as backing layers or as matching layers. For our application, we have chosen tungsten filled epoxy as a backing layer. To estimate the acoustic

impedance and velocities in the composite materials, different theories have been proposed; some are based on single scattering theory while others are based on multiple scattering theory.

In this section we discuss in brief the different theoretical models used to study the mechanical properties of composite materials. The most simple model has been proposed by Reuss and Voigt which respectively assumes constant stress and constant strain throughout the solid [NLLP96]. Models predicting upper and lower bounds for the elastic moduli of the composite material have been obtained by Hashin and Shtrikman which are based on energy considerations [HS63]. Berryman [Ber79] has proposed different single scattering approximations for the estimation of effective elastic constants of composite materials such as the average T-matrix approximation (ATA), the differential elastic medium (DEM) and the coherent potential approximation (CPA). Devaney *et al.* [DL80] have proposed a theory based on a self-consistent formulation of multiple scattering. All these theories assume that the inclusions are spherical with uniform size, which is much smaller than the wavelength. In the calculation shown below, the bulk modulus and the shear modulus of the homogeneous matrix (Epoxy) and inclusion (Tungsten) are respectively denoted by K_1, G_1 and K_2, G_2 whereas the effective moduli of the resultant composite are denoted by K and G. Volume fractions of matrix and inclusions are respectively v_1 and v_2.

Among the different models, the models which have been mostly used for the estimation of effective elastic parameters of the composite medium are discussed here in brief.

The Voigt and Reuss model

The Reuss model assumes a constant stress in the two constituents of the composite material. This method gives the lower bound for the ultrasonic velocity in the composite [LD77]. The Voigt model, on the other hand, assumes a constant strain in the two constituents and gives the upper bound for ultrasonic velocity. In fact, the Hashin-Shtrikman model provides upper and lower bounds that are inside the Voigt-Reuss bounds. The bulk modulus and the shear modulus of the composite in the Reuss model are respectively given by:

$$\frac{1}{K} = \frac{v_1}{K_1} + \frac{v_2}{K_2} \quad , \tag{3.3}$$

$$\frac{1}{G} = \frac{v_1}{G_1} + \frac{v_2}{G_2} \quad . \tag{3.4}$$

The bulk and shear modulus of the composite in the Voigt model are respectively given by:

$$K = v_1 K_1 + v_2 K_2 \quad , \tag{3.5}$$

$$G = v_1 G_1 + v_2 G_2 \quad . \tag{3.6}$$

The average T-matrix approximation (ATA)

This model is based on a single scattering theory of inclusions in composite materials. The problem is formulated in terms of scattering phenomena for long wavelengths. It is modeled using the following equations by making the single scattering of the inclusions in the composite material equal to the scattering of the composite material. The bulk modulus and the shear modulus of the composite material in the model are given by [Ber79]:

$$\frac{1}{K + \frac{4}{3}G_1} = \frac{v_1}{K_1 + \frac{4}{3}G_1} + \frac{v_2}{K_2 + \frac{4}{3}G_1} \quad , \tag{3.7}$$

$$\frac{1}{G + F_1} = \frac{v_1}{G_1 + F_1} + \frac{v_2}{G_2 + F_1} \quad , \tag{3.8}$$

where

$$F_1 = \frac{G_1}{6} \times \frac{9K_1 + 8G_1}{K_1 + 2G_1} \quad . \tag{3.9}$$

The Devaney model

This model is based on a self consistent formulation of the multiple scattering theory. When the volume fraction of the inclusion is low, this model will become similar to other models. But when the volume fraction of inclusion becomes high, multiple scattering effects are important and the model may become more accurate compared to models based on single scattering theory. The bulk modulus and the shear modulus of the composite material using the Devaney model are given by [DL80]:

$$K = K_1 + v_2 \frac{(3K + 4G)(K_2 - K_1)}{3K + 4G + 3(K_2 - K_1)} \quad , \tag{3.10}$$

$$G = G_1 + v_2 \frac{5(3K + 4G)G(G_2 - G_1)}{(15K + 20G)G + 6(K + 2G)(G_2 - G_1)} \quad . \tag{3.11}$$

It could be seen from equations (3.10) and (3.11) that the expressions for the bulk modulus and the shear modulus also contain the same terms. Thus the solution of these equations requires a number of iterations. The process of determining the bulk modulus and the shear modulus should be started with some initial approximations for both moduli.

3.3.3 Comparison of the models

To compare the performance of the models described above, longitudinal velocities and acoustic impedances are computed for different volume fractions of tungsten. All the models described above give the effective bulk modulus, K and shear modulus, G of the resultant composite medium. When the values for K and G are obtained, the longitudinal velocity, v_l and the shear velocity, v_s of sound wave in the composite medium are calculated as

$$
\begin{aligned}
v_l &= \sqrt{\frac{K + \frac{4}{3}G}{\rho}} \quad , \\
v_s &= \sqrt{\frac{G}{\rho}} \quad .
\end{aligned}
\tag{3.12}
$$

where ρ is the density of the two-phase composite material. The density is given in terms of the densities of the matrix, ρ_1, and the density of the inclusion, ρ_2, as:

$$
\rho = v_1 \rho_1 + v_2 \rho_2 \quad . \tag{3.13}
$$

The acoustic impedance is the product of density and the velocity of sound wave. The longitudinal velocity and the acoustic impedance for the tungsten epoxy composite are simulated for different volume fractions of tungsten powder. Material properties of epoxy resin and tungsten used in the simulation are shown in Table 3.2. To make a comparison of the simulation and the experimental results, the material properties of the epoxy are taken from Nguyen *et. al* [NLLP96] which is different from the epoxy used in our work.

Based on the data presented in Table 3.2, the longitudinal velocity and the acoustic impedance of the composite material calculated from the four different models are shown in Figure 3.5 and 3.6. As discussed earlier, the Voigt model and the Reuss model provide repectively the upper and the lower bound on the ultrasonic velocity in the composite material. From the figures, it is clear that for lower volume fractions, all the models except the

Table 3.2: Material properties of epoxy novolac resin and tungsten.

Material	Density (g/cc)	Longitudinal velocity (m/s)	Shear velocity (m/s)
Epoxy novolac resin	1.260	2340	1140
Tungsten	19.3	5200	2900

Voigt model behave similarly. But as the volume fraction increases, the multiple scattering is dominant. Then the Devaney model should be the best fit among the models discussed here as it considers multiple scattering. Experiments have been performed with tungsten epoxy composites for different volume fractions of tungsten [SNI05] [NLLP96]. The Devaney model shows good agreement with the experimental results as shown in Figure 3.5. From Figure 3.6, it is clear that to match the acoustic impedance of the composite to silicon, the volume fraction of tungsten in the composite should be about 49%. This gives a longitudinal velocity in the composite of about 1930 m/s and a density of the composite of about 10150 kg/m^3.

To match the acoustic impedance of the composite with silicon, a special technique is needed since the mixture becomes difficult to work with for higher volume percentage of tungsten than 40% [BML$^+$04]. Because of the ease of preparation of the composite using simple techniques such as hand mixing, a composite with a slightly smaller volume fraction of tungsten is chosen in our work. The backing material should have an acoustic impedance of 18 MRayl or more to match its impedance fairly well with silicon of 19.6 MRayl. From the Devaney model we find that 46% volume fraction of tungsten gives the acoustic impedance of about 18 MRayl with a velocity of 1890 m/s and a density of 9500 kg/m^3. The Devaney model assumes that all the inclusions are all equal in size and spherical. We deliberately have used a mixture of tungsten powders of different diameters which we expect will ease the inclusion of tungsten in the mixture, but it also makes the results from the Devaney model more uncertain. Early calculations started with a slightly different velocity, 2000 m/s, and density, 9000 kg/m^3, gives the same acoustic impedance. Due to the uncertainties these round numbers have been kept in the simulations.
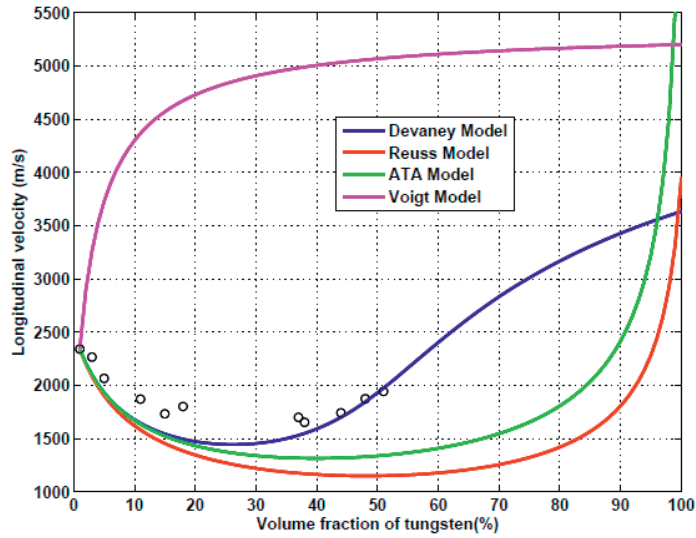
Figure 3.5: Variation of longitudinal velocity in epoxy tungsten composite with volume fraction of tungsten. The dots shown in the figure are experimental values of longitudinal velocities obtained from [NLLP96].
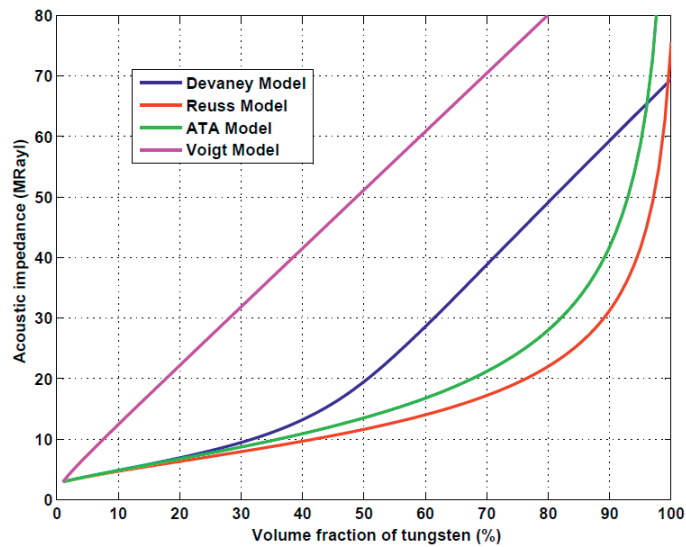
Figure 3.6: Variation of acoustic impedance in epoxy tungsten composite with volume fraction of tungsten.

3.4   Acoustic attenuation in backing material

In this section we discuss the causes of attenuation of acoustic waves in a material, focusing on acoustic backing for ultrasound transducers. The different sources of loss in the material are discussed briefly and modeling of such losses in a composite material is also presented.

3.4.1   Cause of attenuation

When a sound wave travels in a medium, some of this energy is lost in the medium. In most of the cases, it is converted into random thermal energy. The sources of dissipation of energy may be divided into two general categories; one is intrinsic losses in the medium, and the other is associated with boundaries of the medium [KFCS00]. Intrinsic losses in the medium are mainly due to viscous losses, heat conduction losses, and internal molecular processes like relaxation and dislocation damping. When a medium contains inhomogeneities (for example voids in a solid material or fillers in an epoxy matrix), more acoustic energy is lost in the medium compared to a homogeneous medium. This excess attenuation is mainly due to two mechanisms: (1) scattering of acoustic energy (Rayleigh, diffusion, and stochastic), and (2) absorption losses which convert the acoustic energy into thermal energy [GGR90].

Viscous losses come into effect when there is relative motion between the adjacent portions of the medium. This may occur during shear deformation of the medium or the compressions and expansions caused by the transmission of the sound wave [KFCS00]. The absorption coefficient due to viscous loss in a medium is given by [Kin87]:

$$\alpha = \frac{\omega^2}{2\rho c^3} \left(\frac{4}{3}\eta + \eta_B \right) \quad , \tag{3.14}$$

where ω is the angular frequency, ρ is the density, c is the velocity of the sound, η is the coefficient of shear viscosity, and η_B is the coefficient of bulk viscosity. From equation (3.14), it is clear that the absorption coefficient is proportional to the square of frequency and inversely proportional to the third power of the velocity. As the velocity of shear waves for most materials typically is close to one half of the velocity of longitudinal waves, viscous loss will be much higher for the shear waves.

The other source of loss in a material is due to heat conduction. Heat conduction losses result from the conduction of thermal energy from higher temperature regions with compression to lower temperature regions with rarefactions. The absorption coefficient due to thermal conduction has the

same frequency dependency and the same velocity dependency as that for viscous loss. For a perfect gas, it is given by [KFCS00]

$$\alpha_\kappa = \frac{\omega^2(\gamma - 1)\kappa}{2\rho c^3 C_P} \quad , \tag{3.15}$$

where κ is the thermal conductivity, γ is the adiabatic index, C_P is the specific heat at constant pressure, ω is the angular frequency, ρ is the density, and c is the velocity of sound. The equation (3.15) is derived for a perfect gas but it also applies to any other medium [KFCS00]. It is clear from the equation that α_κ vanishes for $\gamma = 1$. For $\gamma = 1$, the equation changes to isothermal condition from adiabatic condition and there would be no thermal fluctuations due to propagation of acoustic waves.

While determining the absorption coefficients in equations (3.14) and (3.15), the medium is assumed to be a continuum having directly observable properties such as density, pressure, temperature, velocity, specific heat, and compressibility without concerning its molecular structure. Both equations are valid for frequencies much smaller than the relaxation frequency.

In addition to these losses, attenuation may occur due to scattering by finite-size grains or by dislocations in a solid. Another cause of attenuation is the unequal thermal conductivity and expansion of neighboring grains due to their axis being rotated with respect to each other [Kin87]. For this reason, high quality single crystal materials exhibit lower sound attenuation at high frequencies than the same materials in a polycrystalline form.

As discussed in Section 3.3.1, the acoustic backing used in our case is a composite material that consists of tungsten particles in an epoxy matrix. As epoxy is a viscous material, it contributes to the attenuation with an amount which is proportional to the square of the frequency. The attenuation would significantly increase for higher frequencies where CMUTs are usually operated. It is thus a good choice for the lossy material. But the acoustic impedance of such materials is low. The acoustic impedance can be increased by adding high density materials like tungsten and alumina powders. This will increase the density as well as the acoustic impedance of the composite material. If the size of the filler particles are chosen small compared to the wavelength, they scatter waves in all directions and thereby reduce the power in the coherent acoustic wave. A large number of these particles behave collectively as a diffuse reflector. This scattering of acoustic waves is called *Rayleigh scattering*. A lot of theoretical work has been carried out to calculate the scattered pressure from such inclusions using different approximations such as quasi-static and Born approximations [GDKH77]. Ying *et al.* [YT56] have suggested that when the particle size is small

compared to the wavelength, the attenuation per wavelength varies as the fourth power of the frequency. However, at very high frequencies, they tend to behave as a specular reflector.

In addition to this, fillers in a polymer matrix contributes to the attenuation in ways that depends on their shape, size and acoustic impedance relative to the polymer matrix [GGR90]. Wang *et al.* [WRC01] have suggested that poor adhesion between the filler and the polymer matrix also contributes to attenuation.

3.4.2 Modeling of the acoustic attenuation

If the amplitude of the stress is small and the wavelength is much larger than the dimension of the inclusions, the composite could be modeled as a homogeneous isotropic linear viscoelastic material [WLNH80]. A common characteristic of such a material is that its modulus of elasticity can be represented by a complex quantity that depends on frequency. This gives attenuation of such materials a frequency dependent characteristics.

For the composite we are modeling, tungsten powder with spherical particles with sizes less than 5 μm is used. The frequency range used is around 30 MHz. The longitudinal velocity for such a composite structure is estimated to be about 2000 m/s using the Devaney model. For this frequency range, the size of the particles are much smaller than the wavelength. Thus the composite can be modeled as a linear viscoelastic material as stated earlier. A loss factor damping is used to model the attenuation where the viscoelastic material is modeled with a complex elastic modulus. The complex modulus is the frequency domain representation of the stress relaxation function of the viscoelastic material. The complex modulus of elasticity may be written as:

$$E^{'} = E(1 + j\eta) = E_1 + jE_2 \quad , \tag{3.16}$$

where

$$E_1 = \text{Storage modulus,}$$
$$E_2 = \text{Loss modulus,}$$
$$\eta = \text{loss factor} = \frac{E_2}{E_1}.$$

The first part, E_1, is called storage modulus as it gives the material's ability to store energy elastically, and the second part, E_2, is called loss modulus as it gives the material's ability to dissipate the energy. The loss factor, η, is used to describe the energy dissipation property of the material.

This is defined as the ratio of energy lost in a cycle, W, to the peak potential energy, V, stored in the system during that cycle, divided by 2π [Cra70]:

$$\eta = \frac{W}{2\pi V} \quad . \tag{3.17}$$

The longitudinal wave velocity (v_l), and the shear wave velocity (v_s) are related to the Young's modulus of elasticity and the Poisson's ratio as follows:

$$
\begin{aligned}
v_l &= \sqrt{\frac{E(1-\nu)}{\rho(1+\nu)(1-2\nu)}} \quad , \\
v_s &= \sqrt{\frac{E}{2\rho(1+\nu)}} \quad .
\end{aligned}
\tag{3.18}
$$

where E is Young's modulus of elasticity, ν is Poisson's ratio, and ρ is the density of the material.

To represent the modulus of elasticity by a complex quantity for such a viscoelastic system, the longitudinal and shear wave velocities are normally expressed as complex quantities. The complex velocities are given by:

$$
\begin{aligned}
v_l{}^2 &= v_l'^2(1+j\eta_d) \quad , \\
v_s{}^2 &= v_s'^2(1+j\eta_s) \quad ,
\end{aligned}
\tag{3.19}
$$

where η_d and η_s are loss factors normally referred to as dilatational and shear loss factors.

3.4.3 Calculation of the attenuation coefficient

To obtain the attenuation coefficient for the composite material, longitudinal wave propagation is considered here. For a plane longitudinal wave propagating along a principal direction, considered x here, in a linear viscoelastic material, there is only one non-zero strain component, ε. Following Crandall *et. al* [CKNP], the longitudinal stress, σ, in the composite material can be expressed as:

$$\sigma = E(1+j\eta_d)\varepsilon \quad . \tag{3.20}$$

If v is the particle velocity in x direction and ρ is the mass density of the medium, the equation of motion gives:

$$\frac{\partial \sigma}{\partial x} = j\omega\rho v \quad . \tag{3.21}$$

From the equation of conservation of mass, we have

$$\frac{\partial v}{\partial x} = j\omega\varepsilon \quad .$$ (3.22)

Combining equations (3.21) and (3.22), we can write a small signal wave equation for sound wave propagation in the material as:

$$E(1 + j\eta_d)\frac{\partial^2\varepsilon}{\partial^2 x} = -\omega^2\rho\varepsilon \quad .$$ (3.23)

In order for the strain waves to have the form of equation (3.23), the solution will be of the form $\varepsilon_0 = Ae^{j(\omega t - kx)}$, if the loss factor is not included. As equation (3.23) includes a loss factor η_d, the solution is then given by:

$$\varepsilon_1 = Ae^{j(\omega t - k_1 x)} \quad ,$$ (3.24)

where k_1 is the propagation constant given by

$$
\begin{aligned}
k_1 &= \frac{w}{v_{l_1}} \quad , \\
&= \frac{\omega}{v_l\sqrt{1 + j\eta_d}} \quad , \\
&= \frac{k}{\sqrt{1 + j\eta_d}} \quad , \\
&\approx k(1 - \frac{j\eta_d}{2}) \quad ,
\end{aligned}
$$ (3.25)

assuming that the value of η_d is small compared to 1, which is a practical assumption for most solid materials.

The equation (3.24) then changes to

$$
\begin{aligned}
\varepsilon_1 &= Ae^{j(\omega t - (k - \frac{jk\eta_d}{2})x)} \quad , \\
&= Ae^{j(\omega t - kx)}e^{-(\frac{k\eta_d}{2})x} \quad , \\
&= \varepsilon_0 e^{-\alpha x}, \text{where } \alpha = \frac{k\eta_d}{2} \quad .
\end{aligned}
$$ (3.26)

The quantity α is the attenuation coefficient for the longitudinal waves. It can be expressed in dB for a given length x as:

$$\alpha(\text{dB}) = 20log(e^{-\alpha x}) \quad .$$ (3.27)

The expression for α is also derived in [CKNP] for modeling of clay, the obtained result is given as:

$$\alpha = \beta \left(\frac{\omega}{c}\right) \quad , \tag{3.28}$$

where c is the longitudinal wave velocity given by $\sqrt{\dfrac{E}{\rho}}$, ω is the angular frequency, and β is a constant given by

$$\beta = \frac{\sqrt{1 + \eta_d{}^2} - 1}{\eta_d} \quad .$$

The equation (3.28), for small values of η_d, results in the same value for α as given by equation (3.26). Equation (3.27) is used for the calculation of the attenuation coefficient in this work. It should be kept in mind that the value of α as given by equation (3.27) is just an approximation. This model assumes a linear dependence of loss with frequency which may not be true for all cases. The acoustic property of a composite material depends upon different manufacturing parameters such as working temperature, pressure, mixing, and the curing period. Thus experiments must be performed to determine the losses with high accuracy. However, the model described above gives a quick estimation of loss which is fairly accurate for lower volume fractions of inclusions and for a limited range of frequencies.

Chapter 4

Improved Backing of CMUTs

In Chapter 3, we have discussed the acoustic backing needed for CMUTs. In this chapter we discuss why conventional backing structure for CMUTs are not sufficient for many practical purposes and why we need an improved backing structure. We describe the working principle and some theoretical calculations made on such improved structures.

4.1 Need for an improved backing

If the acoustic backing needed for CMUTs is thick enough, it will absorb all the excess acoustic energy. But in imaging applications like IVUS, the space available for the transducer assembly is usually a few millimeters or even less. So there may not be enough space available for a thick backing layer. For example, in a catheter based ultrasound imaging system, *AcuNav* [Sie], the available space for acoustic backing material with adequate attenuation at 4 MHz is 0.5 mm or less [PTBR05]. In such applications, we propose an improved backing structure for the CMUTs. Such backing layers have a low profile structure at the bottom which contribute to some attenuation by scattering. This attenuation comes in addition to what the backing material provides by itself. Thus a thinner layer of such a structured backing would fulfill the backing requirements for CMUTs. This type of backing structure could possibly be used in connection with other types of ultrasound transducers.

4.2 Different ways of implementation

The use of a low profile structure at the bottom of the backing is similar to the backing structure proposed by Khuri Yakub *et al.* [KEY05]. This structure consists of parallel rectangular grooves with equal width and spacing of the grooves. This, in principle, gives cancellation of specular reflection of waves when the groove depth is a quarter of the acoustic wavelength at broadside. This structure scatters the waves into waves with significantly changed transverse wave vectors, giving long propagation paths back to the transducer. It may also convert longitudinal waves into shear waves which normally have much higher propagation losses in the backing material than the longitudinal waves. And in the case that waves with shifted k-vectors should reach back to the CMUTs, they will, only to a small degree, interfere with the imaging in the direction of interest. They will be further suppressed by focusing.

The structure proposed in [KEY05] causes scattering in a narrow band. We show that the scattering can be extended to a broader frequency range by superimposing grooves with different depths, different directions, and different periods to obtain cancellation of specular reflection at a set of frequencies. The principle is to provide sets of reflecting surfaces with equal areas but with different depths that may be grouped in pairs such that the depths differ by a quarter of a wavelength at the desired set of frequencies; the grouping is different at different frequencies. Cancellation of specular reflection at two independent frequencies requires four different depths; at three frequencies it requires eight different depths. The basic principle which is utilized by the method is shown in Figure 4.1.

A plane longitudinal wave is propagating towards a free surface which is corrugated in a periodic manner, here by rectangular grooves. The patterned grooves form a diffraction grating. Diffraction gratings reflect incoming waves in normal direction as well as directions oblique to the normal. The directions of the reflected waves depends upon the wavelength and the period of the pattern. The first oblique direction, for example, is given by

$$\theta = \frac{\lambda}{W} \quad , \tag{4.1}$$

where $W = 2d$ is the period of the grating, and λ is the wavelength of the wave connected to its velocity, v, and frequency, f, by

$$\lambda = \frac{v}{f} \quad . \tag{4.2}$$

The amplitudes of the diffracted orders depend on the depth of the
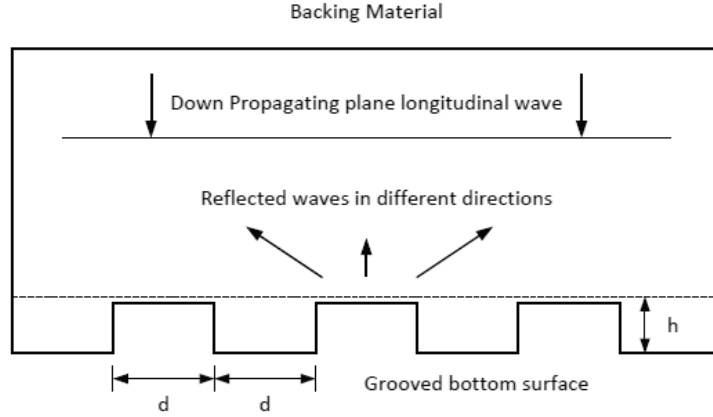
Figure 4.1: Sketch of a slab of backing material with a down-propagating plane longitudinal wave, which should be scattered/absorbed before it returns.

grooves. The grooves have the same width as the distance between the grooves, d, and the groove height is h. At the dotted line right above the bottom of the grooves, as a first approximation, there will be reflected waves with uniform amplitudes along the line, but with phase differences of $2h \times \dfrac{2\pi}{\lambda}$ between regions with and without grooves.

At a frequency where $h = \dfrac{\lambda}{4}$, the phase difference is 180° and the amplitude of the specular reflection, the wave reflected as it would have been from a plane bottom surface, is zero. Instead the wave is converted into longitudinal and shear waves with k-vectors in the transverse direction of multiples of $\pm \dfrac{2\pi}{2d}$. This conversion will only be effective over a rather narrow band in frequency. To be able to cover a larger band we have to use structures that effectively add several such scattering periodicities with different effective heights, h. It might also be desirable that the waves are scattered more or less uniformly in all transverse directions.

We want to make several such scattering structures work independently so that each of them makes a null in the specular wave reflection coefficient at a particular frequency. To obtain this, we must arrange them so that they add $2h$ propagation length to the signals reflected from half of the total area compared to the delays of the signals from the other half of the total area. This balance in propagation delays should preferably be maintained both globally over the complete structure, but also locally for smaller areas, everywhere in the structure.

One structure which is capable of doing this is etched squares of different sizes, where the squares of each size are organized as on a checker board. For example, the black checker board squares are etched down a certain height h_i for the ith checker board as shown in Figure 4.2. To accommodate several heights in the balanced way described above we must scale the size of the squares in the checker boards such that there is a linear factor of at least two in size between them (two to an integer power). Four squares of the smaller pattern should be placed in one of the next larger squares and so on. Larger squares should give cancellation at lower frequencies through choice of the height difference. The structure with three interwoven checker boards as described above is investigated by a simple numerical model. A contour plot of the height differences of the surface with such a pattern is shown in Figure 4.3. Slightly more than four by four of the larger squares (two by two of the larger periods) are shown.
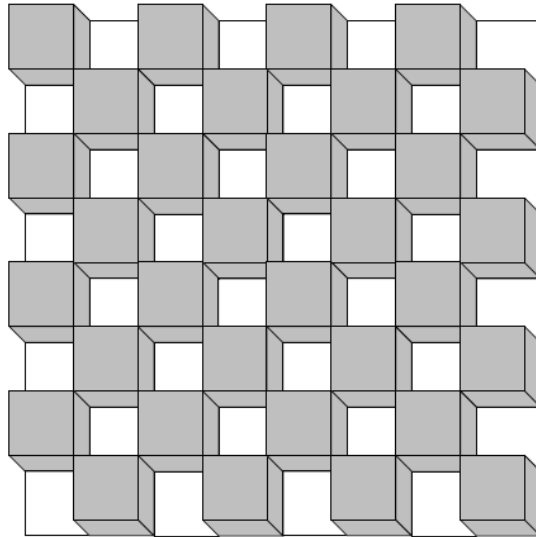
Figure 4.2: Backing structure with checkerboard pattern.

This structure is fairly easy to analyze, and a plot of an obtained specular reflection coefficient versus frequency is shown in Figure 4.4. The heights are chosen to give cancellation of specular reflection at 15.2 MHz, 24.7 MHz, and 36.1 MHz. The cancellation at about 46 MHz is due to a 1.5λ delay difference for the 15.2 MHz structure. It is therefore less locally balanced than it could have been at this frequency. The frequencies in this example are chosen to demonstrate the effect upon the specular reflection coefficient over a range of frequencies. It is clear from the figure that this type of
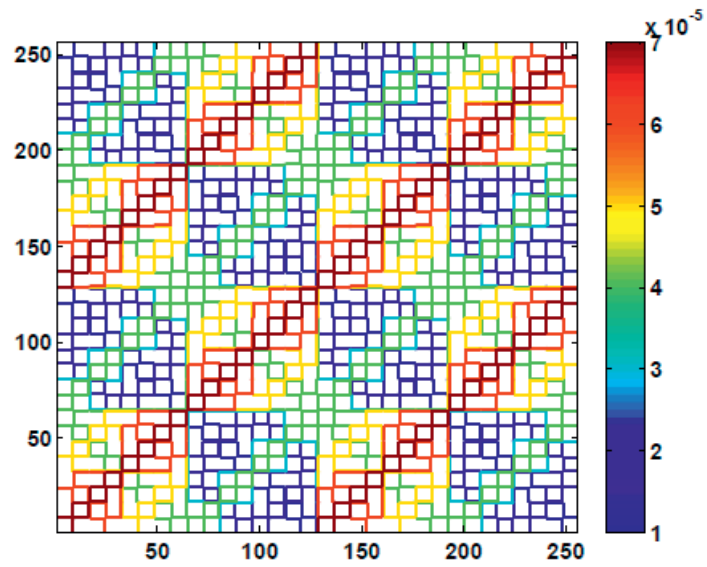
Figure 4.3: Contour plot of the heights for a part of the interwoven checker board pattern.

structure minimizes the specular reflection over a wide frequency band.
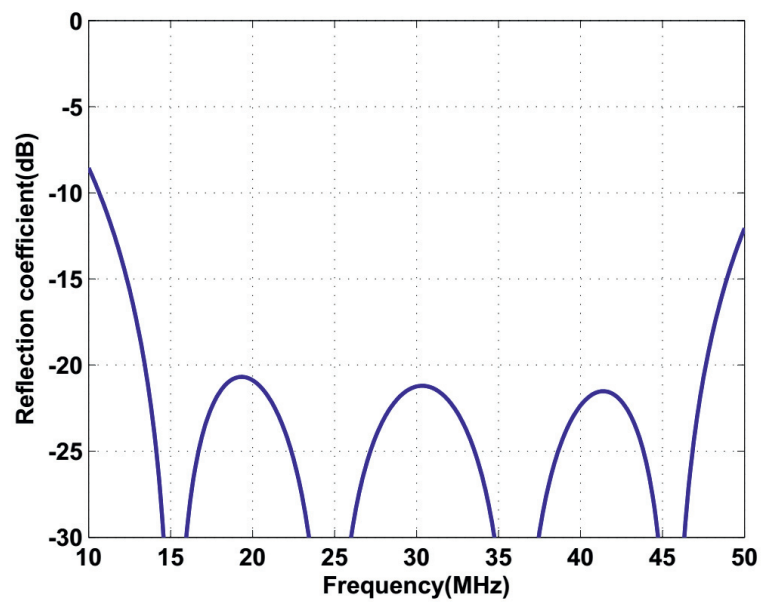
Figure 4.4: Specular reflection coefficient from the checker board structure versus frequency

The structure discussed above works well for a frequency range but it gives large differences in linear dimensions between the low frequency and high frequency scatterers, with a factor of 2^n for a null at n frequencies. To obtain many nulls in the reflection, this means that the smallest area with full balance in reflections become fairly large. To avoid this, we could use other patterns. It is possible to use parallel grooves which have the same distance between grooves as the groove width. If we want several groove structures overlaid on top of each other such that they are all active at the same time, and balanced as described above, we may use different directions for grooves with different depth and possibly different width which are designed to make them active at desired frequencies.

Another possible structure is a basic pattern of two triangles which together forms a square or a rectangle. A structure which forms a balanced depth pattern combined with this could be the structure which is obtained if the square or rectangle is divided into triangles by the other of the two possible diagonals. Such a structure is shown in Figure 4.5 which gives cancellation of specular reflection at two independent frequencies specified by the heights h_1 and h_2. To get cancellation of specular reflection over even broader frequency range, one could repeat the same structure with rectangles/squares where the dimensions in the plane are scaled up or down by a factor of two.
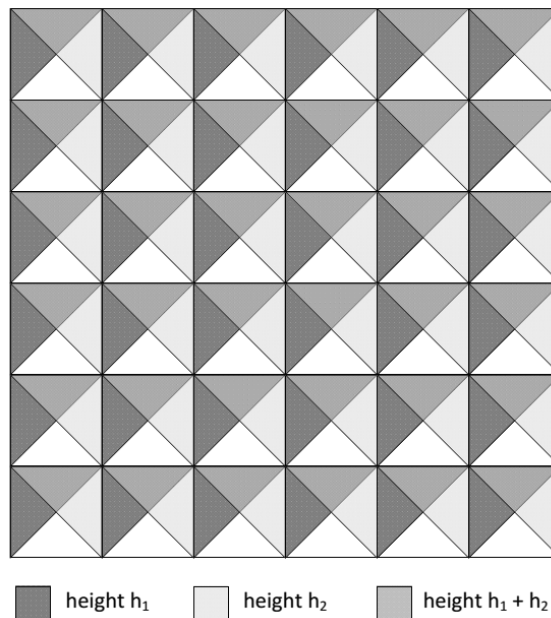
Figure 4.5: Possible backing structure with interwoven triangular pattern.

4.3   Grooved backing structure

Among the different possibilities, parallel grooves with an interwoven structure that provide nulls in specular reflection at two different frequencies is chosen in this work. This gives a low value of the specular reflection coefficient over a frequency range covered by these two frequencies. To get nulls at two different frequencies, four different groove heights are to be made as there should be 2^n number of groove depths to get nulls at n different frequencies. This structure is chosen because it is comparatively easier to create than other structures discussed earlier. Simulations performed for such structures in COMSOL Multiphyics will be presented in Chapter 5 and details on how this type of structure could be fabricated will be discussed in Chapter 6.

Two different designs are used, one symmetric and one asymmetric. Neglecting the effects of vertical surfaces and corners, both designs should provide the same result but they can have different advantages/disadvantages in actual applications. The two groove heights, h_1 and h_2 as shown in Figure 4.6 and 4.7 are chosen so that they correspond to quarter wavelengths at the two specified frequencies, f_1 and f_2. The frequency range where the value of the specular reflection coefficient becomes low is determined by these two frequencies. For a particular case when f_1 and f_2 are 16 MHz and 25 MHz, the specular reflection coefficient is calculated for this type of structure. The obtained plot is shown in the Figure 4.8. As it could be clearly seen from the figure, beside the two nulls at 16 MHz and 25 MHz, the specular reflection coefficient is less than 15 dB for a range of frequency from 12 MHz to 28 MHz.
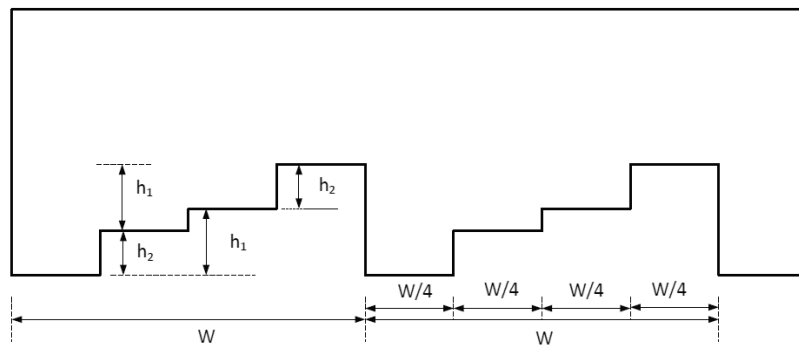
Figure 4.6: Grooved bottom structure with asymmetric design; only two periods of the structure are shown.
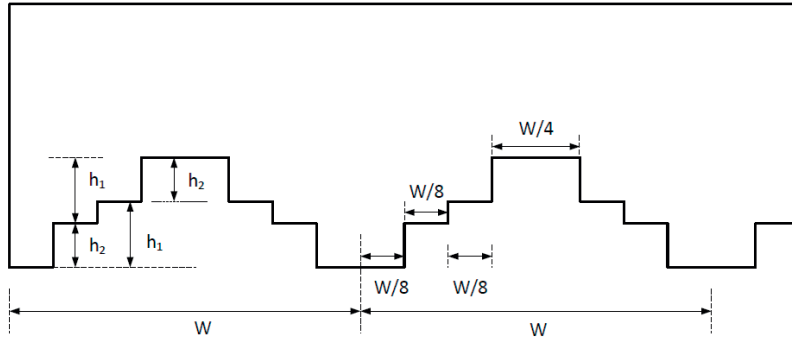
Figure 4.7: Grooved bottom structure with symmetric design; only two periods of the structure are shown.
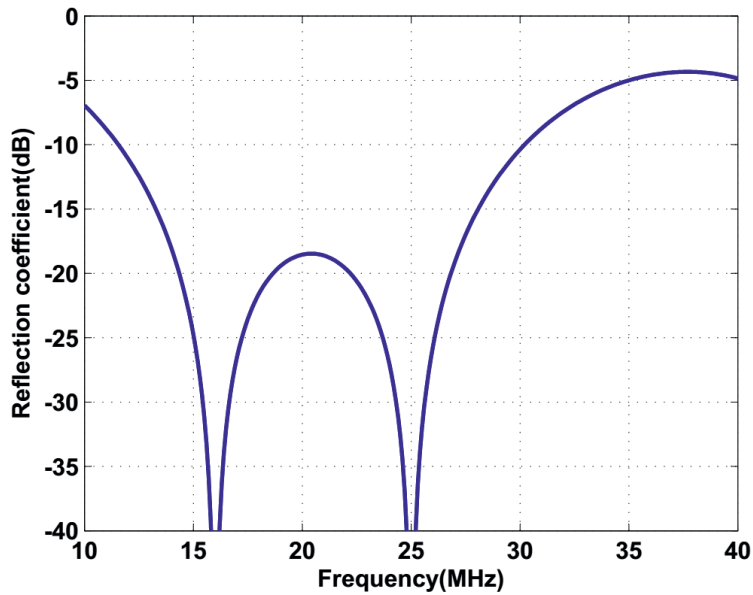
Figure 4.8: Reflection coefficient for grooved bottom structure, both for symmetric and asymmetric design.

The structures shown here are periodic structures with a period W. Thus the width for each step would be equal to one-forth of the period, $W/4$. The structures shown here are similar to the contour plot shown in Figure 4.3, except that the contour plot has an interwoven structure in both x and y directions, whereas the structuring in Figure 4.6 and 4.7 is only in

one direction.

To cover a broader frequency range, three frequencies could be chosen. But it requires eight different step heights which could be more challenging to make. It is clear that the groove heights become smaller when the frequencies chosen becomes higher since they corresponds to a quarter of the wavelength. For cancellation at higher frequencies, the groove heights becomes so small that roughening the bottom side of the structure by few microns would contribute to attenuation of waves by scattering. CMUT transducers normally have bandwidth larger than 100%, and for high frequency transducers the bandwidth covers a broad range of frequencies. Thus to obtain an added attenuation for both lower and higher band of frequencies, one could use similar structures as shown in Figure 4.6 and 4.7 with its bottom surface roughened by a few microns. This roughening of the surface could be done randomly to get the scattering over a range of frequencies rather than at a particular frequency.

4.4 Wave propagation in a CMUT backing stack

A CMUT array on a silicon substrate with a grooved backing structure operating in a fluid medium is illustrated in Figure 4.9. In this section we focus on issues related to surface waves and the excitation of bulk waves in the substrate, not on fluid coupled crosstalk due to neighbor coupling of CMUT arrays. The silicon substrate shown in the figure may consist of several silicon wafers for electronics with bonding layers in between. After propagating through the substrate and backing, the bulk waves may reflect back into the fluid medium. This results in a delayed transmit signal echo and thus degrade the response of the CMUT.

When ultrasound transducers are used for medical imaging, the resulting echo signal from the backing must be suppressed compared to the main signal to avoid image degradation. The requirements for suppression depend on the required dynamic range of the imaging system, which may vary with the medical applications. Somewhat arbitrarily we choose this to be 40 dB in transmission or reception in this work. Referring to Figure 4.9, if A is the main signal and D is the resulting echo signal, we can write

$$\left(\frac{D}{A}\right)_{\text{dB}} = \left(\frac{D}{C}\right)_{\text{dB}} + \left(\frac{C}{B}\right)_{\text{dB}} + \left(\frac{B}{A}\right)_{\text{dB}} \leq -40 \text{ dB} \quad . \qquad (4.3)$$

The grooves created at the bottom of the backing will reduce the specular reflection from the backing and therefore reduce the second term of equation (4.3). This will be discussed in more detail in Chapter 5. In this
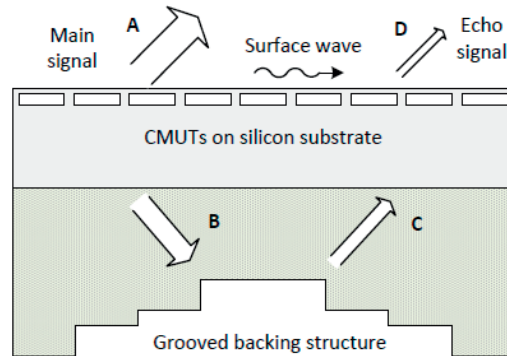
Figure 4.9: A typical scenario for CMUT arrays on silicon substrate with grooved backing structure operating in a fluid medium.

section, we discuss how factors other than the reflectivity of the backing influence the signal degradation for the CMUT array. To get an estimate of these factors, we calculate the first and the last terms of equation (4.3) when well backed CMUT transducers are excited in a fluid medium. The first term of the equation gives the coupling of the acoustic signal reflected from the backing into the fluid medium, and the third term gives the acoustic signal transmitted into the backing relative to the signal transmitted into the fluid medium. In the discussion, we assume water as the fluid medium and look in detail at the transmission case, but due to reciprocity the results are valid also in reception. The theory considers plane waves propagating in several media bounded by infinite, parallel interfaces based on Auld [Aul90]. The backing material is assumed to be cured directly at the bottom of the silicon substrate without any glue layer. The waves excited in various layers due to CMUTs vibrating on top of the silicon substrate are shown in Figure 4.10. The center frequency of the CMUT is chosen to be 25 MHz. This gives the 100% bandwidth of the transducer from 12.5 MHz to 37.5 MHz. The grooved backing structure which will be discussed in Chapter 5 should therefore provide low specular reflection for this frequency range.

There is a wide variety of possible CMUT designs. For the calculations in this section we assume a simple idealized CMUT structure. It is a massless layer between the fluid and the substrate which may be expanded and compressed vertically in response to an exciting voltage. This gives its top surface a vertical velocity, v_{ex}, compared to its bottom surface. It has an acoustic impedance which matches to the impedance of the fluid for all steering angles, provided that the substrate is infinitely stiff. A real CMUT will differ from this idealized model in several ways. It will include mass in the
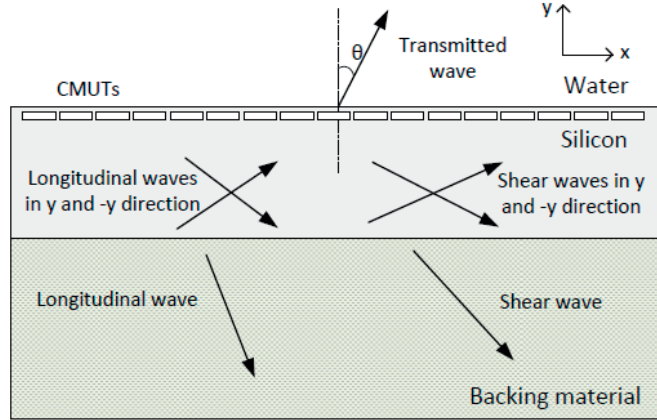
Figure 4.10: Transmitted wave into water, and transmitted longitudinal and shear waves in silicon-backing stack operating in water when CMUTs on top of the silicon substrate are excited.

CMUT plate and there will be reactive forces accelerating the fluid. Further, limited coupling coefficient and electrical parallel capacitances means that the CMUT will not be electrically matched to the acoustic load as assumed here. This will in most cases mean that at the center frequency the CMUTs will be acoustically softer than given by our model. The forces acting on the substrate will be non-uniform on the scale of CMUT and element diameters. However due to the high acoustic velocities in silicon compared to water, it will only be an average value of these forces that excite the propagating waves in silicon. Even though the calculation shown here is for an idealized CMUT, which cannot be realized, we believe it gives for many cases a conservative estimate of the degradation for reasonably designed CMUTs over a large bandwidth.

The material properties of the silicon and the backing used in the calculations are shown in Table 4.1. Silicon is considered here as an isotropic material with a Young's modulus of 160 GPa and a Poisson's ratio of 0.22. The material properties of the backing material are chosen to match it fairly well acoustically to silicon for normal incidence of longitudinal waves. The longitudinal and shear loss factors for the backing material are chosen to be 0.08 and 0.8, respectively. These loss factors account for absorption losses in the backing material. This will be discussed in more detail in Chapter 5 describing modeling of loss for the grooved backing structure. The thicknesses of the silicon are chosen to be 60 μm and 100 μm. When CMUTs on top of the silicon substrate are vibrating, longitudinal and shear waves are excited in various layers of the stack. Each layer is characterized by four waves:

two longitudinal and two shear waves propagating or damped in positive
and negative y-directions. The backing material in this section is assumed
to be thick enough so that no waves are reflected back from the bottom of
the backing. Therefore the backing layer is characterized by only two waves
propagating or damped in negative y-direction as shown in Figure 4.10.
Horizontal shear waves are not taken into account in the calculations. The
amplitudes of particle velocities of different transmitted and reflected waves
shown in Figure 4.10 are formulated by calculating particle velocities and
stresses for each layer as described by Auld [Aul90]. Using continuity of ve-
locities and stresses at the boundary between the two media, the equations
are solved to calculate the amplitudes of reflected and transmitted longi-
tudinal and shear waves in all layered media. Similar formulation has also
been shown by Brekhovskikh [BB60] for calculations of reflection and trans-
mission coefficients for elastic waves in solid layered media using a transfer
matrix approach.

Table 4.1: Material properties of silicon and backing material.

Material	Density (kg/m^3)	Longitudinal ve-locity (m/s)	Shear velocity (m/s)
Silicon	2340	8836	5294
Backing	9000	$2000\left(1+j\frac{0.08}{2}\right)$	$1000\left(1+j\frac{0.8}{2}\right)$

The amplitudes of particle velocities of different waves when the CMUT
array is excited at 25 MHz frequency are calculated for the two different
thicknesses of the silicon substrate for different steering angles. The ratio
of amplitudes of the particle velocity in water to the exciting velocity, v_{ex},
of the idealized CMUT structure are shown in Figure 4.11. As the wave
velocity in water is much smaller than the wave velocity in silicon, angles
that the longitudinal and shear waves in the silicon make with the surface
normal are much larger than the angle in water. At an angle of about 10°
in water, the longitudinal wave in silicon propagates along the surface. For
larger angles, the longitudinal wave in silicon is evanescent. At an angle of
about 17°, the shear wave will propagate along the surface. These angles
are also known as the first and the second critical angle for the interface
[RD00]. Dips are clearly observed at these angles for a thick silicon layer.
For an angle slightly above the second critical angle, there is an existence
of a wave propagating along the surface which is the SAW wave modified
by the backing. This effect is more pronounced when the thickness of the

silicon is increased further above 100 μm. As the SAW is exponentially damped into the silicon substrate, the substrate should be thin compared to the characteristic wavelength in order to allow the acoustic backing layer at the bottom of the substrate to absorb these waves. This could be seen in Figure 4.11 for 100 μm substrate compared to 60 μm substrate where the dip in the response above 17° steering angle is much reduced for 60 μm substrate. The result shown in Figure 4.11 supports the conclusion made by Berg *et al.* [BR12] that a well backed 60 μm silicon substrate may be used to carry CMUTs with a 25 MHz center frequency.
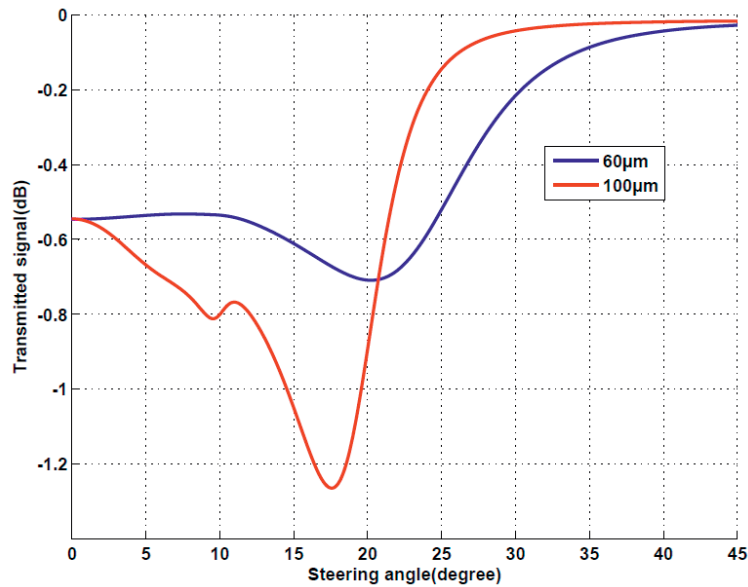
Figure 4.11: Amplitude of particle velocity in water compared to amplitude of exciting velocity, v_{ex}, of the CMUT structure when CMUTs on top of the silicon substrate are excited at 25 MHz for two different thicknesses of silicon.

In this work we make grooves at the bottom of the backing material. Therefore we are interested in longitudinal waves transmitted into the backing material. As the shear waves have much higher losses than the longitudinal waves, they are properly attenuated in the backing. The amplitudes of longitudinal waves at the top of the backing are shown in Figure 4.12 for the two different thicknesses of the silicon. These are 20-30 dB below the transmitted longitudinal wave in water and the values will be even smaller when they are reflected back from the bottom as they are partly absorbed in

the backing structure and partly scattered by the grooves. This also applies for the waves above 20° to 30° steering angle which are already small at the top of the backing. Therefore, for incidence angles above these values, the reflected waves will cause small perturbations only. This gives us an estimate of the third term of equation (4.3). To get an estimate of first term of equation (4.3), a similar calculation is repeated for a longitudinal wave excited at the top of the backing towards silicon and water. The transmitted longitudinal wave in the water is then calculated. The obtained results are shown in Figure 4.13 for the same two thicknesses of silicon. The velocity amplitude of the transmitted wave in water in this case is about 0-10 dB below the input longitudinal wave velocity. It also decreases rapidly above 20° to 30° steering angle in water for both thicknesses of the silicon substrate.
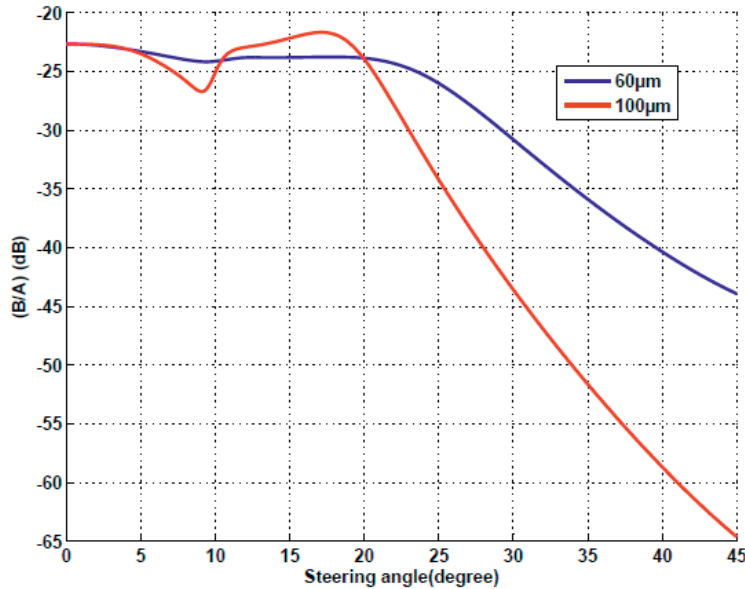
Figure 4.12: Amplitude of particle velocity of transmitted longitudinal wave at the top of the backing (B) compared to amplitude of particle velocity in water (A) for two different thicknesses of silicon versus steering angle in water.

The results shown here are for the idealized CMUT model. Referring to Figure 4.12, in a real CMUT there will be reactive forces accelerating the CMUT membrane and the fluid, and these forces will make the force on the fluid and the silicon different; not equal as assumed in the model. However as those forces are in quadrature with the radiation forces, the amplitude of
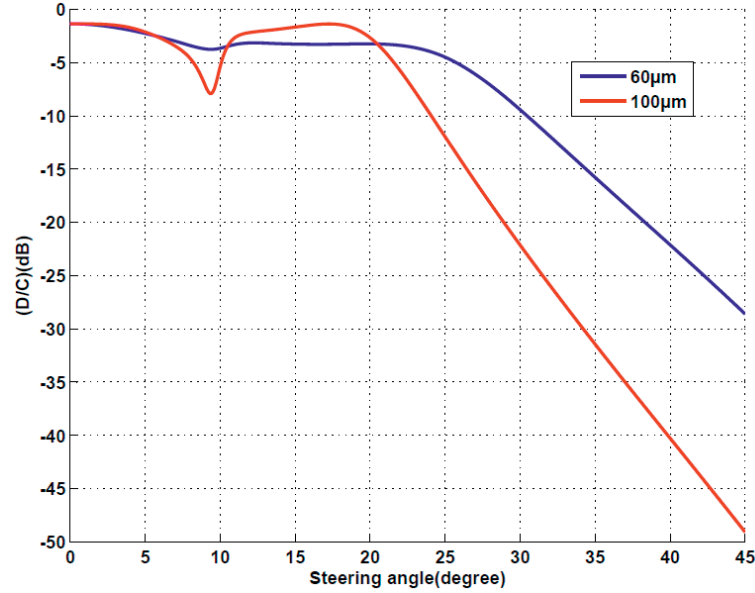
Figure 4.13: Amplitude of particle velocity of transmitted wave in water (D) compared to amplitude of particle velocity of longitudinal wave in the backing (C) for two different thicknesses of silicon versus steering angle in water.

the force on the substrate will not change much. As mentioned earlier the acoustic impedance of the CMUT around the center frequency is probably much smaller than assumed here in our model. This would mean that the CMUT layer is easier to compress than we have assumed, and hence less movement will be transferred to the fluid compared to our result in Figure 4.13. This is probably the largest difference between our model and a real CMUT structure.

From our calculation we know that a 60 μm or thinner silicon substrate works well for degradations due to SAW, whereas thicker substrates are better for bulk wave reduction, especially at higher steering angles. We look at the combined echo suppression from the first and the last terms of equation (4.3) for a 60 μm thick silicon substrate versus steering angle, 0° to 45°, and frequency, 10 MHz to 40 MHz. This is shown in Figure 4.14. At high steering angles our goal of 40 dB suppression is obtained from these terms alone at high frequencies. For steering angles up to 20° to 30°, the combined echo suppression is 25-30 dB for essentially the whole frequency range. This means that an additional 10-15 dB attenuation in the backing

is required to avoid signal degradation in CMUT arrays. Therefore the grooved backing structure should provide this value for 100% bandwidth of the transducer for steering angles up to 20° to 30°.
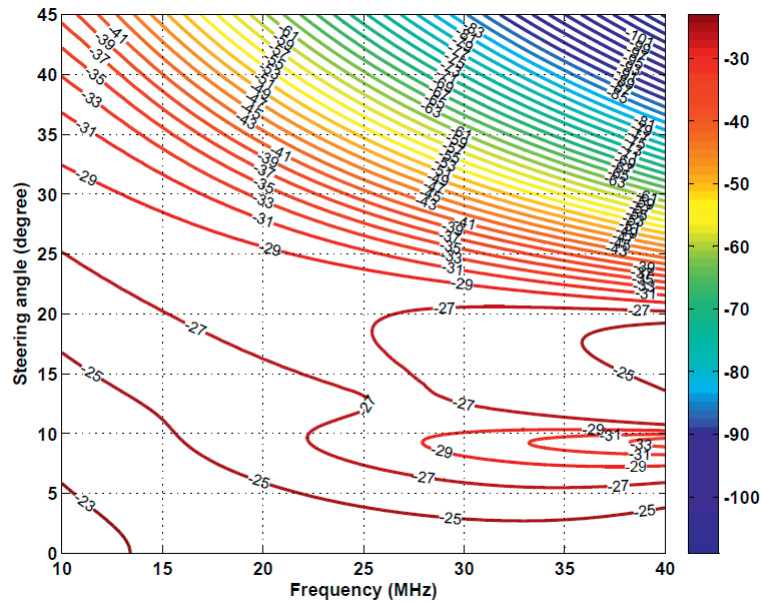
Figure 4.14: Combined echo suppression (dB) from the first and the last terms of equation (4.3) for 60 μm thick silicon substrate as a function of frequency and steering angle in water, 2 dB between contour lines.

Chapter 5

Simulation of Grooved Backing Structures

In this chapter we describe the simulation of the grooved backing structure for CMUT transducers. The grooved backing structure is simulated using the finite element analysis software COMSOL Multiphysics (version 3.5a) while the results are post-processed in Matlab. In the first section of this chapter, we briefly discuss what the finite element method is and how it can be used. We then show how finite element analysis is used in this work with simulation results obtained for some specific cases.

5.1   Introduction to FEM

Many physical phenomena in engineering and science are generally modeled by differential equations, and solving these equations by classical analytical methods becomes complicated in many cases. The finite element method (FEM) is a numerical approach by which these differential equations can be solved approximately. The FEM is a function based approach to solve the differential equations. It is widely used in diverse fields such as solid/fluid mechanics, acoustics, electromagnetics,etc to solve static and dynamic problems.

   The differential equations which describe a physical problem are assumed to hold over a certain region known as a *domain*. The domain may be 1D, 2D or 3D. In the finite element method, the domain is divided into smaller parts called *elements*. In 1D, an element is a line segment. In 2D, an element is some sort of polygon which can be used to fill the entire area, such as a triangle or a rectangle. In 3D, polyhedrons together with other similar elements could be used to fill the entire volume. The collection of all such

elements is known as the *finite element mesh*. A typical triangular element and corresponding finite element mesh for a simple structure is shown in Figure 5.1.

         (a) triangular element   (b) finite element mesh
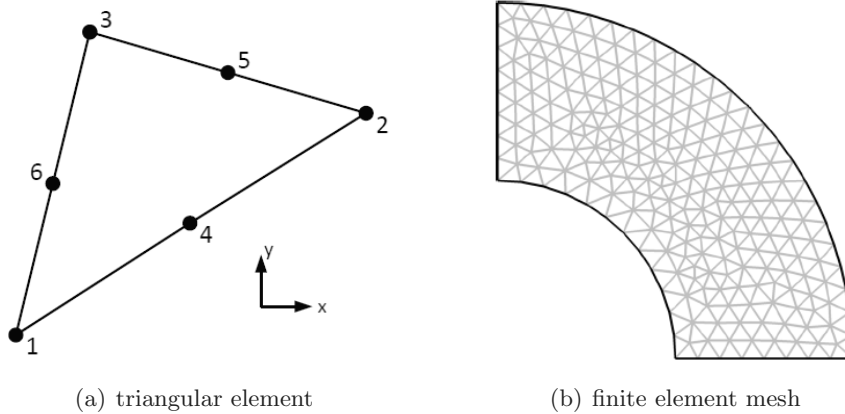
Figure 5.1: Typical triangular element with six nodes and corresponding finite element mesh for a structure.

The characteristic feature of FEM is that an approximation is carried out over each element to find its behavior instead of doing it over the entire domain. This approximation is usually a polynomial, where linear and quadratic approximations are mostly used. After the behavior of each element is determined, they are patched together using some specific rules, to form an entire region. This gives the approximate solution for the entire region [OP92]. A simple demonstration of such a method is shown in Figure 5.2 for a one-dimensional case where the entire region is divided into five elements and linear approximation is used to get the temperature distribution, $T(x)$, along a body.

The corners of the elements are known as *nodes*. In FEM, we solve for the unknown variables at each node and the values of the variables in the region between the nodes are calculated using shape functions. These shape functions are decided before the calculations and are often indicated by the name of the element type - linear elements, quadratic elements, etc. For each node in the element, there will be a shape function N_i that is unity at node i, but zero at all other nodes. In addition, the sum of all the shape functions will be unity for all points in the element. If we consider $\tilde{u}_i$ as the value of dependent variable for the ith node with shape function N_i, the approximate value of the dependent variable, $\hat{u}$, within an element is given
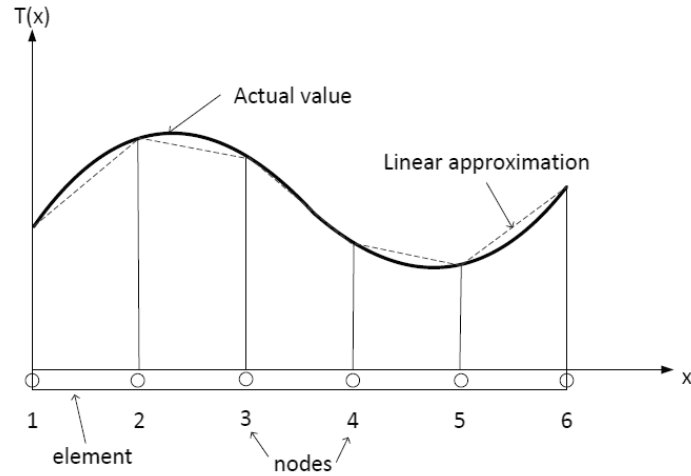
Figure 5.2: Approximation of a temperature distribution along a body using five elements with linear variation within an element.

by [ZTZ05]:

$$u \approx \hat{u} = \sum_{i=0}^{n} N_i \tilde{u}_i \quad , \tag{5.1}$$

where n is the number of nodes associated with the element, and u is the exact value of the dependent variable.

A problem in a physical domain leads to a set of differential equations and boundary conditions. The differential equations and the boundary conditions together are referred to as the *strong form* of the problem. The strong form contains higher order differential terms, which are reduced to lower order terms in its equivalent *weak form*. And it is the weak form that the finite element formulation is based on. The weak form is often an integral form and requires a weaker continuity on the field variables compared to the strong form. For example, in the strong form with second order derivative terms, the approximation function should be at least twice differentiable whereas it could be linear in its equivalent weak form. This is the main advantage of using the weak form.

To convert the strong form into a corresponding weak form, the *weighted residual method* is often used. The finite element method gives an approximate solution. Thus if we substitute the approximate value of the unknown variable in the differential equation, the right hand side of the equation will not be exactly zero. This value is known as *residual*. The FEM does not attempt to make this residual equal to zero, rather it tries to make the

weighted average residual zero. For this purpose, the differential equation
is multiplied by a weighting function, W, and integrated over the entire do-
main [OP92]. Different types of weighting functions are used with different
methods such as the point collocation method, the sub-domain collocation
method, the least squares method, Galerkin's method, etc. In the point col-
location method, the weighting functions are chosen as Dirac- δ functions
which forces the weighted residual to zero at specific points in the domain.
In sub-domain collocation method, the weighted residual is forced to zero
not only at the fixed points in the domain but also over various subsections
of the domain. In the least squares method, the continuous summation of
all the squared residual is minimized. But the most commonly used method
is Galerkin's method which may be viewed as a modification of the least
squares method. In this method, the shape functions themselves are chosen
as weighting functions, i.e.

$$W_i = N_i \quad .\tag{5.2}$$

Based on the above discussion, the basic steps involved in the finite
element analysis can be summarized as follows:

- The problem to be solved is described in terms of differential equations
  and its approximation is derived by constructing the weak form.

- The type and order of the elements to be used in the analysis are
  selected.

- The mesh is defined for the problem. This involves the description of
  the node and element layout, as well as the specification of boundary
  conditions and parameters for the form used.

- The element arrays are computed evaluating the integral form for each
  element and assembled as a global matrix equation.

- The resulting set of linear algebraic equations for the unknown pa-
  rameters are solved.

- The results for the nodal and element variables can be obtained from
  the solution.

5.2   FEM simulation of grooved structure

For the finite element simulation of the grooved backing structure, COM-
SOL Multiphysics (version 3.5a) is used. It is a simulation program that

employs the finite element method to solve complex physical problems governed by partial differential equations (PDEs). COMSOL is a powerful tool as it is possible to couple different physical domains for a better understanding of the problem. However, in this work, this multiphysics property of COMSOL is not utilized. The finite element modeling with COMSOL uses the following basic steps:

- Defining the geometry and the meshing.

- Setting properties for the physical domain.

- Setting boundary conditions.

- Selecting solving procedure and solving the equations.

- Performing post-processing.

The different steps involved for the simulation of the grooved backing structure using COMSOL Multiphysics are described in brief in the following sections.

5.2.1 Governing equations

For simulation of the grooved backing structures, the structural mechanics module of COMSOL is used. This module is used for the analysis of components and subsystems when it is necessary to evaluate the deformations under loads. The analysis is performed here for a 2D case. Plain strain formulation is used to study the displacements, the stresses, and the strains. As this type of structure should provide a low specular reflection coefficient over a wide frequency range, the frequency response analysis is performed by solving the steady-state response from harmonic excitation. The excitation frequency is swept over a range using a parametric solver. The equation governing the plane strain mode is shown below [OP92]:

$$
\begin{bmatrix} \sigma_{xx} \\ \sigma_{yy} \\ \sigma_{xy} \end{bmatrix} = \frac{E}{(1+\nu)(1-2\nu)} \begin{bmatrix} 1-\nu & \nu & 0 \\ \nu & 1-\nu & 0 \\ 0 & 0 & \frac{1}{2}(1-2\nu) \end{bmatrix} \begin{bmatrix} \epsilon_{xx} \\ \epsilon_{yy} \\ \gamma_{xy} \end{bmatrix} - \frac{\alpha E \Delta T}{(1-2\nu)} \begin{bmatrix} 1 \\ 1 \\ 0 \end{bmatrix},
$$
(5.3)

where σ_{xx}, σ_{yy}, and σ_{xy} are the stresses, ϵ_{xx}, ϵ_{yy}, and γ_{xy} are the strains respectively in longitudinal and shear directions, E is Young's modulus of elasticity, ν is Poisson's ratio, α is the thermal expansion coefficient, and ΔT is the change is temperature. The second term of the right hand side

of equation (5.3) gives strains caused by thermal expansion of the material. These strains are also referred to as *thermal strains*. To make the calculations simpler, the ΔT temperature variation is not used in our simulations.

From equation (5.3), it is clear that the in-plane strains directly determine the in-plane stresses and vice-versa. However, in this module of COMSOL, the output from the solution are displacements in x and y directions from which other quantities could easily be determined.

5.2.2   Defining the geometry and domain parameters

The main goal of the simulation is to study the specular reflection of waves from the bottom of the grooved structure. The geometries for the structure are defined as shown in Figure 5.3. The backing material chosen here is a composite of epoxy and tungsten powder. The longitudinal velocity for the composite is chosen to be 2000 m/s and the density is chosen to be 9000 kg/m^3 in this work using the Devaney model as described earlier in Chapter 3.
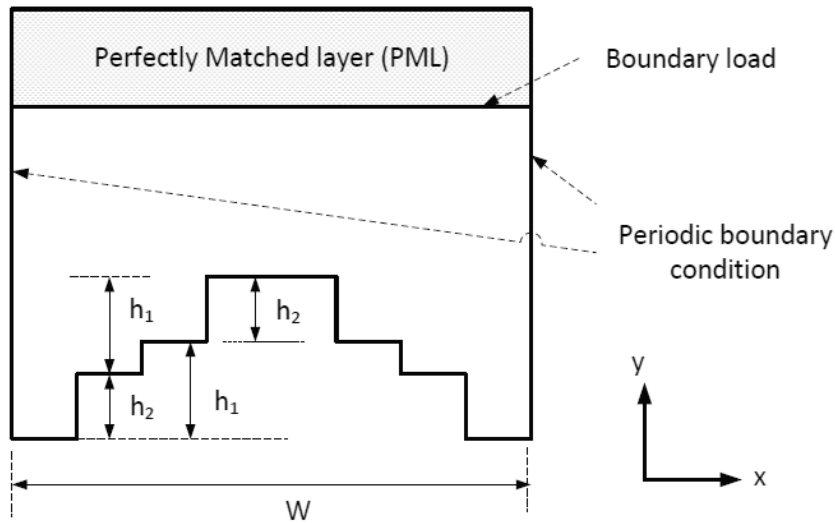
Figure 5.3: COMSOL simulation for a grooved backing structure (figure is not to scale).

In the structural mechanics module, a material can be defined in terms of its Young's modulus, Poisson's ratio and density. For these calculations, we assume that tungsten epoxy composite behaves as a homogeneous isotropic material. Using the values for velocity and density obtained from the De-

vaney model, the Young's modulus obtained for the composite is 24.3 GPa with a Poisson's ratio of 0.33.

To emphasize the effect of the scattering from this type of structure, we have set the absorption losses in the composite material to zero in these calculations. The effect of finite losses within the composite material will be discussed in Section 5.3. A uniform harmonic force is applied in y-direction to excite a plane wave propagating in a direction normal to the bottom of the structure. The "Boundary load" feature of COMSOL is used to represent such waves. In Section 5.5, we will also deal with waves that are incident from oblique directions. To generalize for both normal and oblique incidence cases, a more general expression is set up for the k-vector and its components as a function of incident angle θ and frequency f. The k-vector and its components are shown in Figure 5.4 where $k_0 = \dfrac{2\pi}{\lambda} = \dfrac{2\pi f}{v_l}$ is the magnitude of the k-vector. The generalized term for the "boundary load" could then be represented by $Ae^{-j(k_x x + k_y y)}$, where A is a constant.
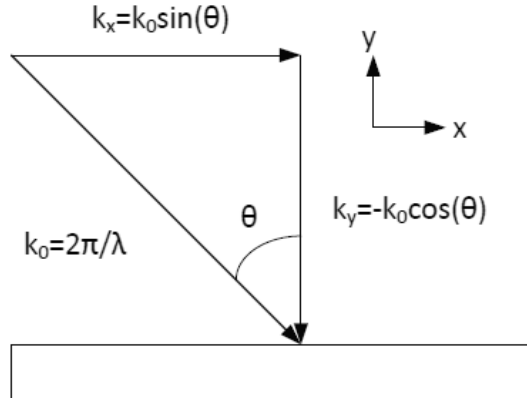
Figure 5.4: General expression for the k-vector and its components as a function of incident angle.

As we know the longitudinal wave velocity in the structure, the values for different groove depths h_1 and h_2 can easily be obtained. The grooved structure is designed to give nulls in the reflection coefficient at two frequencies, 16 MHz and 25 MHz. This gives the values of h_1 and h_2 respectively as 31.25 μm and 20 μm with a longitudinal velocity of 2000 m/s. The total period of the structure is chosen to be 600 μm, which gives a cumulative total width of each step of 150 μm. The height of the structure is taken to be 650 μm and the thickness of a perfectly matched layer (PML) layer, see next paragraph, is taken to be 400 μm.

5.2.3   Perfectly matched layer (PML)

For the structures, our interest is to find how much of the incident energy is specularly reflected by the grooves. Thus the top layer of the structure is used as a non-reflecting boundary so that the specularly reflected wave and other back-scattered waves are absorbed in it. To emulate the non-reflecting boundary, the PML feature of COMSOL is used. The concept of PML was introduced by Berenger [Ber94] as a layer designed to absorb electromagnetic waves without reflection. PML is a domain in COMSOL that absorbs all the incident radiation without producing reflections. It provides good performance over a wide range of incidence angles. It could be created in any coordinate system. In this case, we have used cartesian PML type with absorption in y-direction so that the reflected wave from the bottom would be absorbed in the PML layer on the top. For a PML that absorbs waves in coordinate direction ξ, the implementation uses the following coordinate transformation inside the PML [Com08]:

$$\xi^{'} = sign(\xi - \xi_0)|\xi - \xi_0|^n \frac{L}{d\xi^n}(1 - i) \quad , \qquad (5.4)$$

where L is the scaled PML width, ξ_0 is the coordinate of the inner PML boundary, $d\xi$ is the actual PML width, and n is the scaling exponent whose values lies between 1 and 2. The value of L is usually set to one wavelength. In frequency response analysis, the wavelength varies for different frequencies, then the value for the scaled PML width is set to the longest wavelength for the PML to function properly. For longitudinal waves in elastic isotropic solids, the wavelength is given by:

$$\lambda = \frac{1}{f}\sqrt{\frac{(1 - \nu)E}{(1 + \nu)(1 - 2\nu)\rho}} \quad , \qquad (5.5)$$

where f is the frequency, E is the Young's modulus, ν is the Poisson's ratio and ρ is the density of the material.

For the oblique incidence case, this scaled PML width, L, should be divided by the absolute value of the cosine of the input angle in order to preserve the same amount of attenuation as in the case of normal incidence [Com08].

5.2.4   Boundary conditions

To make the calculations simpler, only one period (600 μm in this case) of the structure is used in the simulation. Periodic boundary conditions are used to make the structure act as if it is infinite in x-direction. To apply

the periodic boundary conditions in COMSOL, a homogeneous Neumann boundary condition is to be used on the boundaries where the periodicity is required. This boundary condition corresponds to the free (no constraints or no loads) boundary condition in the structural mechanics module. To apply periodic boundary conditions in x-direction means that if u and v are the displacements in x and y directions at the left side of the structure, the corresponding displacements on the right side of the structure are required to be ue^{-jk_xW} and ve^{-jk_xW} respectively. Here k_x is the x-component of the k-vector of the exciting force, and W is the period of the structure in x-direction. The bottom surface of the structure is kept free. This means that all the incident waves will be reflected back into the medium without any loss at the interface.

5.2.5 Meshing and solving

In the simulation, triangular elements are chosen to generate the finite element mesh. As the frequency response analysis is used, the wavelength varies as the frequency varies from lowest to highest value in the range. The mesh size is chosen such that one wavelength consists of at least 8 to 10 elements. The order of the shape functions can be set in the physical domain, ranging from linear to quintic. However, quadratic Lagrange element, which is also the default setting in COMSOL, is chosen in this case. All simulations were solved with standard settings for the solvers. The frequency was scanned from 10 MHz to 40 MHz to include the two frequencies, 16 MHz and 25 MHz, where nulls in the specular reflection are desired.

5.2.6 Post-processing

Although there are post-processing and visualization options in COMSOL, Matlab is chosen for post-processing of the result because of its greater flexibility. COMSOL has a feature which enables generation of a matlab file which could be used for further processing. It is also easier to modify the geometry and other parameters using this approach. The output from the structural mechanics module are displacements in x and y directions from which velocities in both directions could easily be obtained. The longitudinal and shear stress components could also be obtained from the result. After these parameters are found, the amplitudes of the waves traveling in different k-directions can be calculated at a cross section of the structure using the Fourier transform. As the amplitudes of waves traveling in different directions are known, the reflection coefficient of the waves from the grooved structure could easily be determined.

5.3   Modeling of acoustic attenuation in COMSOL

In the first part of the simulation, the absorption loss in the material is not included to study the attenuation provided solely by the grooves. But for a realistic modeling of the grooved backing structure, the acoustic attenuation in the composite material should also be included. In Chapter 3, we have discussed how acoustic attenuation could be modeled. In this section we will describe how the model described earlier could be implemented in COMSOL. Two different models exist for damping in COMSOL which are briefly discussed here. One is the *Rayleigh Damping*, and the other is *Loss factor damping.*

In most viscous damping models, a dashpot is used as a damping element where damping is assumed to be proportional to velocity. In Rayleigh damping model, this damping matrix, C, is defined in terms of the mass, M, and the stiffness, K, matrices as shown below:

$$[C] = \alpha[M] + \beta[K] \quad , \tag{5.6}$$

where α and β are the constants used to set the amount of damping. These constants are also known as Rayleigh damping parameters.

It is possible also to transform the Rayleigh damping parameters to an equivalent loss factor. For specified damping parameters α and β, the loss factor η at a frequency f can be determined by [LG95]:

$$\eta = \frac{\alpha}{2\pi f} + \beta 2\pi f \quad . \tag{5.7}$$

The Rayleigh damping model is used by many computer programs to model the effect of viscous damping. From equation (5.7), it is clear that when $\beta = 0$, very little damping is assigned to higher frequencies. But when $\alpha = 0$ and $\beta \neq 0$, these frequencies are heavily damped. Thus the parameters should be chosen in order to provide an appropriate amount of damping for different frequencies. But the problem with this model is to get good values for the different damping parameters. Also the assumptions of both mass and stiffness proportional damping have effects which are difficult to justify physically.

In this work, we use the loss factor damping described earlier in Chapter 3. In Structural mechanics module of COMSOL, a material is modeled with the help of Young's modulus and Poison's ratio. COMSOL also has a built in loss factor model. But it uses uniform loss in both longitudinal and shear directions, which is not realistic as the viscous loss is higher for shear waves than for longitudinal waves. Thus we are using complex values for Young's

modulus (E) and Poisson's ratio (ν) to represent the loss. The complex values for both E and ν could be obtained by using equation (3.19), see Chapter 3, for a lossy composite material, which are rewritten here:

$$
\begin{aligned}
v_l{}^2 &= v_l'^2 (1 + j\eta_d) \quad, \\
v_s{}^2 &= v_s'^2 (1 + j\eta_s) \quad,
\end{aligned}
\tag{5.8}
$$

where η_d and η_s are the dilatational and the shear loss factors.

The backing material is assumed to be an isotropic solid which means that the material properties could be described in terms of only two parameters, c_{11} and c_{44} of the stiffness matrix. These parameters also give the value of another stiffness parameter c_{12}. These parameters are given in terms of velocities and density, ρ as:

$$
\begin{aligned}
c_{11} &= \rho v_l{}^2 \quad, \\
c_{44} &= \rho v_s{}^2 \quad, \\
c_{12} &= c_{11} - 2c_{44} \quad.
\end{aligned}
\tag{5.9}
$$

Thus the Young's modulus and the Poisson's ratio for the material used in equation (5.3) are obtained using the stiffness parameters as:

$$
\begin{aligned}
E &= c_{11} - \frac{2c_{12}{}^2}{c_{11} + c_{12}} \quad, \\
\nu &= \frac{c_{12}}{c_{11} + c_{12}} \quad.
\end{aligned}
\tag{5.10}
$$

This model gives a value of acoustic attenuation which depends linearly on frequency. This is just an approximation as the attenuation in tungsten epoxy composites varies with frequency in a way that may or may not be linear. But if the values of attenuation at different frequencies are known, it is also possible to define a loss model that has a different frequency dependence using either the loss factor model or the Rayleigh damping model.

5.4 Simulation for a wave propagating normal to the bottom surface

In this case, the reflection of the specular waves from the grooved bottom structure is calculated for normal incidence. For normal incidence, the value

for the incidence angle, θ, as defined in Figure 5.4 is set to zero. After the problem is solved in COMSOL, the displacements in x and y directions are obtained. It is also possible to obtain the values for velocities and stresses for longitudinal waves both in y and $-y$ directions. For a down propagating wave, there will be a specularly reflected wave and other reflected waves in directions given by k_x-vectors of multiples of $\pm\dfrac{2\pi}{W}$ in addition to the incoming k_x. At a cross section of the structure above the grooves, Fourier transform of the obtained velocities and stresses are computed as shown in Figure 5.5. This gives the amplitudes of waves in different k-directions. The amplitudes of longitudinal waves with $k_x = 0$ propagating in upward and downward direction are calculated from the following equations:

$$\begin{bmatrix} v_y \\ T_{yy} \end{bmatrix} = \begin{bmatrix} 1 & 1 \\ Z_l & -Z_l \end{bmatrix} \begin{bmatrix} A_l \\ B_l \end{bmatrix} \quad , \tag{5.11}$$

where A_l and B_l are the amplitudes of waves propagating respectively in downward and upward directions in the grooved structure, v_y is the zeroth order FFT of the particle velocity in the y direction, T_{yy} is the zeroth order FFT of the longitudinal stress in the y direction, and Z_l is the value of the longitudinal acoustic impedance. The ratio of the amplitudes $\left(\dfrac{B_l}{A_l}\right)$ gives the value of the reflection coefficient at a particular frequency.
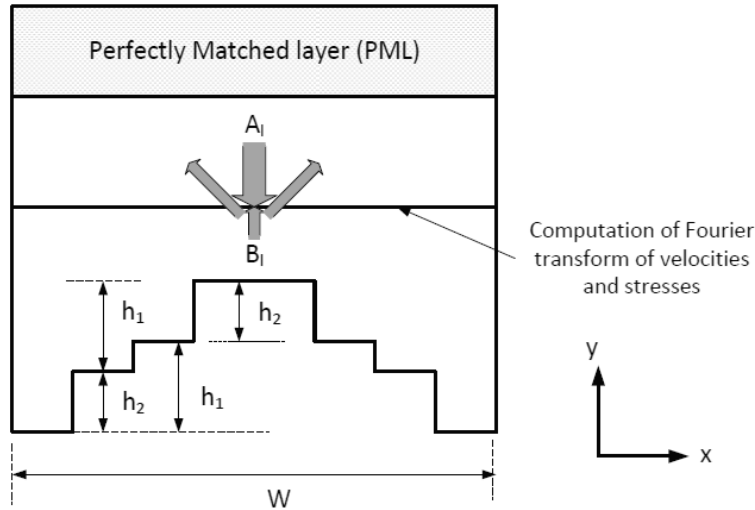
Figure 5.5: Calculation of specular reflection coefficient by taking the Fourier transform at a cross section of the structure.

Two different structures are studied here; one with a single groove and

another with two interwoven grooves. In the single grooved structure, this frequency is chosen to be 16 MHz and for the double grooved structure, these frequencies are chosen to be 16 MHz and 25 MHz. The results obtained from the simulation are shown in Figure 5.6 and 5.7 for the two cases respectively. For the double grooved structure, the results are shown for both symmetric and asymmetric designs. Neglecting effects of vertical surfaces and corners, both designs should provide the same response. They may also have different advantages/disadvantages during manufacturing.
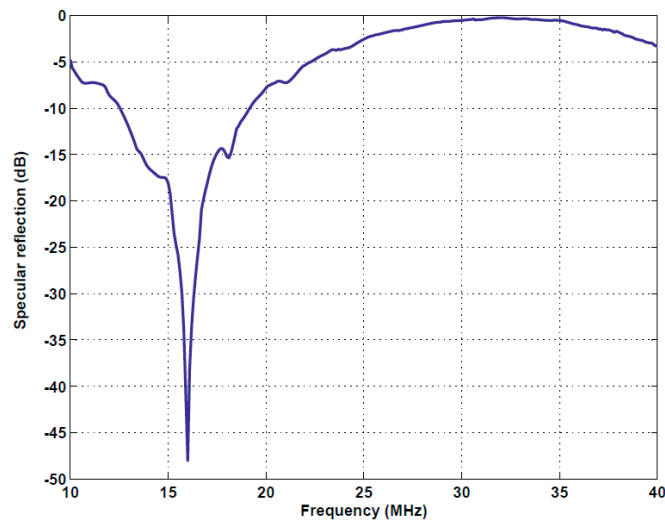
Figure 5.6: Reflection from a single grooved structure designed to give a null at 16 MHz.

As we see from the figures, the obtained results match well with the calculations done earlier using the simple delay difference method. In the single grooved structure, the null in specular coefficient is seen only at a particular frequency, which is 16 MHz in this case. In the case of doubled grooved structure, besides two nulls in the frequency range, the specular reflection is less than -15 dB in the range of frequencies from 12 MHz to 28 MHz. The specular reflection obtained for both symmetric and asymmetric designs are almost identical, except the exact value of specular reflection at the two chosen frequencies.

To estimate the attenuation that is only due to the grooved structure, absorption loss in the material is not taken into account. This means that the groove structure by itself is capable of providing 15 dB or more attenuation in the frequency range of 12 MHz to 28 MHz. In Section 5.3, we have discussed how absorption loss due to the tungsten epoxy composite could
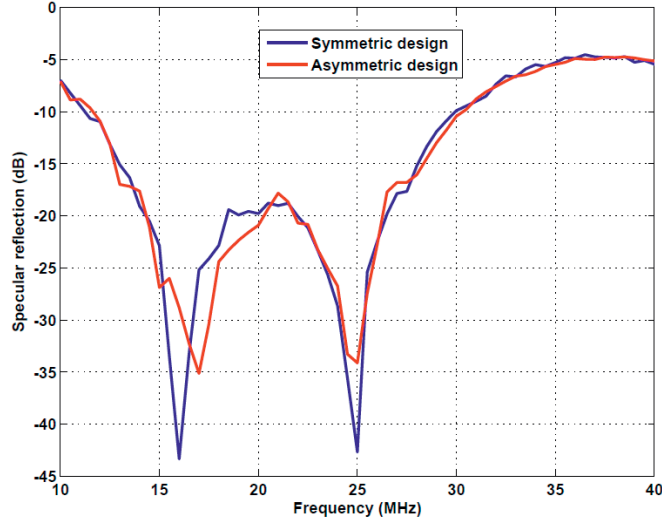
Figure 5.7: Reflection from double grooved structure designed to give nulls at 16 MHz and 25 MHz.

be included in the simulation. The result for the double grooved structure with the loss factor included is shown in Figure 5.8. The reflection is evaluated at a height of 150 μm above the lowest surface in the backing. Here the values of dilatational loss factor, η_d, and shear loss factor, η_s, are chosen as 0.08 and 0.8 respectively. The loss in shear direction is chosen higher than in longitudinal direction as the viscous loss is higher for shear waves compared to longitudinal waves. These values provide an attenuation of about 1 dB/mmMHz for the longitudinal waves. These values are chosen to demonstrate the effect of absorption loss and do not correspond to the measured absorption loss from tungsten epoxy composites. From our measurement results, which will be discussed in detail in Chapter 7, the attenuation obtained for epoxy tungsten composite with about 40% volume fraction of tungsten is about 30 dB/mm around 20 MHz. This loss however seems to vary less with frequency than assumed in this model. Thus the values for the loss factors are chosen such that they are close to the experimental results for most of the frequency range used in this work.

It can be seen that the addition of absorption loss and scattering loss do not exactly yield the total attenuation shown in Figure 5.8. This is because the absorption loss shown here is for a 150 μm thick epoxy tungsten composite without grooves, whereas the actual thickness changes due to the presence of the grooves at the bottom.

The inclusion of the loss factor in the model provides a more accurate
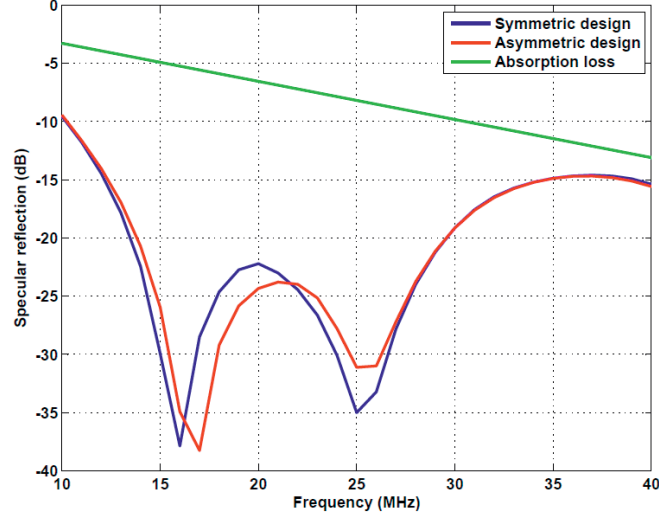
Figure 5.8: Reflection from double grooved structure including the absorption loss with loss factors $\eta_d = 0.08$ and $\eta_s = 0.8$ evaluated at a height of 150 μm above the lowest surface in the backing.

value of the attenuation for the grooved backing structure. It includes both attenuation due to scattering from the grooves and the absorption loss in the tungsten epoxy composite. The loss model used here depends linearly on frequency, that is why more loss is observed at higher frequencies than at lower frequencies. But the nulls in the specular reflection are still present at roughly the same frequencies.

5.5   Simulation for oblique incidence

Section 5.4 discusses waves at normal incidence. In this section the same process is repeated for different angles of incidence. For the calculation of reflected waves in different directions, a similar formulation is used as in the case of reflection of waves from a free boundary. For the longitudinal wave input in such a boundary, there will be a reflected longitudinal wave as well as a reflected shear wave as shown in Figure 5.9. But due to the presence of grooves at the bottom of the surface, the wave is also converted into longitudinal and shear waves with k-vectors in the transverse direction which are multiples of $\pm\dfrac{2\pi}{W}$ in addition to the incoming k_x, where W is the period of the structure in x direction. The calculation shown below is valid only for the waves that are specularly reflected from the bottom of the

surface for different incident angles.
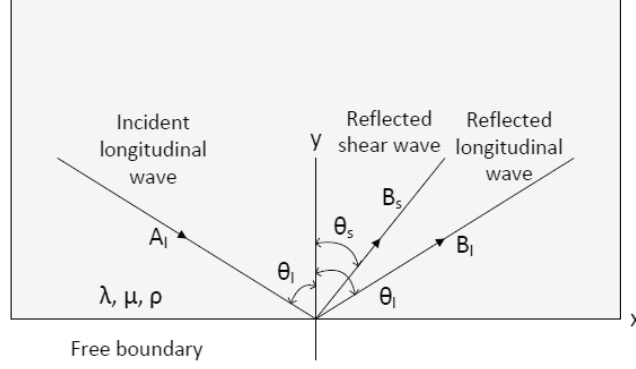
Figure 5.9: Reflection of longitudinal waves from a free boundary.

The plane strain formulation in the structural mechanics module of COMSOL solves the waves for displacements in x and y directions. From this solution, velocity and stress in both directions could easily be computed. The solid medium is the backing material whose material properties and density are known. If v_x and v_y are the particle velocities in x and y directions, the longitudinal stress, T_{yy} and the shear stress, T_{xy} are given by [Aul90] :

$$T_{yy} = \frac{c_{12}}{j\omega}\frac{\partial v_x}{\partial x} + \frac{c_{11}}{j\omega}\frac{\partial v_y}{\partial y} \quad . \tag{5.12}$$

$$T_{xy} = \frac{c_{44}}{j\omega}(\frac{\partial v_y}{\partial x} + \frac{\partial v_x}{\partial y}) \quad . \tag{5.13}$$

Using the equations (5.12) and (5.13), the velocities, v_x and v_y and the stresses, T_{xy} and T_{yy} in the medium may be represented in a matrix form as follows:

$$
\begin{bmatrix} v_y \\ v_x \\ T_{xy} \\ T_{yy} \end{bmatrix} = \begin{bmatrix} -\cos\theta_l & \cos\theta_l & -\sin\theta_s \\ \sin\theta_l & \sin\theta_l & \cos\theta_s \\ \frac{c_{44}\sin 2\theta_l}{v_l} & -\frac{c_{44}\sin 2\theta_l}{v_l} & -Z_s\cos 2\theta_s \\ -\frac{c_{11}\cos^2\theta_l + c_{12}\sin^2\theta_l}{v_l} & -\frac{c_{11}\cos^2\theta_l + c_{12}\sin^2\theta_l}{v_l} & -Z_s\sin 2\theta_s \end{bmatrix} \begin{bmatrix} A_l \\ B_l \\ B_s \end{bmatrix} .
\tag{5.14}
$$

Here θ_l is the incident angle, θ_s is the angle of the reflected shear wave, A_l is the amplitude of the incident longitudinal wave, B_l is the amplitude of

reflected longitudinal wave, B_s is the amplitude of the reflected shear wave, v_l is the velocity of the longitudinal wave, Z_s is shear acoustic impedance, and c_{11}, c_{12} and c_{44} are the stiffness parameters of the backing. The parameters c_{12} and c_{44} are also known as Lame's constant for an isotropic solid. The angle θ_s is given by $\sin^{-1}\left(\left(\dfrac{v_s}{v_l}\right)\sin\theta_l\right)$, where v_s is the velocity of shear waves in the material.

To solve the problem, oblique waves are applied with the help of k-vectors in x and y directions. After solving the problem in COMSOL, the displacements in the x and y directions are obtained for different frequencies. Also the corresponding stresses in x and y directions are computed. These parameters are computed for a cross section of the geometry as in the case of normal incidence, where the reflection coefficient is to be evaluated. The Fourier transform of particle velocities and stresses are obtained at this cross section. But before taking the Fourier transform, the spatial velocities and stresses are multiplied by a factor $e^{jk_x x}$. For the calculation of the reflection coefficient over a range of frequencies, equation (5.14) is solved and the ratio $\left(\dfrac{B_l}{A_l}\right)$ is obtained for each frequency. The parameters on the left hand side of the equation are all the zeroth order FFT of velocities and stresses obtained over a cross section of the structure above the grooves. These equations also give the result for waves propagating in normal direction when the value of the incident angle, θ_l, is set to zero.

The result obtained for different incidence angles are shown in Figure 5.10 and 5.11 respectively for asymmetric and symmetric designs for the frequency range, 10 MHz to 40 MHz. The material loss factors are the same as in the earlier case, 0.08 for the longitudinal waves and 0.8 for the shear waves. As seen from the figures, the specular reflection obtained for small incidence angles are very close to that for normal incidence. But as the angle of incidence becomes larger, the nulls in the specular reflection disappear. It can also be seen from the figures that the symmetric design performed slightly better compared to asymmetrical design. For both designs, for incidence angles smaller than $\pm 15°$, the specular reflection is not distinctly different from the results obtained for normal incidence. For larger incident angles, the deviation is more pronounced. Multiple reflections at different steps in the grooved structure could be one of the reasons for this. Also conversion of longitudinal waves into shear waves and waves in different transverse directions is more likely for larger input angles. A careful investigation of the results shows that there is an additional attenuation for all incident angles compared to the structure without grooves.
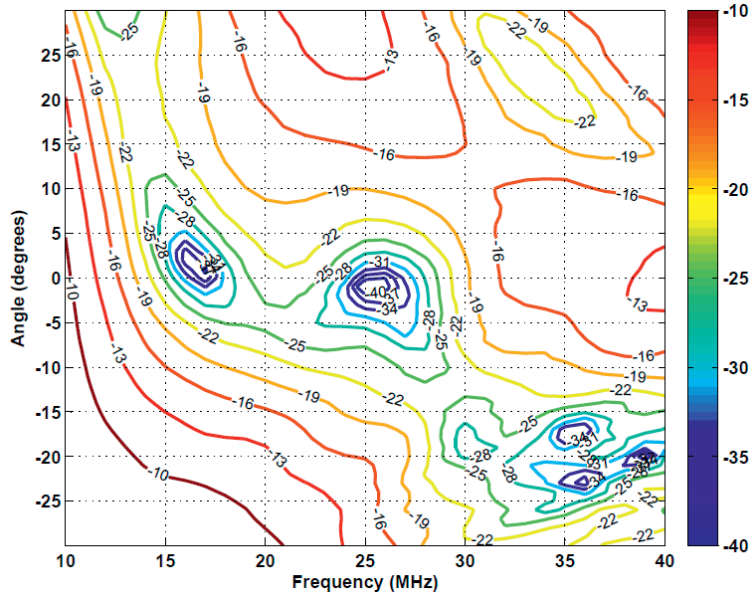
Figure 5.10: Specular reflection (dB) from double grooved structure for different incident angles with a period of 600 μm (asymmetric design).
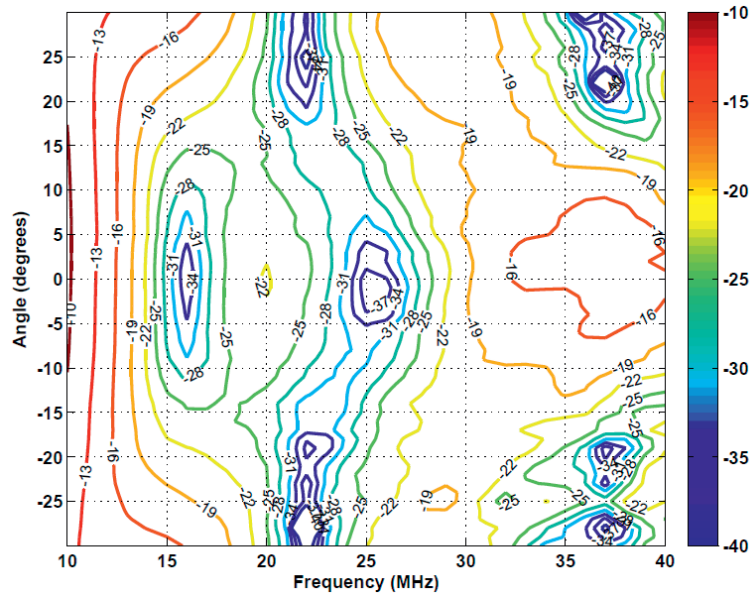
Figure 5.11: Specular reflection (dB) from double grooved structure for different incident angles with a period of 600 μm (symmetric design).

The simulations shown here are valid for infinite structures. It is clear that for the grooved backing structure to perform well, there should be a balance in cumulative total width of each step [CR09]. However, when CMUT transducers are to be used for intravascular applications, not only the thickness of the backing, but the lateral dimensions are also limited. The reflection properties of the grooves at the bottom of the backing help to reduce the thickness of the structure. But to take full advantage of the structure, the grooves should be designed such that lateral dimensions contain more than a few periods of the structure so that it behaves similar to an infinite structure. For example, if we assume that a lateral dimension of 1.5 mm is available for backing, we can accommodate 10 periods of a 150 μm structure compared to 2.5 periods of a 600 μm structure. This means that the period of the grooved structure should be reduced to get similar performance in practical applications. The performance of the grooved structure is studied for different periods smaller than 600 μm in the frequency range from 10 MHz to 40 MHz. For this frequency range the performance is essentially the same when the period is reduced down to 200 μm. The performance becomes somewhat different as the dimensions become smaller than 200 μm. The results obtained with a period of 150 μm for the frequency range are shown in Figure 5.12 and 5.13 respectively for symmetric and asymmetric designs. The performance of the grooved structure is still acceptable at 150 μm, but it is more random. For smaller periods, the asymmetric structure has a better performance. The performance of the symmetric design changed more rapidly compared to the asymmetric design when the period was reduced. This seems reasonable as the symmetric design divides the period into smaller parts compared to the asymmetric design.
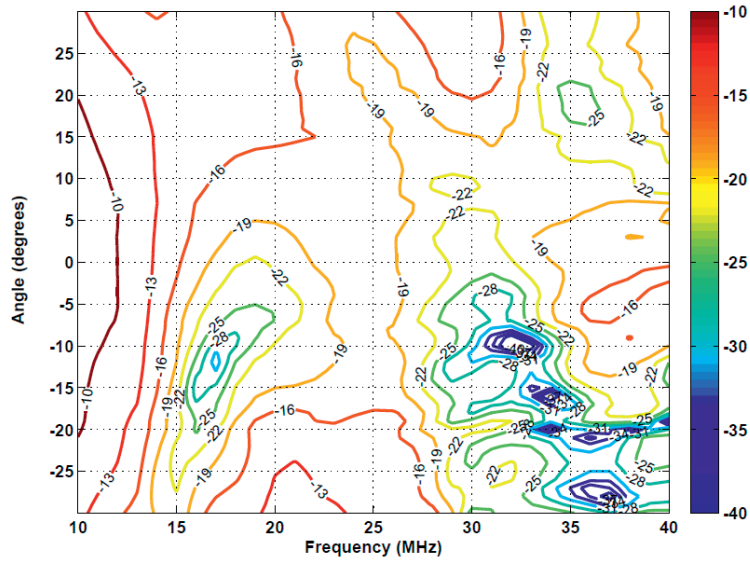
Figure 5.12: Specular reflection (dB) from double grooved structure for different incident angles with a period of 150 μm (asymmetric design).
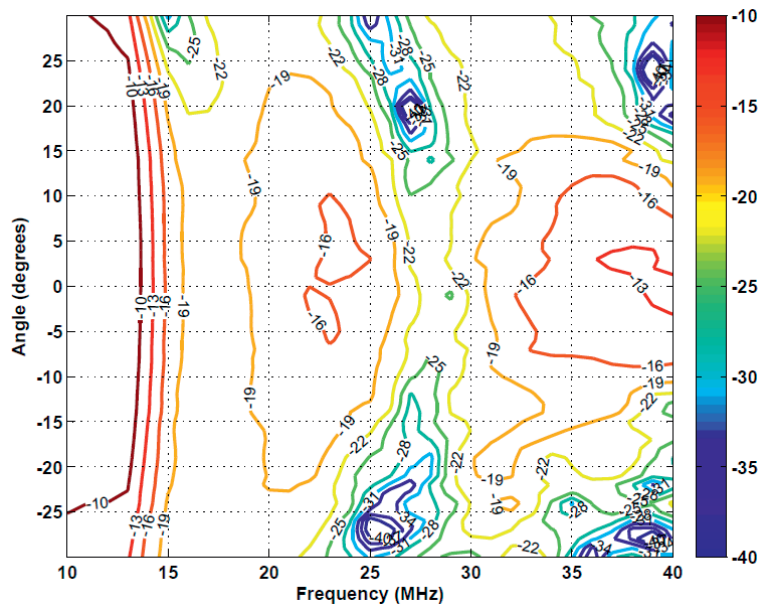
Figure 5.13: Specular reflection (dB) from double grooved structure for different incident angles with a period of 150 μm (symmetric design).

Chapter 6

Fabrication of Backing Structures

In this chapter we discuss how the grooved backing structure described in Chapter 4 and Chapter 5 can be prepared. We briefly discuss the different possible ways to make such structures and describe the details on how they are prepared in this work.

6.1 Fabrication methods

The dimensions of the grooves in the backing structure are in the range of tens of microns. Therefore we need to find a machining technique to achieve these dimensions. The backing structure used here is a composite material consisting of epoxy and tungsten powder. The mixture needs some time for curing. This curing time depends on temperature and pressure. After the mixture is cured, grooves could be created on its surface by machining techniques. As there are multiple steps of grooves in the structure, machining could be difficult in this case. Also these steps have to be repeated for each sample of the backing structure. Therefore a better way to create such a backing structure is to use a mold where it could be prepared by casting.

The mold required for the fabrication of the structure should be precise, in the order of a micron. There exists several methods for the preparation of such micro-molding components. One such technique is mechanical micro-machining, which is a scaled-down version of traditional material removal processes. This method is currently capable of fabricating miniature parts as small as tens of micrometers with very complex features and close tolerances using energy-efficient small machine tools [mec11]. But many factors need to be taken into account when shifting from macro-scale to micro-scale

such as material structure, vibration, thermal expansion, etc. Laser assisted machining (LAM) is another manufacturing process that has been referred to as an alternative to conventional machining of hard and/or difficult-to-process materials [OP07]. This involves preheating of a focused area with a laser beam over the surface of the workpiece to cause localized heating and thermal softening along the path of the cutting action. The main advantage of laser assisted machining over conventional machining is the increased material removal rate, productivity, and tool life. Electric discharge machining (EDM) is another non-conventional material removing technique. This process involves melting and evaporating material from the workpiece surface. This process uses electrical energy and turns it into thermal energy through a series of discrete electrical discharges occurring between the electrode and workpiece immersed in a dielectric fluid. A variety of EDM known as micro-EDM is capable of machining micro-holes and micro-shafts as small as 5 μm in diameter to complex three-dimensional (3D) micro-cavities [HN03]. But this method requires workpieces that are electrically conductive.

Another method for making 3D metallic or polymer micro-structures is using a lithographic process known as LIGA. The word LIGA is an acronym that stands for the main steps of the process: deep X-ray **Li**thography, electroplating (**G**alvo in German), and injection molding (**A**bformung in German) [Liu12]. It involves patterning of a thick layer of photoresist (for example polymethylmethacrylate) with high energy beams produced by a synchrotron radiation X-ray source. The photoresist is developed to form structures with deep vertical walls and high aspect ratios. Electroplating is conducted to fill the cavities with metal. After removing the photoresist, the metal piece can be used as a mold for batch fabrication of the parts. In some cases, UV rays are also used instead of high energetic X-rays. This method is then referred to as UV-LIGA.

6.2 Description of the method used: silicon micromachining

A widely used method for fabrication of 3D structures of micrometer scale is silicon micromachining. This method has been used for the fabrication of most of the MEMS devices. Different techniques used for micromachining of silicon are described briefly in Chapter 2. For the preparation of the grooved backing structure in our case, a grooved silicon wafer is used as a mold. As discussed earlier in Chapter 5, we are making a grooved structure that provides cancellation of specular reflections at two frequencies, 16 MHz and 25 MHz. This gives the different groove depths as 20 μm, 31.25 μm, and

51.25 μm with a longitudinal velocity of 2000 m/s. These depths could be achieved either by deep reactive ion etching (DRIE) or by wet anisotropic etching of silicon substrates. One of the following methods could be used to make the desired grooves on the silicon substrates:

1. Bosch RIE

   This is the most usual way to perform dry etching for creating deep structures. The method is capable of producing deep and high aspect ratio features with nearly vertical sidewalls. It is based on the patent by Robert Bosch GmbH and Texas Instruments Corporation. The process comprises a sequence of alternating process steps of silicon etching and protective polymer deposition, each of a few seconds duration in a high-density plasma [Liu12]. The cyclic nature of the etch process may leave an artifact known as *scallops* on the etched sidewalls as shown in Figure 6.1. Each scallop corresponds to one full etch and deposit cycle. There exist different ways to partly smooth them out, but it is difficult to entirely get rid of them. The net result of this process are walls that essentially form 90° with the top surface, apart from the scallops. But they do have a tendency to create a slightly smaller angle as we etch further downwards, i.e. the opening could become larger the deeper we go.
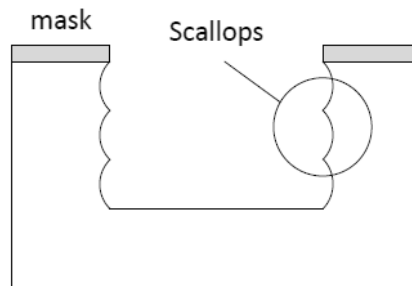
Figure 6.1: Deep reactive ion etching of silicon.

2. Continuous RIE

   The continuous RIE process avoids the scallops. But this method is not used for depths of 20 μm and more, and is typically used only up to 1 μm depth, for extreme depth accuracy.

3. Isotropic RIE

   Isotropic RIE is another variety of RIE. In isotropic etching, the etch rate is the same in both horizontal and vertical directions. This

method will give groove walls that are not exactly 90°. As the grooved structure for our case has different steps, there will be difficulties on how to put the three levels together, especially due to the underetch problems.

4. Anisotropic wet etching

   Anisotropic wet etching has been used for more than two decades for etching of silicon. This process can be used to create recessed structures (for example cavities with or without membranes), protruding structures, and suspended mechanical structures [Liu12]. The process has been used for the manufacturing of commercial products like pressure sensors and accelerometers. Wet anisotropic etching of silicon is usually carried out by silicon etchants like EDP (ethylene diamine pyrocatechol), KOH (potassium hydroxide) or TMAH (tetra methyl ammonium hydroxide). Although DRIE and other processes offers high aspect ratio and vertical walls, silicon anisotropic wet etching is very popular as it offers unique 3D profiles and smooth walls at relatively lower cost. This method creates smooth walls at a 54.7° angle for <100> oriented silicon wafers as the etch rate on <111> direction is very small compared to the etch rate on <100> direction. But underetch may cause a problem as there are three different depths in the design.

Among the different options stated above, we have chosen wet anisotropic etching of silicon by TMAH to create the mold for the backing structure. We have considered <100> oriented silicon substrate with edges of the mask aligned in <110> direction. This method creates smooth walls at an angle of 54.7° but with a small undercut, u, as shown in Figure 6.2. The design of structures for improved backing of CMUTs consists of different steps that have vertical walls. For the bulk wave propagation, the performance would not be different even if the angles are different than 90°. Simulations have been performed for structures with this 54.7° angle which resulted in a similar performance as the structures with vertical walls. As the requirement of angle is not very strict, the wet anisotropic etching of silicon is chosen from the different options discussed earlier. This method is a cost effective method and easier to implement compared to the other options. The fact that the angle wall makes with the top surface is only 54.7°, makes it easy to remove the epoxy tungsten composite from the mold after curing. Because this method creates a smooth wall at 54.7°, the width of the different layers would be somewhat different from what we have shown in the earlier drawings.
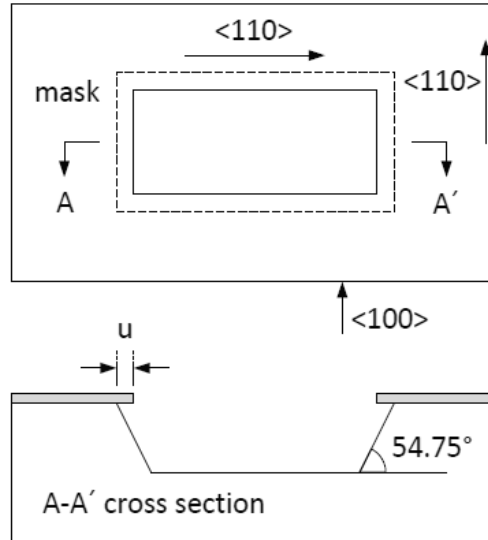
Figure 6.2: Wet anisotropic etching of silicon.

A schematic of the grooved structure obtained by wet anisotropic etching of silicon is shown in Figure 6.3. As shown in the figure, the widths of different levels would be changed according to the wet etching angle. The figure shown here is for the asymmetric design, but the change would be similar in the case of the symmetric design. The requirements for the groove depths for different levels are still the same. This means that the cumulative widths of the four different height levels should be equal, the total period width remaining the same. For the asymmetric design shown in Figure 6.3, this gives:

$$W_1 = W_2 = W_3 = W_4 \quad . \tag{6.1}$$

As the period of the structure is 600 μm, the widths at each step will now be less than 150 μm due to this wet etching angle. The exact value of the widths in the masks depends on how we start the wet etching process. For example, if we start the etching process by etching the shallowest and the widest step first, the widths of each layers would be 132 μm (approx). It is a rough estimate; the exact value depends on different practical considerations. In a practical case, there will be an undercut in the silicon wafer and the exact values of widths may differ slightly from what have been designed. The simulation shows that the result would not vary much if the change is within 5% to 10% in width of each layer. But the smaller the variation is,

the closer the result is with the simulation.
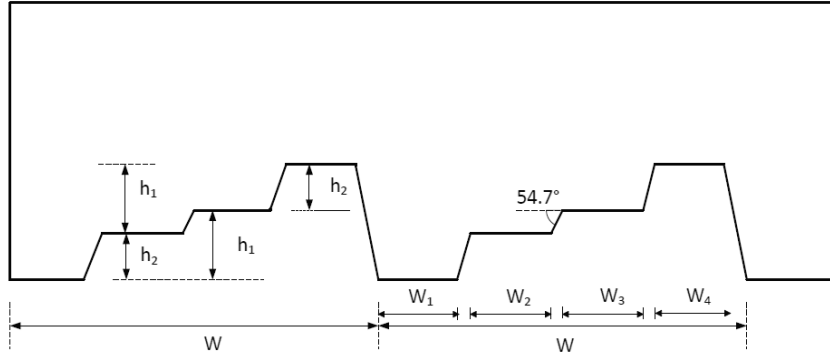
Figure 6.3: Asymmetric structure with grooves obtained by anisotropic wet etching of silicon (figure is not to scale).

6.3   Fabrication of the grooved structure

As explained in the previous section, wet anisotropic etching of silicon by TMAH is performed to create grooves on a silicon wafer. The etching process and the other processes were performed at SINTEF MiNaLab facility in Oslo. The structure is designed to give nulls in specular reflection at two frequencies. This requires four different levels in the structure. Thus three masks are needed to create the grooves in the structure. We have used both symmetric and asymmetric designs. Neglecting the effects of vertical surfaces and corners, both designs should provide the same response. But they may have different advantages/disadvantages during the manufacturing process. The masks layout for the structure is shown in Figure 6.4, where the upper half of the silicon wafer is used for the asymmetric design and the lower half is used for the symmetric design. We have designed the masks to start the wet etching process from the widest and the shallowest step first. The three different masks are shown as three different colors in the figure.

The etched silicon wafers were examined after each etching step to confirm the dimensions before proceeding to the next etching steps. The structures prepared by anisotropic wet etching of silicon wafers were very close to the design parameters used in the simulations. There were little variations around the edges and the variation of the step heights were within the tolerance limit of ± 5 to $\pm 10\%$. After the grooved structures were fab-
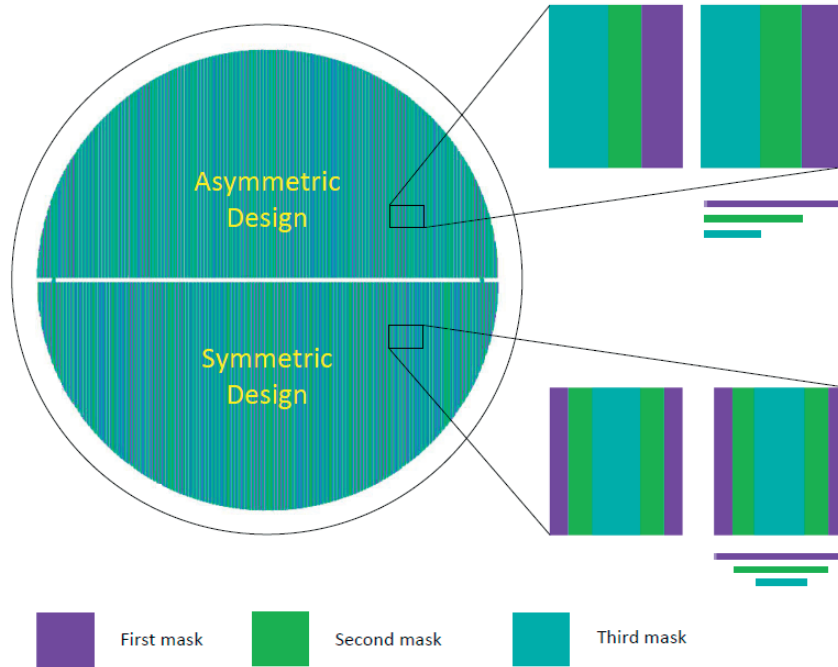
Figure 6.4: Mask layout for symmetric and asymmetric design.

ricated, a thin layer of polymer was deposited on their surface so that it could be easier to demold the epoxy tungsten mixture from the structure after curing. Instead a release agent could also be used before epoxy tungsten mixture is molded using this structure. The SEM images of silicon wafers after each etching steps are shown in Figure 6.5 to 6.7 for both symmetric and asymmetric designs. The first mask is essentially the same for both symmetric and asymmetric designs as we have started with the widest and the shallowest width first.

FEM simulations are performed on the structures that have the exact geometry as the silicon wafers obtained from the wet etching processes. As the grooves are made by wet anisotropic etching of the silicon wafer, the groove walls are not vertical in this case. The simulations are performed for walls at 54.74°, both for the symmetric and the asymmetric designs. The geometry used for simulation would be exactly as in Figure 6.3, but with only one period of the structure. Periodic boundary conditions are applied in the horizontal direction to make the structure infinite. The longitudinal and the shear loss factors are chosen as 0.08 and 0.8 respectively. The values chosen for absorption loss in the composite are the same as in the earlier case

(a) Symmetric design   (b) Asymmetric design
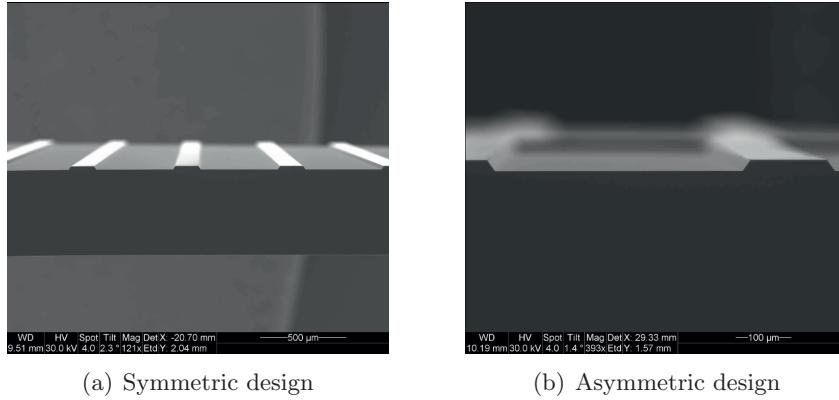
Figure 6.5: SEM images of etched silicon wafer after first mask.

(a) Symmetric design   (b) Asymmetric design
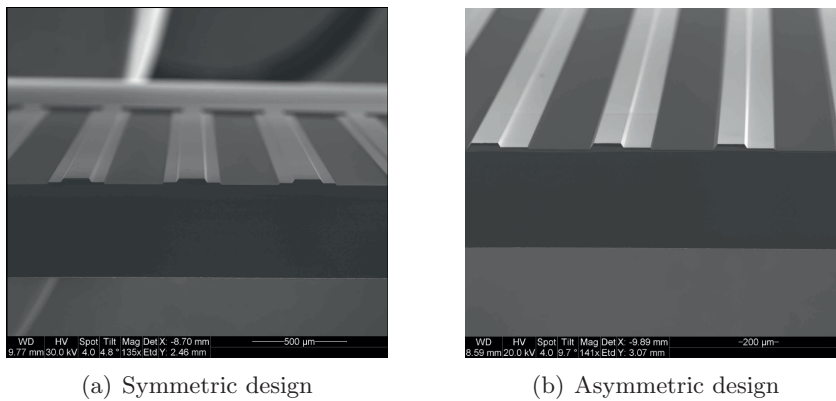
Figure 6.6: SEM images of etched silicon wafer after second mask.

to make a comparison with the performance of the grooved structures with the vertical walls. The obtained results for the specular reflection for different incident angles from such a grooved structure are shown in Figure 6.8 and 6.9 for asymmetric and symmetric designs respectively. Comparing the results obtained with vertical walls of the grooves, we confirm that the angles due to wet etching do not change the reflection pattern significantly. The frequencies where the nulls are observed in the reflection coefficient are roughly at the same frequencies 16 MHz and 25 MHz, but the exact value of specular reflection at those frequencies are slightly different in this case. The symmetric and the asymmetric designs have similar responses for the normal incidence case. The asymmetric design gives a result that is not symmetric with respect to the incident angle. For both designs, for

(a) Symmetric design   (b) Asymmetric design
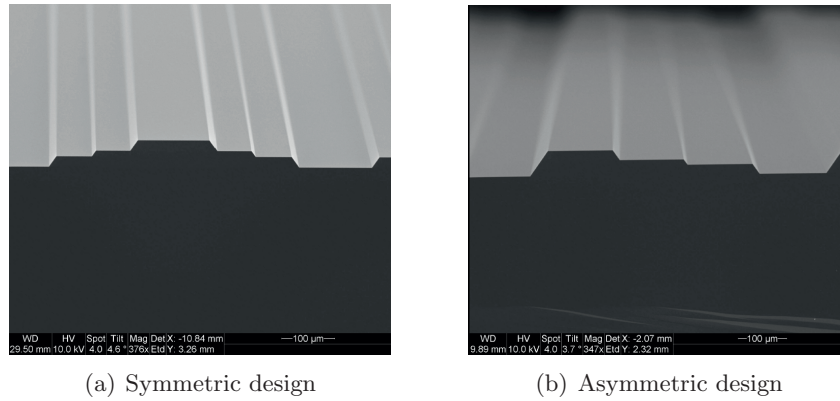
Figure 6.7: SEM images of etched silicon wafer after the third and final mask.
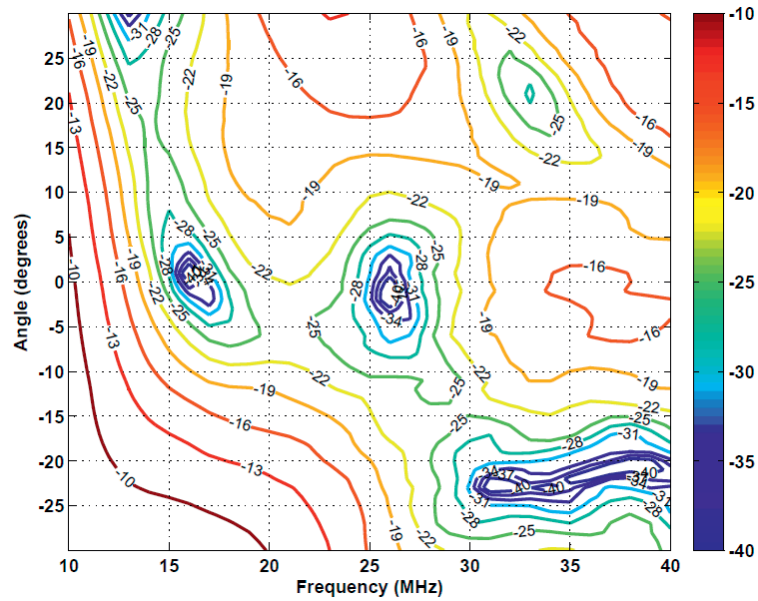
Figure 6.8: Specular reflection (dB) from a grooved structure for different incident angles with a geometry exactly as in the practical case with a period of 600 μm (asymmetric design).

incidence angles smaller than $\pm15°$, the specular reflection is not distinctly different from the results obtained for normal incidence. For larger incident angles, the deviation is more pronounced. Although there are small deviations, the overall attenuation obtained from the grooved structure over the frequency range is still the same as obtained with the structures that have
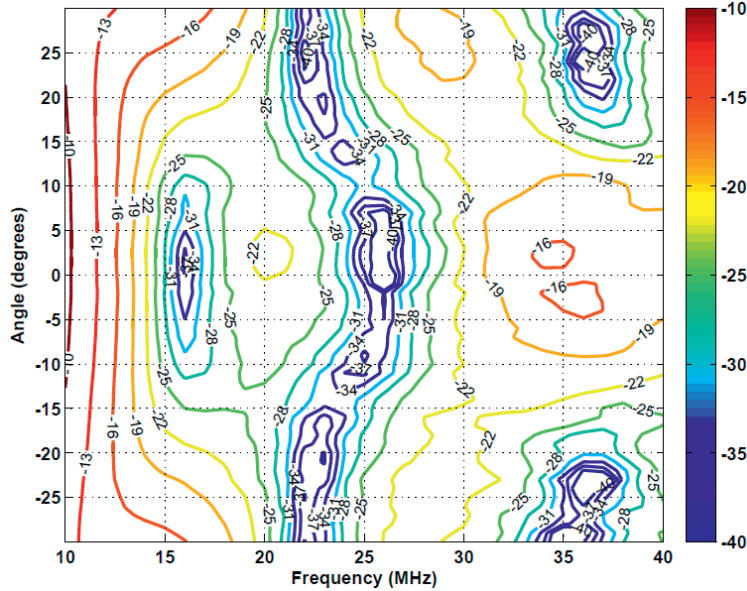
Figure 6.9: Specular reflection (dB) from a grooved structure for different incident angles with a geometry exactly as in the practical case with a period of 600 μm (symmetric design).

vertical walls.

In this work, the period of the structure is chosen to be 600 μm. But in practical applications where the space is limited, the period of the structure should be reduced so that we could include a few periods of the structure for a given width of the acoustic backing. In such a case, it behaves similar to an infinite structure. The performance is essentially the same when the period of the structure is reduced down to 200 μm. The specular reflection obtained for the structures with a period of 200 μm are shown in Figure 6.10 and 6.11 respectively for symmetric and asymmetric designs. The results are similar to what has been obtained using grooves with the vertical walls discussed in Chapter 5. This makes the grooved backing structure prepared with wet anisotropic etching of silicon useful in practical applications, where there is limited space available under the transducer.
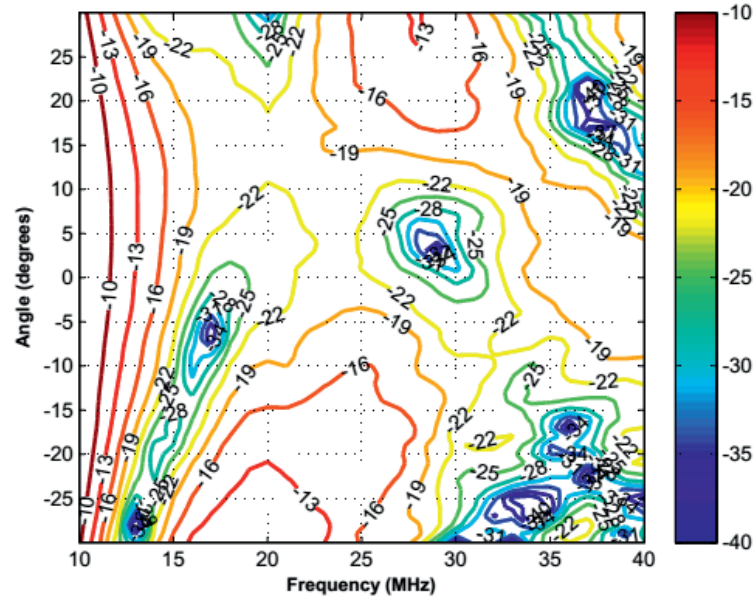
Figure 6.10: Specular reflection (dB) from a grooved structure for different incident angles with a geometry exactly as in the practical case with a period of 200 μm (asymmetric design).
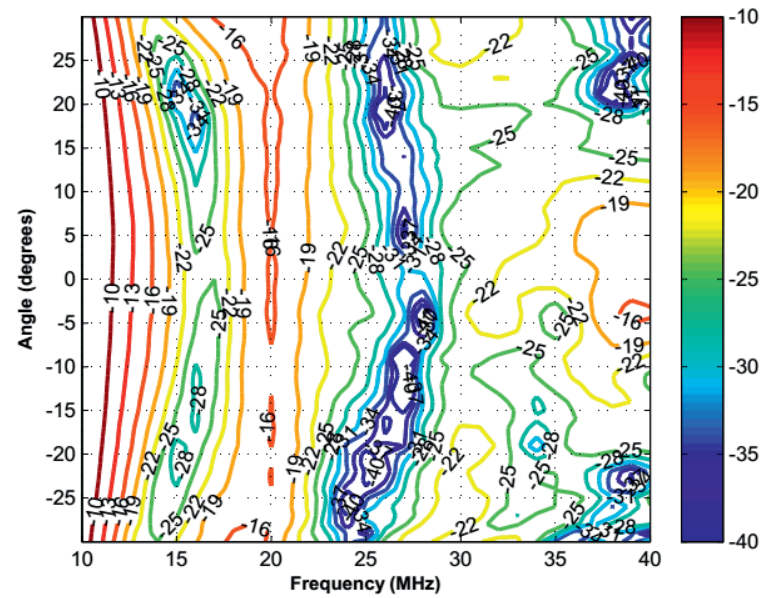
Figure 6.11: Specular reflection (dB) from a grooved structure for different incident angles with a geometry exactly as in the practical case with a period of 200 μm (symmetric design).

Chapter 7

Experimental Results

We have performed simulations on the grooved backing structure using COMSOL Multiphysics and Matlab as described in Chapter 5, and fabricated the structures as described in Chapter 6 . In this chapter, we present some experimental results obtained by using such grooved structures. We compare the FEM simulation results with the experimental results for validation of our work. In the first section of the chapter, we describe the experimental procedure and present the results obtained from the experiments. In the latter section, results obtained by measurement of shear wave properties of some polymer materials are presented. These lossy polymers can be used as a top layer for the CMUT transducer to reduce the acoustic cross coupling between the transducer elements. They can also be used as lens material for CMUT transducers.

7.1   Validation of FEM simulation

7.1.1   Details of experimental procedure

Experiments were performed for the measurement of attenuation due to grooved backing structures. Backing material chosen for this work is a composite of epoxy and tungsten powder as discussed in Chapter 3. To estimate the attenuation due to grooves, reflection measurement was performed using Rhode and Schwarz vector network analyzer (10Hz/9kHz-4GHz). An immersion type ultrasonic transducer from Olympus (Panametrics - NTD V300 series) with center frequency 20 MHz was used as a transceiver for the experiment. The frequency was swept from 10 MHz to 30 MHz in the network analyzer in order to include the two frequencies, 16 MHz and 25 MHz, where nulls are desired in the specular reflection. The transducer

used is a single element longitudinal wave transducer with a quarter wavelength layer that is acoustically matched to water. The power setting in the network analyzer was chosen in such a way that the average power dissipation to the transducer did not exceed 125 mW (21 dBm). This should be maintained in order to avoid overheating of the transducer and depoling of the crystal [Oly06]. The scattering parameter S_{11}/S_{22}, can be measured over the frequency range to measure the specular reflection coefficient. In this work we measured the parameter S_{22} to get the reflection coefficient. Averaging was enabled in the network analyzer to improve the accuracy of the results. Averaging was enabled both during the calibration process and during the measurement process. The obtained results were post-processed and analyzed using Matlab.

A schematic of the experimental setup is shown in Figure 7.1. One side of the backing material was kept in water while the other side was kept free. By keeping the bottom side free, the waves that are incident on the bottom side of the backing material would reflect back to the same medium with negligible reflection loss at the backing-air interface. This is because the acoustic impedance of the backing material is much higher than the acoustic impedance of air.
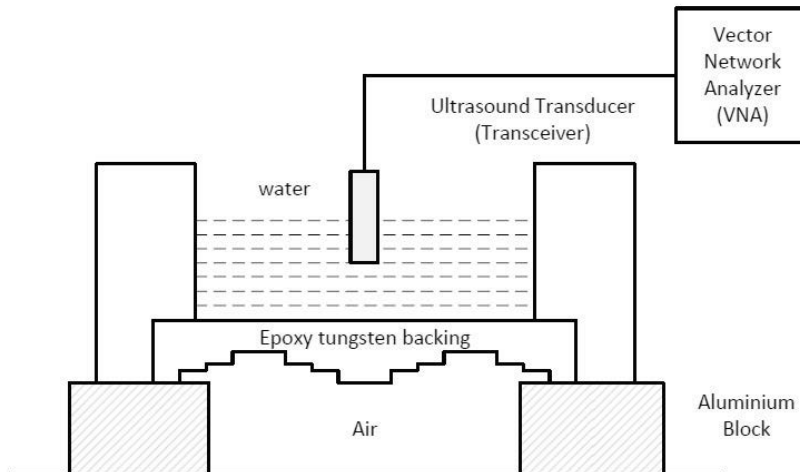
Figure 7.1: Experimental setup for the measurement of attenuation due to the presence of grooves at the bottom of the backing.

Experiments were performed for waves propagating normal to the bottom of the backing structure. The experimental setup was placed in a me-

chanical support where small adjustments in angle could be made in order to align the backing material correctly with the transducer. To estimate the attenuation due to the grooves at the bottom of the epoxy tungsten backing, a similar experiment was performed for the backing material without grooves present at its bottom. Both of them were prepared with the same volume fraction of tungsten powders. The difference between these two cases provide an estimate of attenuation due to the presence of the grooves. The obtained results from the experiment were compared with the simulation results. Although the groove depths were optimized for the epoxy-tungsten composite, the structures were also tested for wave propagation in the cases of water and epoxy (without tungsten). The parameters in the simulation were then adjusted to get an estimated response for these cases. The description of the different experiments and the results obtained from them are described in the following sections.

7.1.2 Performance of the grooved structure

Wave propagation in water

In this case, the reflection coefficient from a grooved silicon wafer in water was measured. Acoustic waves were irradiated on the grooved side of the wafer and the other side of the wafer was in air. The silicon wafers used in the measurements were 500 μm thick. To estimate the attenuation due to the grooves, the experiment was repeated with a silicon wafer of the same thickness but without any grooves at the bottom. The results obtained for both cases are shown in Figure 7.2. The theoretical estimate of the reflection attenuation in water, taking the velocity of sound in water as 1500 m/s, is also shown in Figure 7.3. In fact, the difference between the two curves in the Figure 7.2 should give the actual value of attenuation due to grooves.

It can be seen from the figure that there is significant reflection attenuation due to the presence of the grooves at about 19 MHz which matches fairly well with the theoretical calculations. We would also expect another dip at 12 MHz based on theoretical calculations, but this is dominated by noise in our result. In the results, dips could be seen in the curve for silicon wafer without grooves at 16 MHz and 24 MHz. They are due to thickness resonances in the silicon wafers. This occurs when the wafer thickness becomes equal to a multiple of the half of the acoustic wavelength in silicon. The frequencies where these thickness resonances occur are given by the following equation:

$$f = n \left(\frac{v}{2t} \right) \quad , \tag{7.1}$$
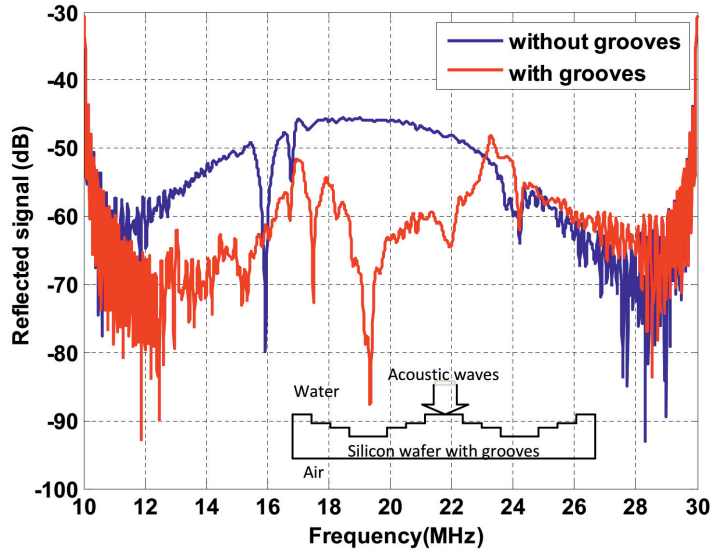
Figure 7.2: Reflected signal from silicon wafer in water with and without grooves.
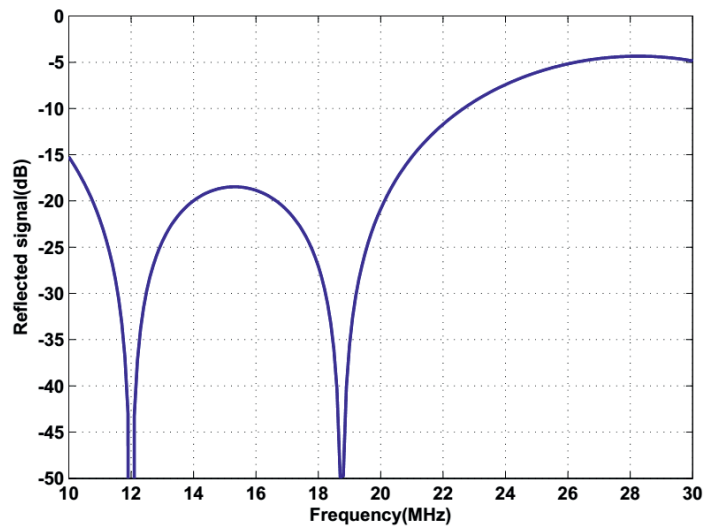
Figure 7.3: Calculated added reflection attenuation due to the grooves for silicon wafers in water. The nulls are at different frequencies than 16 MHz and 25 MHz as the wave propagation is considered here in water instead of epoxy tungsten composite.

where v is the longitudinal wave velocity in the silicon wafer, t is the thick-

ness of the silicon wafer, and n is an integer. As the longitudinal velocity in silicon is about 8000 m/s and the thickness of silicon wafer used in the experiment is 500 μm, the frequencies where the resonances are supposed to occur are integer multiples of 8 MHz. The dips in the response at 16 MHz and 24 MHz fit well with this. As it could be seen from the figure, the presence of grooves contributed an additional attenuation of 10-15 dB for the reflected wave in the frequency range 12 MHz to 22 MHz. This matches fairly well with the theoretical calculations as shown in Figure 7.3. In addition to this attenuation, the presence of grooves at the bottom of the wafer reduced the dips in the response that are due to the thickness resonances in the silicon.

Wave propagation in epoxy

To measure the reflection coefficient for wave propagation in epoxy, the experiments were repeated with thin epoxy layers on silicon wafers. The epoxy used in the experiment was EPO-TEK 301-2 from *Epoxy Technologies*. The wafers with epoxy were kept in water with acoustic waves irradiated on the epoxy side. The other side was kept free so that the signal that would reach the bottom of the wafer would totally reflect back with a small transmission loss at the interface. The experiment was also repeated with epoxy on the silicon wafer without grooves. The thickness of epoxy was kept at 1mm ($\pm$0.1mm) for both cases. The obtained results for both cases are shown in Figure 7.4. The theoretical estimate of the added attenuation due to the back side grooves in the epoxy is shown in Figure 7.5. For the theoretical calculation of reflection attenuation in epoxy, the longitudinal velocity in epoxy is taken to be 2650 m/s. In the measurement results, we can see significant reflection attenuation near 21 MHz which matches fairly well with the theoretical estimate. The signal to noise ratio (SNR) is poor in this case because the losses in the epoxy are very high. Also, there are significant transmission losses at the two interfaces, the water-epoxy interface and the epoxy-silicon interface. From the experiment, the loss in epoxy is estimated to be about 9-12 dB/mm around 20 MHz, which is in accordance with [GGR90]. The thickness resonances in silicon were still present in this case because the silicon wafers were not removed from the epoxy. The presence of grooves at the bottom of the epoxy provided an added attenuation of 10-15 dB in the frequency range 16 MHz-23 MHz. We see that the irregularities at 16 MHz and 24 MHz caused by the thickness resonances were reduced due to the presence of the grooves, see Figure 7.4.
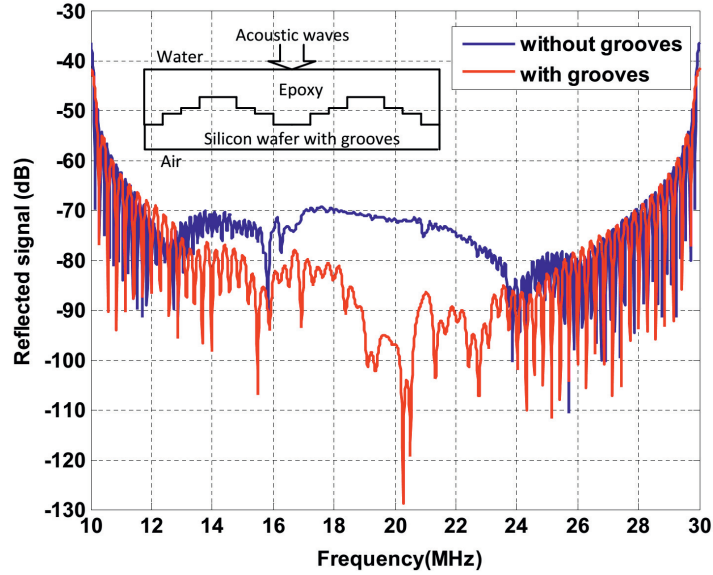
Figure 7.4: Reflected signal from the bottom side of the epoxy with and without grooves.
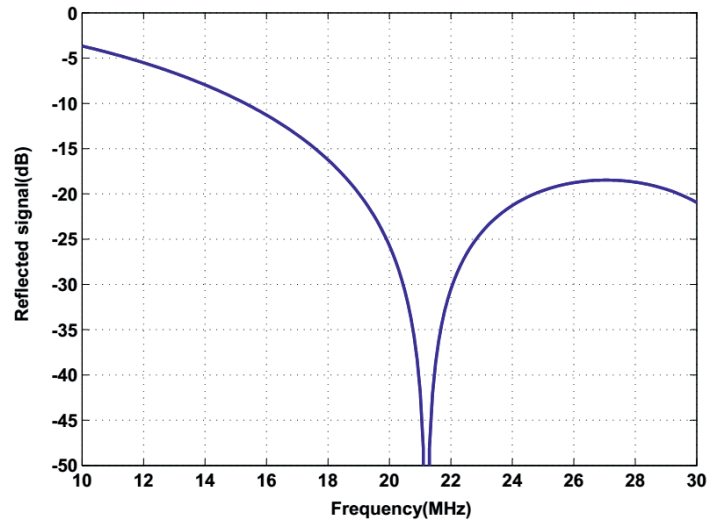
Figure 7.5: Calculated added reflection attenuation due to back side grooves for epoxy. Only one null is present here as the longitudinal velocity in epoxy, about 2650 m/s, is higher than the velocity in the epoxy tungsten composite.

Wave propagation in epoxy tungsten composite

We have discussed in an earlier section that the dimensions of the grooved backing structure were optimized for epoxy tungsten composite. The exper-

iments were performed with composites of epoxy and tungsten in this case. A schematic of the experimental setup for this case is shown in Figure 7.1. The epoxy used here is the same two part epoxy, EPO-TEK 301-2, used in the earlier experiments. The epoxy and hardener were mixed in a container. The tungsten powder, which is a mixture of 1-5 μm particle size (67%) and less than 1 μm particle size (33%), was hand mixed with epoxy at about 40% volume fraction to get a homogenous mixture. The mixture was degassed in a vacuum chamber at less than 10^{-3}millibar pressure to remove air bubbles introduced during the mixing process. The mixture was then cast between two silicon wafers spaced 200 μm apart. Two samples of equal thickness were prepared, one with grooves and one without grooves. They were both cured at room temperature for about 24hours. As explained in Chapter 6, the silicon wafers were covered with a thin layer of polymer which acts as a mold release agent and the cured tungsten and epoxy mixture could be removed easily.

After mold release, similar measurements were made as with epoxy. The acoustic impedance of the composite was estimated to be about 14 MRayl. This was found by multiplying the longitudinal velocity with the density of the composite. The longitudinal velocity was estimated to be about 1900 m/s by the measuring the time taken by the acoustic signal to travel through the sample of known thickness, and the density was estimated to be about 7300 kg/m^3 by measuring the mass and the volume of the sample. Based on our theoretical calculations, the value estimated for the acoustic impedance implies that the volume fraction of tungsten in the composite is close to 40%. But the measured values for the velocity and the density are 10-15% different from the theoretical estimates. The difference could be due to the errors in the measurement of the velocity and the density of the composite. Also there could be some errors in the results obtained from the Devaney model as discussed earlier in Chapter 3. Even though the percentage of tungsten in the composite was high, it was found to be non-conducting from electrical measurements. For electrical characterization, the capacitance was measured for a parallel plate capacitor with epoxy-tungsten composite as the dielectric with dimensions 20x5x1mm^3. The relative permittivity was found to be 22.5 from the experiment.

As the losses in the epoxy tungsten composite were very high, a thin layer of 200 μm was used to estimate the attenuation due to the grooves. As the structure was thin, the echoes of transmitted signal obtained from the front and back surface of the specimen were superimposed in the time domain response. Therefore, it was difficult to separate them. To obtain the shape and level of the reflected signal from the bottom surface, we

made a similar reflection measurement from a single reflecting surface to
get a reference signal. In this case, a thicker plate was used in order to
separate the reflections from the front and the back surface. This signal
matched in amplitude and phase with the first part of the echo, was then
subtracted from the time domain response obtained with the epoxy and
tungsten composites. In this way, we obtained an estimate of the echo
from the back surface of epoxy and tungsten composite. This process is
illustrated in Figure 7.6. This was done for all composite structures, without
grooves and with grooves, and for both symmetric and asymmetric designs.
These calculations assume that the epoxy tungsten mixture behaves like a
homogeneous medium with constant material properties in the frequency
range of interest.
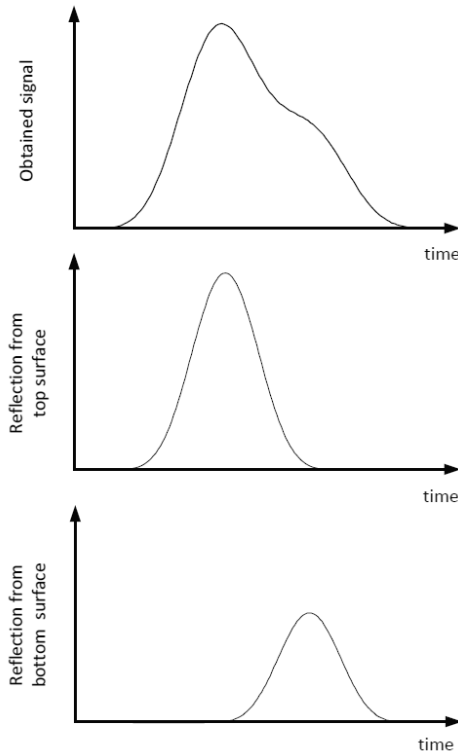
Figure 7.6: Estimation of reflected signal from back side of the epoxy tungsten composite.

The experimental results along with a theoretical estimate of the attenuation are shown respectively in Figure 7.7 and 7.8. To show the attenuation that is solely due to scattering from the grooves in the theoretical estimate,

absorption loss in the epoxy tungsten composite is not included. For the asymmetric design, it can be seen that there is significant additional reflection attenuation due to the grooves, about 25 dB, around 15 MHz, and about 10 dB or more in the frequency range of 14 MHz to 22 MHz. In the case of symmetric design, there is 10 dB or more attenuation in the frequency range 13 MHz to 28 MHz, with a small increase in the added attenuation, to about 16 dB around 24 MHz.
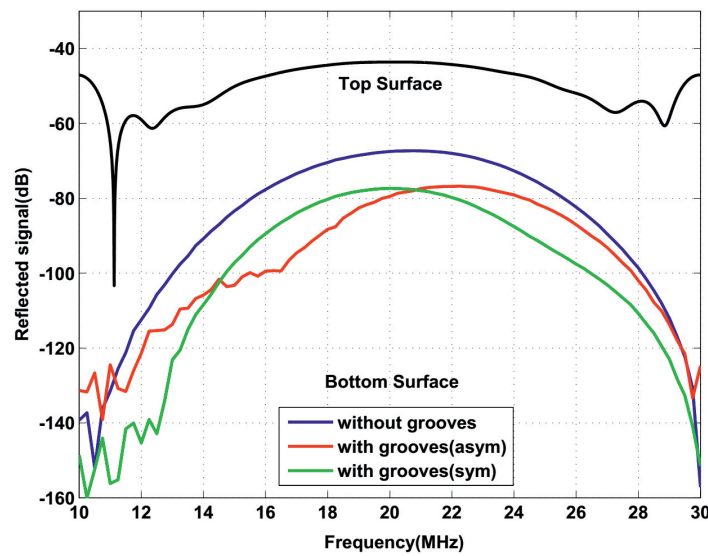
Figure 7.7: Experimental results with epoxy-tungsten composite showing reflected signal from front and back surfaces.

In Figure 7.7, the reflected signal from the top surface of the epoxy tungsten composite is also shown. As the reflected signals from top and bottom surface of the composite are known, absorption loss from the composite can easily be estimated. This is obtained by taking the difference between the measured reflected signal from the top and the bottom surface, and subtracting two times the transmission loss through the water-composite interface, which is 4.56 dB for this case. The transmission loss is calculated by taking the acoustic impedance of water and the epoxy tungsten mixture as 1.5 MRayl and 14 MRayl respectively. But this should be corrected with the reflection loss at the top surface of the composite. The different reflected and transmitted signals for our case are shown in Figure 7.9. Using
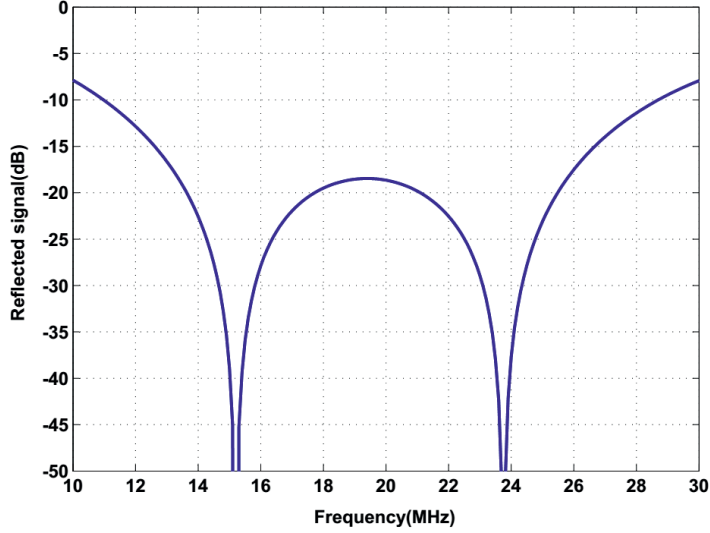
Figure 7.8: Calculated added reflection attenuation due to back side grooves for the epoxy tungsten composite. The nulls are at slightly different positions here since we have used the data obtained from our measurements for the velocity in the epoxy tungsten composite. The velocity used is 1900 m/s which is different from 2000 m/s used in the earlier calculations.

the notations of the figure, absorption loss (L) is calculated by:

$$
\begin{aligned}
L &= A - 2 \times T - C \quad , \\
  &= (B + R) - 2 \times T - C \quad ,
\end{aligned}
\tag{7.2}
$$

where A is the input signal from the transducer, B and C are respectively the reflected signal from the top and the bottom surface of the epoxy tungsten composite, and R and T are the reflection power loss and the transmission power loss at the interface between water and epoxy tungsten composite respectively. The reflection power loss and the transmission power loss at the interface between two media with acoustic impedances Z_1 and Z_2 are calculated by:

$$
\begin{aligned}
R &= \left(\frac{Z_2 - Z_1}{Z_2 + Z_1} \right)^2 \quad , \\
T &= \frac{4Z_1 Z_2}{(Z_1 + Z_2)^2} \quad .
\end{aligned}
\tag{7.3}
$$

This gives a two way loss in the 200 μm thick epoxy-tungsten composite to be 12-16 dB around 20 MHz. This is equivalent to 30-40 dB/mm around 20 MHz. As the 6 dB bandwidth of the transducer is about 48%, the result outside the frequency range 13-25 MHz is somewhat uncertain as it is dominated by noise in our measurements.
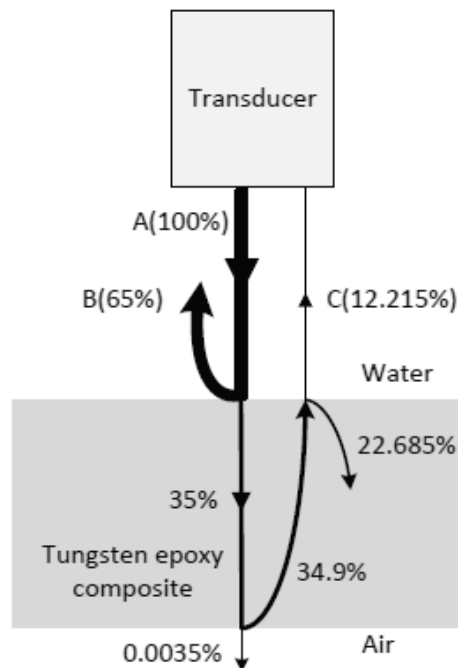
Figure 7.9: Reflection and transmission loss at different interfaces of epoxy tungsten composite.

The experimental results matched fairly well with the simulation and the theoretical calculations. With about 40% volume fraction of tungsten in epoxy, we are able to get an additional attenuation of 10-20 dB in the frequency range of interest for both designs, with a maximum of about 25 dB at around 15 MHz for the asymmetric design. For the other cases where high attenuation is expected, only a modest increase at around 24 MHz for the symmetric case is observed. At 15 MHz in the symmetric case and 24 MHz in asymmetric case, no local increase in attenuation is observed. One possible explanation for this could be that the top and bottom surfaces of the grooved structure were not exactly parallel. In fact, there was small variations, 10-20 μm, in the thickness when measured at the different points of the sample. Also non-homogeneity of tungsten powder in the epoxy-tungsten mixture

along the sample dimension could have caused some anomalies as it might lead to velocity variations in the mixture.

7.1.3   Performance of grooved backing structure with silicon

From the tests performed with the grooved structure, it is found that the structure is capable of providing attenuation which is due to the presence of the grooves at its bottom. This attenuation comes in addition to what the epoxy tungsten composite provides by itself. In CMUT transducers, there is a ringing effect which is due to thickness resonances in the silicon substrates on which CMUTs are usually manufactured. This is explained in Chapter 3 of the thesis. In this section the performance of the grooved backing structure with a silicon substrate is evaluated.

The backing material used here is prepared in a same way as explained in the earlier section. The volume fraction of tungsten is also kept the same as earlier, about 40%. The epoxy tungsten composite is allowed to cure directly at the bottom of the silicon wafer without any glue layer. Grooves are made at the bottom of the backing with the help of a patterned silicon wafer. A grooved backing structure of thickness about 200 μm is prepared at the bottom of the silicon wafer. The unintended thickness variation observed for the backing structure is within 5-10% of the total thickness. Both symmetric and asymmetric designs are used for the grooved backing structure. The thickness of the silicon wafer used is 500 μm.

Reflection measurements are performed using the vector network analyzer as earlier. The obtained specular reflection from silicon wafers with and without backing structures are shown in Figure 7.10 for the frequency range 10 MHz to 30 MHz. The thickness resonances are observed at frequencies around 16 MHz and 24 MHz for the silicon wafer without backing. These values are in accordance with the theoretical calculations. For the silicon with backing structure, the results for the specular reflection are similar, but the notches due to the thickness resonances in the silicon substrate are absent in the frequency response. The reason for the absence of notches is due to the absorption of the acoustic energy of the silicon substrate in the backing. This is true for both symmetric and asymmetric designs of the grooved backing structure. This means that a thin grooved backing structure is capable of eliminating the thickness resonances in the silicon wafer.

In Figure 7.11, time domain plots of the reflected signal from the silicon wafer with and without backing are shown. For the silicon with a backing structure, the results shown here are for the backing with symmetrically designed grooves at its bottom. The results with the asymmetrically designed
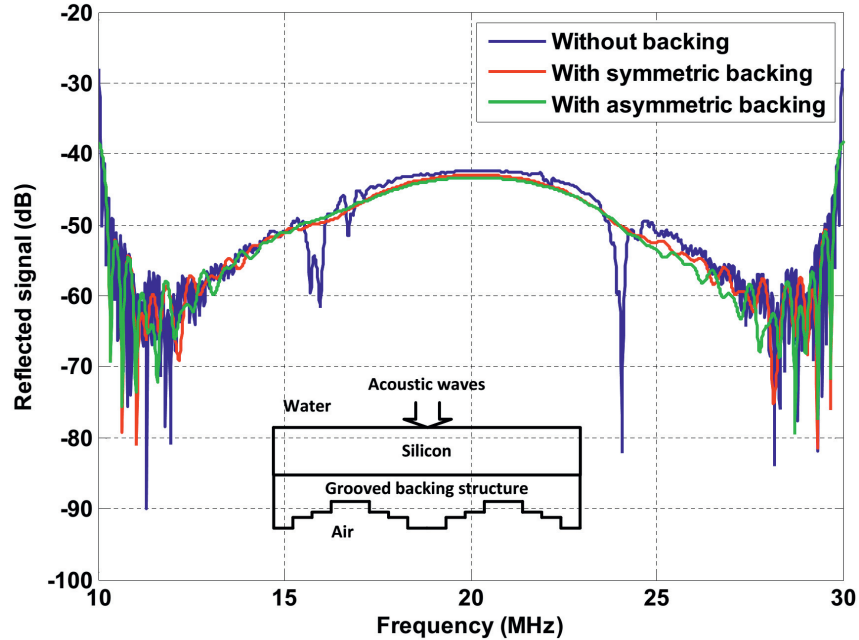
Figure 7.10: Reflected signal from the silicon wafer with and without backing.

grooves are not significantly different. Both real and imaginary parts of the signals are shown. From the figure, it is clear that the addition of the backing layer removes the ringing which is observed due to finite thickness of the silicon substrate thereby reducing the pulse duration. Therefore, the addition of a lossy backing will improve the bandwidth and the axial resolution in the imaging applications as the pulse duration of the signal will be reduced.

The time domain responses are also plotted in dB-scale in Figure 7.12 for the silicon wafers with and without acoustic backing structures. For the silicon with backing structure, we expect three interfering echoes: (1) echo from the top surface of silicon wafer, (2) echo from the silicon-backing interface, and (3) echo from the bottom surface of the backing. The first echo is from the top surface of silicon and it is essentially the same for all the cases. As we know the thicknesses and the material properties of both the silicon and the backing, the time delays for the different echoes could easily be estimated. In this work the echo from the silicon-backing interface is estimated to be about 0.125 μs from the occurrence of the first echo, and the third echo is estimated to be about 0.2 μs from the occurrence of the
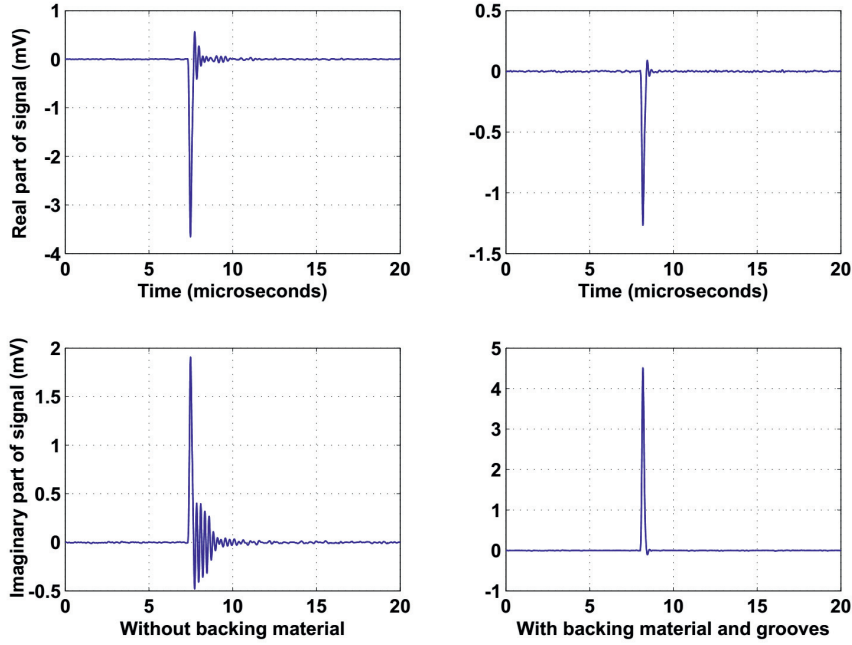
Figure 7.11: Time domain plot of the reflected signals from silicon wafer with and without backing. Note that the first echo is from the front surface of the wafer and is not affected by the backing.

second echo. The power level for the second echo is calculated to be below 25 dB compared to the first echo, but it is difficult to estimate from the figure. However, we are able to estimate the power level of the third echo. It is found to be below 40 dB compared to the first echo. Using values for the acoustic impedances of water (Z_w), silicon (Z_s) and epoxy tungsten backing (Z_b) respectively to be 1.5 MRayl, 19.6 MRayl and 14 MRayl, the total loss in the backing can then be calculated. The expressions for power transmission losses through the water-silicon interface (T_1) and the silicon-backing interface (T_2) can be written as:

$$
\begin{aligned}
T_1 &= \frac{4Z_w Z_s}{(Z_w + Z_s)^2} \quad , \\
T_2 &= \frac{4Z_s Z_b}{(Z_s + Z_b)^2} \quad .
\end{aligned}
\tag{7.4}
$$

Using the expressions for power transmission losses through the different interfaces and the observed power level of the third echo, total loss from the
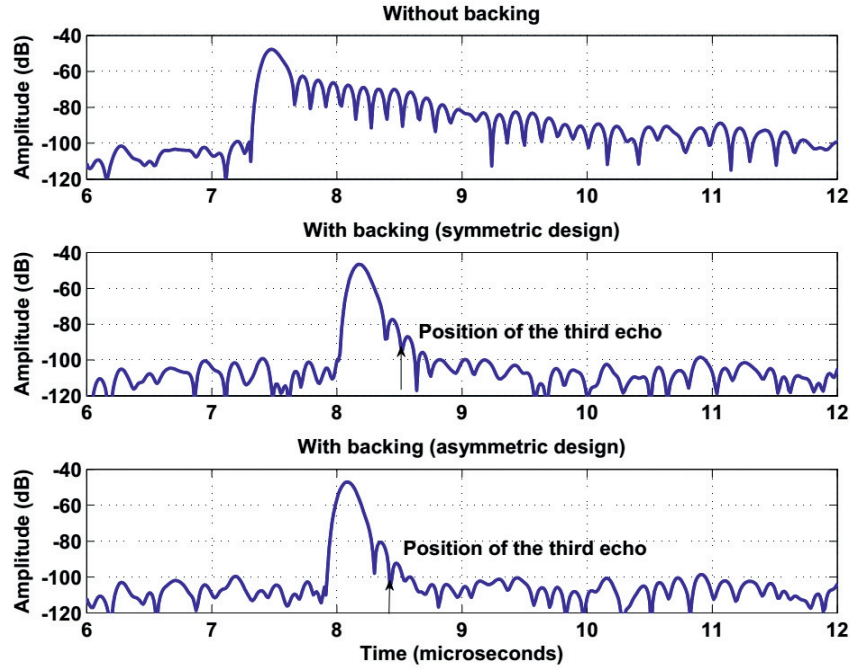
Figure 7.12: Amplitude of the reflected signals (dB) from silicon wafer with and without backing.

epoxy tungsten backing is calculated by:

$$
\begin{aligned}
\text{Loss} &= -40 + 20 log\left(\frac{(Z_s{}^2 - Z_w{}^2)(Z_s + Z_b)^2}{16 Z_w Z_s{}^2 Z_b}\right) \quad , \\
&\approx -30\text{dB} \quad .
\end{aligned}
\tag{7.5}
$$

As estimated from our measurements in an earlier section, the absorption loss in the 200 μm thick backing structure is about 12-16 dB at about 20 MHz. This means that the grooves at the bottom of the structure provide the additional loss of about 14-18 dB at about 20 MHz. This means that a grooved backing structure of thickness about 200 μm or more is able to reduce possible echo problems in the CMUT transducers.

7.2 Materials used for reducing cross coupling in CMUTs

As discussed in Chapter 3, performance of CMUT transducer is degraded not only due to the excitation of bulk waves in the silicon substrate, but also due to the crosstalk between neighbor elements. The grooved backing structure discussed in earlier section is able to minimize the artifact which is due to excitation of bulk waves in the silicon substrate, but it is not able to minimize the crosstalk effect. This effect is due to the acoustic coupling through the fluid medium outside the CMUT array. The problem has been discussed by many research groups over the years [BKY+05] [ELG05]. There have been some suggestions to use a deep trench isolation between the neighboring elements to reduce the cross coupling effect [JODKY01]. But Berg *et al.* [BR06] have shown that the fluid coupled crosstalk in CMUT arrays can be reduced effectively by using a thin lossy layer on top of the CMUT membrane. It is shown that the thickness of the lossy layer could be only a few percent of its acoustic wavelength and it should have high shear deformation loss, a loss tangent of about 0.4, to reduce the cross coupling effect significantly.

Although different polymers exist which have high shear deformation losses with small shear wave velocities, little information is available on their acoustic properties. Because of large values for shear wave attenuation of such polymers, measurement of shear wave velocity and attenuation coefficient is difficult. In this section shear wave velocities and acoustic attenuation for some of such polymers are presented based on our measurement results. The measurement technique used here is similar to what has been used by Madsen *et al.* [MSZ83] and Tordjeman *et al.* [GLF+08]. In these papers, the shear wave properties are calculated by measuring the complex reflection coefficient at the interface between the material, the shear wave properties of which are to be measured, and a silica delay line. The reflection coefficient is unity when there is air at the interface. When air is replaced by the material, the reflection coefficient changes, both in magnitude and phase. By measuring both magnitude and phase of the reflection coefficient, the shear wave velocity and attenuation coefficient could be determined.

For the measurements, we have chosen an ultrasonic delay line (isopaustic glass from *Philips*) used in analog color television receivers. A schematic of the delay line is shown in Figure 7.13 with two shear wave transducers as transmitter and receiver. The shear wave transducer in the isopaustic delay line is centered around 5 MHz. Following [ZvdB67], the density of the isopaustic glass is taken to be 3800 kg/m^3 and shear wave velocity is

taken to be 2500 m/s. A good property of such a delay line is that the time delay is almost independent of temperature. We mainly follow Madsen *et al.* [MSZ83] in the following calculations where the exponential form of a wave, $e^{j(kx-\omega t)}$, is used. Here ω is the angular frequency and k is the complex wavenumber. If Z_a and Z_b are respectively the acoustic impedances of the delay line and the material, the complex reflection coefficient of particle velocity is calculated by:

$$R = \frac{Z_a - Z_b}{Z_a + Z_b} \quad , \tag{7.6}$$

where Z_b is a complex quantity and Z_a is assumed to be a real quantity as the delay line has very little loss. As R is a complex reflection coefficient, it could also be written as:

$$R = \|R\| \, e^{j\phi} \quad , \tag{7.7}$$

where $\|R\|$ is the amplitude of reflection coefficient and ϕ is the phase difference when the material is attached at the interface instead of air.
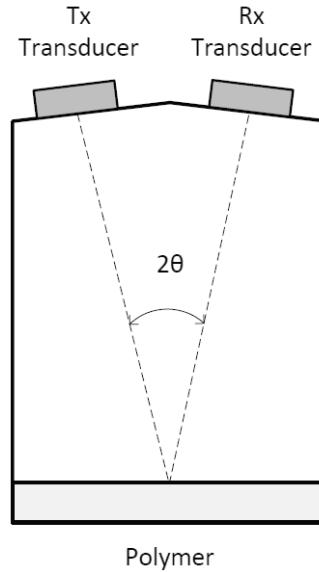
Figure 7.13: Estimation of complex reflection coefficient for shear waves for a polymer whose material properties are to be determined using an isopaustic delay line.

As the density and other properties of the isopaustic delay line are

known, the shear wave velocity and attenuation coefficient of the material can be easily calculated. If μ_a and μ_b are the complex shear moduli in media a and b respectively, and ρ_a and ρ_b are the mass densities of media a and b, the relation between complex wavenumbers and shear moduli can be expressed as

$$
\begin{aligned}
\mu_a &= \frac{\omega^2 \rho_a}{k_a^2} \quad , \\
\mu_b &= \frac{\omega^2 \rho_b}{k_b^2} \quad .
\end{aligned}
\tag{7.8}
$$

The complex reflection coefficient, R, as defined in equation (7.6) can also be written in terms of shear moduli and wavenumbers as

$$
R = \frac{\mu_a k_a - \mu_b k_b}{\mu_a k_a + \mu_b k_b} \quad .
\tag{7.9}
$$

Using equation (7.8) and (7.9), complex shear modulus in medium b can be expressed in terms of the material properties of a and the reflection coefficient R as

$$
\mu_b = \frac{\mu_a^2}{v_a^2 \rho_b} \left(\frac{1-R}{1+R} \right)^2 \quad .
\tag{7.10}
$$

The complex wavenumber, k, contains the shear wave speed of sound, v, and attenuation coefficient, α, in the form

$$
k = \frac{\omega}{v} + j\alpha \quad .
\tag{7.11}
$$

This gives us the shear velocity, v_b, and the attenuation, α_b, in the material as

$$
\begin{aligned}
v_b &= \left(real \left\{ \sqrt{\frac{\rho_b}{\mu_b}} \right\} \right)^{-1} \quad , \\
\alpha_b &= imag \left\{ \omega \sqrt{\frac{\rho_b}{\mu_b}} \right\} \quad .
\end{aligned}
\tag{7.12}
$$

For the measurement of shear wave properties, some polymers are chosen which could be used as a lossy layer on top of the CMUT membrane. The polymers chosen are RTV 615 from *Momentive Performance Materials* and Sylgard 160 from *Dow Corning*. These materials have the additional

advantage that their acoustic impedances are close to that of water. As suggested in [BR06], the soft material on the top could be covered with a thin stiff coating layer for protection without affecting the results significantly. Other polymers whose properties are studied are EPOTEK 301-2 from *Epoxy Technology* and Polymethylpentene, TPX® from *Mitsui Chemicals*. The materials discussed here could not only be used as a lossy top layer for the reduction of cross coupling in CMUTs, but they could also be used as lens materials for CMUT transducers.

For the measurement of the complex reflection coefficient, the amplitude and phase of the reflected signal from the bottom surface of the delay line were measured for two different cases, one with air at the interface and the other with the material, whose properties are to be measured, at the interface. The two transducers are excited in parallel and we are looking at the echoes in the resulting one ended delay line. Measurements were taken for the 6th echo instead of the first one because the phase shift was very small and difficult to estimate from the first echo. As it was difficult to couple to the shear wave directly by pressing the test sample towards the surface, honey was used as couplant for the measurements with epoxy and TPX. But in the cases of RTV 615 and Sylgard 160, no couplants were used, instead they were allowed to cure at the surface of the delay line at room temperature. Phase shifts for the different materials were estimated from the time delay obtained for the 6th echo. The amplitude of signals for 6th echo obtained for different materials are shown in Figure 7.14. As the shear wave velocity for the isopaustic delay line and the distance between transmit and receive transducers are known, the occurrence of the first echo in the time domain could be easily estimated. This is found to be $48.75\mu s$ from our measurements. This is different from the standard value, $64\mu s$, of the isopaustic delay line because a small portion of this delay line is chopped off.

If A_{air} and A_{mat} are respectively the amplitudes of the reflected signals for the nth echo when there is air and polymer material at the delay line interface, the amplitude of reflection coefficient is given by:

$$R = \left(\frac{A_{mat}}{A_{air}}\right)^{\frac{1}{n}} \quad , \tag{7.13}$$

and the phase shift is calculated using the time delay, Δt, for the nth echo given by:

$$\phi = \frac{\omega \Delta t}{n} \quad . \tag{7.14}$$
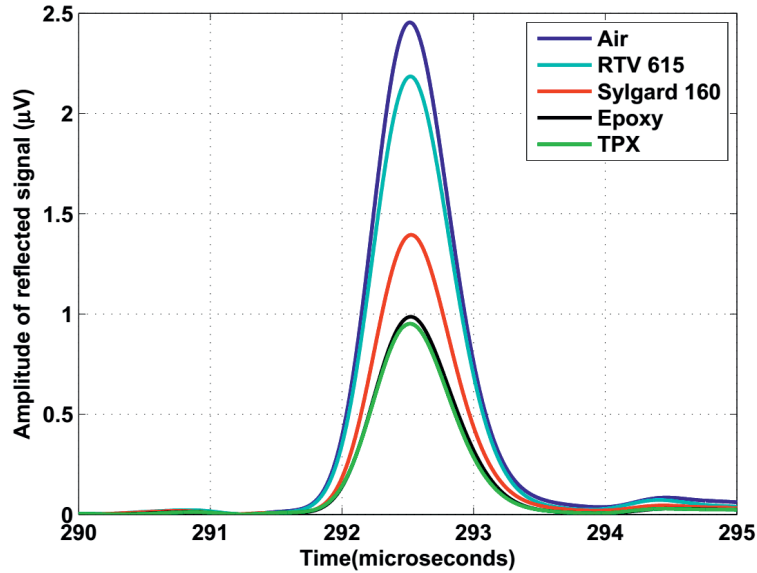
Figure 7.14: Amplitudes of reflected signals for different materials, whose shear wave properties are to be measured.

As the reflection coefficients and the densities of the materials are known, shear wave velocities and attenuation coefficients are calculated using equations (7.10) to (7.12) . The obtained results for shear velocities and attenuation coefficients for some polymers at about 5 MHz are shown in Table 7.1. The experiments were repeated several times to check whether the obtained values are consistent or not. The variation in shear velocities were within 15-20% of the values shown in the table. This variation is due to small errors in the measurement of echo as the resolution in time domain is about 3ns whereas the delay measured are in the range of tens of ns. Another source of error is that the shear waves are not exactly perpendicular to the bottom surface of the delay line, whereas the calculations are based on the normal propagation of shear waves at the interface. However, for this small angle of about 7°, calculation shows that the amplitudes of the reflected shear waves are not much different from those of normal incidence.

The obtained values for the shear wave velocities for epoxy and TPX are comparable with the results obtained by Wang *et al.* [WRC01] and Hartmann *et al.* [Har80]. The measurement of the shear velocity and attenuation coefficient for RTV 615 are available for different frequencies in [MSZ83]. At about 5 MHz, the shear velocity is about 100 m/s and attenuation co-

Table 7.1: Measurements results obtained from isopaustic delay line for different polymers at about 5 MHz.

Material	Amplitude	Phase (degrees)	Shear velocity (m/s)	Attenuation (per cm)
EPOTEK 301-2	0.9309	5.8	940	470
TPX	0.9346	4.9	1020	380
Sylgard 160	0.9101	2.1	330	370
RTV 615	0.9808	0.9	150	1700

efficient is about 2000/cm. These values are very close to results obtained from our measurements. However, the measurements done in [MSZ83] at this frequency is not for RTV that is cured at the surface of the delay line, instead it is pressed on the surface of the delay line.

Because the CMUT transducers are promising for high frequency ultrasound imaging, the performance of these materials are important at high frequencies. Therefore the measurements are also performed at about 15 MHz (third harmonic of 5 MHz) using the same isopaustic delay line. Shear wave properties of Sylgard 160 and RTV 615 are then measured at this frequency. As the losses at 15 MHz are higher than the losses at 5 MHz, measurements are taken for 4th echo instead of 6th echo. The results obtained for shear wave velocity and attenuation for these polymers at about 15 MHz are shown in Table 7.2. From the measurements with RTV 615 at 15 MHz, we know that the bonding of RTV 615 with the delay line was not very good because the stiffness obtained at this frequency was ambiguous. That is why a thin primer layer about 10-20 μm is added to have better adhesion to the surface of the delay line. The primer used is SS4120 which is recommended by *Momentive Performance Materials*. As the solid content in the primer is about 3%, the real thickness of the primer when it dries becomes roughly about 0.3-0.6 μm. Therefore a moderate change in the properties of the RTV 615 is expected with addition of the thin primer layer.

From our experiment, we were able to measure the shear wave velocities and acoustic attenuation for different polymers. The obtained results show that RTV 615 and Sylgard 160 have high shear deformation losses so that they could be used as a lossy top layer for CMUTs to reduce the acoustic cross coupling between neighbor elements. Sylgard 160 has an acoustic impedance that is closer to water than RTV 615, but RTV 615 is transparent

Table 7.2: Measurements results obtained from isopaustic delay line for different polymers at about 15 MHz.

Material	Amplitude	Phase (degrees)	Shear velocity (m/s)	Attenuation (per cm)
Sylgard 160	0.8948	2.4	380	920
RTV 615	0.9613	1.35	250	2260

which makes it easy to inspect the CMUT surface after its addition. These materials could also serve as lens material for CMUT transducers along with stiff polymers like TPX.

Chapter 8

Discussion and Conclusion

In this thesis we have discussed the backing requirements for CMUT transducers. CMUT transducers are promising for invasive ultrasound imaging applications. We know that there are possible echo problems with CMUT transducer which could be minimized by using a thick acoustic backing with significant loss. But there may not be enough space available for transducer assembly with a thick acoustic backing for such applications. Thus we have designed a grooved backing structure for CMUTs which gives a similar performance, but with a thinner backing layer. Simulations were performed for a grooved backing structure to test its performance over a wide frequency range. The backing structures were prepared and experiments were performed to validate the simulation results. The simulations performed on the grooved structure matched fairly well with the experimental results. The backing structure described here contains grooves at its bottom. For bulk waves propagating in the structures, there will not be any specularly reflected waves when the groove depth is equal to a quarter of the wavelength. In our case, the structure is designed to provide nulls in the response of the specular reflection coefficient at two freely chosen frequencies. The grooved structure also provides some attenuation over a frequency range determined by these two frequencies. This attenuation comes in addition to what the backing material provides by itself. Experiments showed that the structures provide an added attenuation of about 10-20 dB over a wide range of frequencies. The observed nulls in the specular reflection coefficient were not as sharp and well defined as in the simulation, but basically the experimental results agree well with simulations.

The main purpose of using a grooved bottom structure for backing the CMUTs is to provide an additional amount of attenuation in the frequency range of interest. The grooves served this purpose at a satisfactory level.

Simulations have shown that the structure will also work for oblique incidence when the angle is within $\pm 30°$ to the surface normal of the bottom of the structure. We have also shown that for a CMUT-backing stack immersed in a fluid medium, waves that reach into the backing from the fluid medium mostly are within this range of angles. Thus the grooved backing structure works for waves propagating in normal as well as in oblique directions to the bottom of the structure when they are used in practical applications.

Tungsten loaded epoxy is used as a backing material for CMUTs in this work. The volume fraction of tungsten used in the epoxy is about 40%, which makes the acoustic impedance of the composite material high with significant acoustic attenuation. The acoustic impedance of the composite is estimated to be about 14 MRayl by measuring the longitudinal velocity and the density of the composite. The acoustic impedance is not exactly matched with silicon substrate, on which the CMUTs are manufactured. This means that there would still be some reflection at the silicon substrate-backing interface but the magnitude of this reflected signal would be relatively small. From the experiment the attenuation in the composite material is found to be 30-40 dB/mm at 20 MHz. This means that a thick backing about 1 mm or more with such a high loss is able to reduce possible echo problems for CMUTs. But for the cases like IVUS where little space is available under the transducer, a thick backing layer could not be used. Then the grooved backing could be an alternative to save space. The grooves add 10-20 dB attenuation in the frequency band of interest which is solely due to scattering by the grooves. This attenuation comes in addition to the absorption losses in the epoxy tungsten composites. This means that we can reduce the thickness of the backing material significantly and still get the same level of attenuation.

We discussed the different possible designs on how to shape the structured bottom surface for the backing. Among the different designs, parallel grooves with an interwoven structure was chosen because it was relatively easy to design and fabricate. An anisotropically etched silicon wafer using TMAH was used as a mold to make the grooved backing structures. The silicon wafers obtained from the wet etching process did not have vertical walls in the grooves due to the anisotropic etching process used. But simulation performed on such structures showed that the performance did not differ significantly from what have been shown for vertical walls. The structure was designed to provide nulls in specular reflection at two chosen frequencies, 16 MHz and 25 MHz. Two different designs were used; one symmetric and the other asymmetric. Neglecting the effects of vertical surfaces and

corners, both designs should provide the same results. The symmetric design performed slightly better than the asymmetric design in simulation for the oblique incidence case, especially for the structures with a large period. But when the period of the structure was reduced, the symmetric design degraded more rapidly than the asymmetric design. For practical applications, a structure with a smaller period is recommended. It means that a finite width of the CMUT transducer can accommodate a few periods of the backing structure. In this case it could behave similar to an infinite structure.

There were some deviations in the experimental results from simulation results in both symmetric and asymmetric designs. The nulls were present in both designs, but not at both frequencies. Even at the frequencies where nulls were present, they were not as sharp as in the simulations. As the acoustic wavelength in the tungsten epoxy is rather small, about 100 μm at 20 MHz, small variations in thickness along the sample could have caused some inaccuracies. In fact, the variation in the thickness was found to be 10 μm to 20 μm when measured at different locations along the sample. In all the simulations, we have assumed the epoxy tungsten composite as a homogeneous isotropic material. But in practice, there are always some inhomogeneities in the material since it is not easy to control the tungsten particle concentration in the sample. These inhomogeneities might lead to velocity variations in the composite. Further the transducer used for the experiment do not have a flat frequency response. It has a frequency response centered around 20 MHz frequency, and has a 6 dB bandwidth of about 50%. So the measurements at frequencies outside this frequency range were dominated by noise. Even though the nulls were not sharp as in the simulations, there was always an attenuation of about 10-20 dB in the frequency range of interest in both designs of the backing structure.

Although the main focus of this work is on acoustic backing required for CMUTs, experiments were also performed to evaluate the shear wave properties of some polymers. When CMUTs are used for immersion applications, in addition to acoustic wave propagation, cross coupling between the neighboring elements may also degrade the response of the transducers. There has been some suggestions to use a thin lossy layer on the top of the CMUT membrane to minimize the this effect significantly. From the measurements done on two silicones, namely RTV 615 and Sylgard 160, it could be said that they have acoustic properties that are well suited for such applications. These materials could not only be used to minimize the cross coupling, but they could also be used as lens materials for CMUT transducers.

Based on the results obtained in this thesis, the following conclusions are drawn:

- Tungsten loaded epoxy is a good candidate for backing CMUT transducers as it fulfills the backing requirements for the CMUT transducers. The material serves as a high impedance backing with significant losses where acoustic energy could be dissipated without much reflection at the interface. It also serves as a mechanical support for the CMUT transducers.

- The grooves at the bottom of the backing structure provide an additional attenuation for waves propagating in normal as well as in oblique directions to the bottom of the backing structure. This means that a thin backing layer with grooves could be used instead of a thick backing layer. The CMUT transducer with such grooved backing thus reduces the total space required for the transducer assembly and makes it a strong contender for invasive ultrasound applications.

- A thin layer of silicone, either RTV 615 or Sylgard 160, could serve as a lossy layer on top of the CMUT membrane that will help to reduce the cross coupling between neighboring CMUT elements significantly.

References

[AMF⁺04]   Firas Akasheh, Todd Myers, John D. Fraser, Susmita Bose, and Amit Bandyopadhyay. Development of piezoelectric micromachined ultrasonic transducers. *Sensors and Actuators A: Physical*, 111(2-3):275 – 287, 2004.

[Ang96]   Bjørn A. J. Angelsen. *Waves, Signals and Signal Processing in Medical Ultrasonics Volume I*. Department of Physiology and Biomedical Engineering, NTNU, Trondheim, Norway, 1996.

[Ang00]   Bjørn A. J. Angelsen. *Ultrasound Imaging: waves, signals, and signal processing Volume I*. Emantec AS, Trondheim, Norway, 2000.

[Aul90]   B.A. Auld. *Acoustic Fields and Waves in Solids*. Krieger Publishing Company, 1990.

[BAS⁺13]   Hiram G Bezerra, Guilherme F Attizzani, Vasile Sirbu, Giuseppe Musumeci, Nikoloz Lortkipanidze, Yusuke Fujino, Wei Wang, Sunao Nakamura, Andrej Erglis, Giulio Guagliumi, et al. Optical coherence tomography versus intravascular ultrasound to evaluate coronary artery disease and percutaneous coronary intervention. *JACC: Cardiovascular Interventions*, 6(3):228–236, 2013.

[BB60]   L.M. Brekhovskikh and R.T. Beyer. *Waves in layered media*, volume 4. Academic press New York, 1960.

[BCD⁺10]   Sigrid Berg, Kamal Chapagain, Jon Due-Hansen, Kjell Arne Ingebrigtsen, Geir Uri Jensen, Kjersti Midtbø, Erik Utne Poppe, Arne Rønnekleiv, and Dag Thorstein Wang. Wafer bond cmut array with conductive vias, mar 2010. Publication number: US 2012/0074509 A1, U.S. Classification: 257/416.

[BCG⁺09]   Hiram G Bezerra, Marco A Costa, Giulio Guagliumi, Andrew M Rollins, and Daniel I Simon. Intracoronary optical coherence tomography: a comprehensive reviewclinical and research applications. *JACC: Cardiovascular Interventions*, 2(11):1035–1046, 2009.

[Ber79]   James G. Berryman. Theory of elastic properties of composite materials. *Applied Physical Letters*, 35(11), 1979.

[Ber94]   Jean Pierre Berenger. A perfectly matched layer for the absorption of electromagnetic waves. *Journal of Computational Physics*, 114(2):185 – 200, 1994.

[BKY⁺05]   B. Bayram, M. Kupnik, G.G. Yaralioglu, O. Oralkan, Dersong Lin, Xuefeng Zhuang, A.S. Ergun, A.F. Sarioglu, S.H. Wong, and B.T. Khuri-Yakub. Characterization of cross-coupling in capacitive micromachined ultrasonic transducers. In *Ultrasonics Symposium, 2005 IEEE*, volume 1, pages 601 – 604, sept. 2005.

[BML⁺04]   C.E. Baumgartner, D.M. Mills, R.S. Lewandowski, L.S. Smith, and D.G. Wildes. Backing material for micromachined ultrasonic transducer devices, dec. 2004. US Patent 6,831,394.

[BR06]   S. Berg and A. Rønnekleiv. Reducing fluid coupled crosstalk between membranes in CMUT arrays by introducing a lossy top layer. In *Ultrasonics Symposium, 2006. IEEE*, pages 594 –597, oct. 2006.

[BR07]   S. Berg and A. Rønnekleiv. Reduction of crosstalk in CMUT arrays by introducing double periodicities. In *Ultrasonics Symposium, 2007. IEEE*, pages 2155 –2158, oct. 2007.

[BR09]   S. Berg and A. Rønnekleiv. Challenges with acoustic backing of CMUT arrays on silicon with integrated electronics. In *Ultrasonics Symposium (IUS), 2009 IEEE International*, pages 980 –983, sept. 2009.

[BR12]   S. Berg and A. Rønnekleiv. Acoustic backing in 3D integration of CMUT with front-end electronics. *Ultrasonics, Ferroelectrics and Frequency Control, IEEE Transactions on*, 59(7):1537 –1549, july 2012.

[Bro00]   L.F. Brown. Design considerations for piezoelectric polymer ultrasound transducers. *Ultrasonics, Ferroelectrics and Frequency Control, IEEE Transactions on*, 47(6):1377 – 1396, nov 2000.

[CCC+05]   G. Caliano, R. Carotenuto, E. Cianci, V. Foglietti, A. Caronti, A. Iula, and M. Pappalardo. Design, fabrication and characterization of a capacitive micromachined ultrasonic probe for medical imaging. *Ultrasonics, Ferroelectrics and Frequency Control, IEEE Transactions on*, 52(12):2259 –2269, dec. 2005.

[CCP03]   Alessandro Caronti, Riccardo Carotenuto, and Massimo Pappalardo. Electromechanical coupling factor of capacitive micromachined ultrasonic transducers. *The Journal of the Acoustical Society of America*, 113(1):279–288, 2003.

[CCS+05]   G. Caliano, A. Caronti, A. Savoia, C. Longo, M. Pappalardo, E. Cianci, and V. Foglietti. Capacitive micromachined ultrasonic transducer (cMUT) made by a novel "reverse fabrication process". In *Ultrasonics Symposium, 2005 IEEE*, volume 1, pages 479 – 482, sept. 2005.

[Cer02]   *Piezoelectric Ceramics: Principles and Applications*. APC International Limited, 2002.

[CFM+06]   Elena Cianci, Vittorio Foglietti, Antonio Minotti, Alessandro Caronti, Gino Caliano, and Massimo Pappalardo. Fabrication techniques in micromachined capacitive ultrasonic transducers and their applications. In Cornelius T. Leondes, editor, *MEMS/NEMS*, pages 353–382. Springer US, 2006. 10.1007/0-387-25786-1-11.

[CKNP]   Stephen H. Crandall, L.G. Kurzweil, A.K. Nigam, and P.J.Remington. *Dynamic properties of modeling clay*. Acoustics and Vibration laboratory, MIT.

[CL10]   Cheng-Hsien Chung and Yung-Chun Lee. Fabrication of poly(vinylidene fluoride-trifluoroethylene) ultrasound focusing transducers and measurements of elastic constants of thin plates. *NDT and E International*, 43(2):96 – 105, 2010.

[Com08]   Comsol AB. *Comsol Multiphysics 3.5, users guide*, 1998-2008.

[Cor09]   Hitachi Corporation, may 2009. Development of Ultrasonic transducer Mappie with cMUT technology. http://www.hitachi-medical.co.jp/medix/pdf/vol51/P31-34.pdf.

[CR09]   K.R. Chapagain and A. Rønnekleiv. Minimizing the bottom reflection in ultrasonic CMUT transducer backing using low profile structuring. In *Ultrasonics Symposium (IUS), 2009 IEEE International*, pages 430 –433, sept. 2009.

[CR11]   Kamal Raj Chapagain and Arne Rønnekleiv. Measurement of the added specular reflection attenuation by using a grooved bottom surface in the backing of CMUTs. In *Ultrasonics Symposium (IUS), 2011 IEEE International*, pages 1004 –1007, oct. 2011.

[Cra70]   S.H. Crandall. The role of damping in vibration theory. *Journal of Sound and Vibration*, 11(1):3 – IN1, 1970.

[CWZ$^+$07] J.M. Cannata, J.A. Williams, Q. Zhou, H. Yu, L. Sun, E.S. Kim, and K.K. Shung. Self-focused ZnO transducers for ultrasonic biomicroscopy. In *Ultrasonics Symposium, 2007. IEEE*, pages 945 –948, oct. 2007.

[DFK78]   C.S. Desilets, J.D. Fraser, and G.S. Kino. The design of efficient broad-band piezoelectric transducers. *Sonics and Ultrasonics, IEEE Transactions on*, 25(3):115 –125, may 1978.

[DGK06]   F.L. Degertekin, R.O. Guldiken, and M. Karaman. Annular-ring CMUT arrays for forward-looking IVUS: transducer characterization and imaging. *Ultrasonics, Ferroelectrics and Frequency Control, IEEE Transactions on*, 53(2):474 –482, feb. 2006.

[DHMP$^+$12] J Due-Hansen, K Midtbø, E Poppe, A Summanwar, GU Jensen, L Breivik, DT Wang, and K Schjølberg-Henriksen. Fabrication process for CMUT arrays with polysilicon electrodes, nanometre precision cavity gaps and through-silicon vias. *Journal of Micromechanics and Microengineering*, 22(7):074009, 2012.

[DL80]   A.J Devaney and H. Levine. Effective elastic parameters of random composite. *Applied Physics Letters*, pages 377–379, 1980.

[DWB+05]   C. Daft, P. Wagner, B. Bymaster, S. Panda, K. Patel, and I. Ladabaum. CMUTs and electronics for 2D and 3D imaging: monolithic integration, in-handle chip sets and system implications. In *Ultrasonics Symposium, 2005 IEEE*, volume 1, pages 463 – 474, sept. 2005.

[EFJ74]   K.R. Erikson, F.J. Fry, and J.P. Jones. Ultrasound in medicine-a review. *Sonics and Ultrasonics, IEEE Transactions on*, 21(3):144 – 170, jul 1974.

[ELG05]   P.-C. Eccardt, A. Lohfink, and H.-G.v. Garssen. Analysis of crosstalk between fluid coupled CMUT membranes. In *Ultrasonics Symposium, 2005 IEEE*, volume 1, pages 593 – 596, sept. 2005.

[EYOKY06]   A. S. Ergun, G. G. Yaralioglu, O. Oralkan, and B. T. Khuri-Yakub. MEMS/NEMS techniques and applications. In Cornelius T. Leondes, editor, *MEMS/NEMS*, pages 553–615. Springer US, 2006. 10.1007/0-387-25786-1-16.

[GDKH77]   J. E. Gubernatis, E. Domany, J. A. Krumhansl, and M. Huberman. The Born approximation in the theory of the scattering of elastic waves by flaws. *Journal of Applied Physics*, 48(7):2812 –2819, jul 1977.

[GGR90]   Martha G Grewe, T.R. Gururaja, and Thomas R.Shrout. Acoustic properties of particle/polymer composites for ultrasonic transducer backing applications. *IEEE transactions on Ultrasonics, Ferroelectrics and Frequency Control*, 37:506–514, 1990.

[GLF+08]   J. Gasparoux, D. Laux, J.Y. Ferrandis, J. Attal, and Philippe Tordjeman. Large frequency bands viscoelastic properties of honey. *Journal of Non-Newtonian Fluid Mechanics*, 153(1):46 – 52, 2008.

[Har80]   Bruce Hartmann. Ultrasonic properties of poly(4-methyl pentene -1). *Journal of Applied Physics*, 51(1):310 –314, jan 1980.

[HEH+03]   Yongli Huang, A.S. Ergun, E. Haeggstrom, M.H. Badi, and B.T. Khuri-Yakub. Fabricating capacitive micromachined ultrasonic transducers with wafer-bonding technology. *Microelectromechanical Systems, Journal of*, 12(2):128 – 137, apr 2003.

[HHB+06]   Yongli Huang, E. Haeggstrom, B. Bayram, Xuefeng Zhuang, A.S. Ergun, Ching-Hsiang Cheng, and B.T. Khuri-Yakub. Comparison of conventional and collapsed region operation of capacitive micromachined ultrasonic transducers. *Ultrasonics, Ferroelectrics and Frequency Control, IEEE Transactions on*, 53(10):1918–1933, 2006.

[HKY94]   M.I. Haller and B.T. Khuri-Yakub. A surface micromachined electrostatic ultrasonic air transducer. In *Ultrasonics Symposium, 1994. Proceedings., 1994 IEEE*, volume 2, pages 1241 –1244 vol.2, 31 1994-nov. 3 1994.

[HN03]   K.H Ho and S.T Newman. State of the art electrical discharge machining (EDM). *International Journal of Machine Tools and Manufacture*, 43(13):1287 – 1300, 2003.

[HS63]   Z. Hashin and S. Shtrikman. A variational approach to the theory of the elastic behaviour of multiphase materials. *Journal of the Mechanics and Physics of Solids*, 11(2):127 – 140, 1963.

[Iag10]   Annamaria Iagnocco. Imaging the joint in osteoarthritis: a place for ultrasound? *Best Practice & Research Clinical Rheumatology*, 24(1):27 – 38, 2010.

[ISC11]   Antonio Iula, Alessandro Savoia, and Giosuè Caliano. Capacitive micro-fabricated ultrasonic transducers for biometric applications. *Microelectronic Engineering*, 88(8):2278 – 2280, 2011. Proceedings of the 36th International Conference on Micro- and Nano-Engineering,36th International Conference on Micro- and Nano-Engineering (MNE).

[JODKY01]   Xuecheng Jin, O. Oralkan, F.L. Degertekin, and B.T. Khuri-Yakub. Characterization of one-dimensional capacitive micromachined ultrasonic immersion transducer arrays. *Ultrasonics, Ferroelectrics and Frequency Control, IEEE Transactions on*, 48(3):750 –760, may 2001.

[KEY05]   Butrus T. Khuri-Yakub, Arif S. Ergun, and Goksen Yaralioglu. Capacitive membrane ultrasonic transducers with reduced bulk wave generation and method, apr 2005. Publication number: US 2005/0236937 A1, U.S. Classification: 310/334, International Classification: H01G007/00.

[KFCS00]   Lawrence E. Kinsler, Austin R. Frey, Alan B. Coppens, and James V. Sanders. *Fundamentals of Acoustics*. John Wiley and Sons Inc., Newyork, USA, 2000.

[Kin87]   Gordon S. Kino. *Acoustic Waves: Devices, Imaging and Analog Signal Processing*. Prentice Hall, Englewood Cliffs, N.J., 1987.

[KYO11]   Butrus T Khuri-Yakub and Omer Oralkan. Capacitive micromachined ultrasonic transducers for medical imaging and therapy. *Journal of Micromechanics and Microengineering*, 21(5):054004, 2011.

[LD77]   S. Lees and C.L. Davidson. Ultrasonic measurement of some mineral filled plastics. *Sonics and Ultrasonics, IEEE Transactions on*, 24(3):222 –225, may 1977.

[LG95]   Man Liu and D.G. Gorman. Formulation of Rayleigh damping and its extensions. *Computers & Structures*, 57(2):277 – 285, 1995.

[Liu12]   Chang Liu. *Foundation of MEMS, second edition*. Pearson Education limited, England, 2012.

[LJS+98]   I. Ladabaum, Xuecheng Jin, H.T. Soh, A. Atalar, and B.T. Khuri-Yakub. Surface micromachined capacitive ultrasonic transducers. *Ultrasonics, Ferroelectrics and Frequency Control, IEEE Transactions on*, 45(3):678 –690, may 1998.

[LKYSH95]   I. Ladabaum, B.T. Khuri-Yakub, D. Spoliansky, and M.I. Haller. Micromachined ultrasonic transducers (MUTs). In *Ultrasonics Symposium, 1995. Proceedings., 1995 IEEE*, volume 1, pages 501 –504 vol.1, nov 1995.

[LTCF96]   GR Lockwood, DH Turnball, DA Christopher, and FS Foster. Beyond 30MHz: Applications of high-frequency ultrasound imaging. *Engineering in Medicine and Biology Magazine, IEEE*, 15(6):60–71, 1996.

[LW00]   I Ladabaum and Paul A. Wagner. Silicon substrate ringing in microfabricated ultrasonic transducers. *IEEE Ultrasonic Symposium*, pages 943–946, 2000.

[LW01]   Igal Ladabaum and Paul A. Wagner. Microfabricated ultra-
            sonic transducer with suppressed substrate modes, oct 2001.
            Publication number: US 2002/0048219 A1, U.S. Classification:
            367/162, International Classification: H04R017/00.

[LWC+11]   Xiang Li, Wei Wu, Youngsoo Chung, W.Y. Shih, Wei-Heng
            Shih, Qifa Zhou, and K.K. Shung. 80-MHz intravascular ultra-
            sound transducer using PMN-PT free-standing film. *Ultrason-
            ics, Ferroelectrics and Frequency Control, IEEE Transactions
            on*, 58(11):2281 –2288, november 2011.

[mec11]   *Mechanical Micro-Machining*, pages 235–274. John Wiley &
            Sons, Inc., 2011.

[MMS00]   Don S. Mamayek, Dennis Mendoza, and Veijo Suorsa. Trans-
            ducer backing material, sep 2000. U.S. Classification: 310/327,
            International Classification: H01L 4108.

[MRW06]   K. Midtbø, A. Rønnekleiv, and D.T. Wang. Fabrication and
            characterization of CMUTs realized by wafer bonding. In *Ul-
            trasonics Symposium, 2006. IEEE*, pages 938 –941, oct. 2006.

[MSZ83]   Ernest L. Madsen, H. John Sathoff, and James A. Zagzebski.
            Ultrasonic shear wave properties of soft tissues and tissuelike
            materials. *The Journal of the Acoustical Society of America*,
            74(5):1346–1355, 1983.

[NLLP96]   T.N. Nguyen, M. Lethiecq, F. Levassort, and L. Pourcelot. Ex-
            perimental verification of the theory of elastic properties us-
            ing scattering approximations in (0-3) connectivity composite
            materials. *Ultrasonics, Ferroelectrics and Frequency Control,
            IEEE Transactions on*, 43(4):640 –645, jul 1996.

[NSC78]   R.E. Newnham, D.P. Skinner, and L.E. Cross. Connectivity
            and piezoelectric-pyroelectric composites. *Materials Research
            Bulletin*, 13(5):525 – 536, 1978.

[OEJ+02]   O. Oralkan, A.S. Ergun, J.A. Johnson, M. Karaman,
            U. Demirci, K. Kaviani, T.H. Lee, and B.T. Khuri-Yakub.
            Capacitive micromachined ultrasonic transducers: next-
            generation arrays for acoustic imaging? *Ultrasonics, Fer-
            roelectrics and Frequency Control, IEEE Transactions on*,
            49(11):1596 –1610, nov. 2002.

[Oly06]   Olympus NDT. *Ultrasonic Transducer Technical notes*, 2006.

[OP92]   Neils Ottosen and Hans Petersson. *Introduction to the finite element method*. Pearson Education limited, 1992.

[OP07]   Tuğrul Özel and Frank Pfefferkorn. Pulsed laser assisted micromilling for die/mold manufacturing. *ASME Conference Proceedings*, 2007(42908):337–342, 2007.

[PBG⁺90]   BN Potkin, AL Bartorelli, JM Gessert, RF Neville, Y Almagor, WC Roberts, and MB Leon. Coronary artery imaging with intravascular high-frequency ultrasound. *Circulation*, 81(5):1575–1585, 1990.

[PTBR05]   T.L. Proulx, D. Tasker, and J. Bartlett-Roberto. Advances in catheter-based ultrasound imaging intracardiac echocardiography and the ACUSON AcuNav^{TM} ultrasound catheter. In *Ultrasonics Symposium, 2005 IEEE*, volume 1, pages 669 – 678, sept. 2005.

[RD00]   Daniel Royer and Eugene Dieulesaint. *Elastic Waves in Solids, Volume I*. Springer, 2000.

[RLJEY97] A. Rønnekleiv, I. Ladabaum, X.C. Jin, and B.T. Ehuri-Yakub. An improved circuit model of MUTs. In *Ultrasonics Symposium, 1997. Proceedings., 1997 IEEE*, volume 1, pages 395 –399 vol.1, oct 1997.

[Røn05]   A. Rønnekleiv. CMUT array modeling through free acoustic CMUT modes and analysis of the fluid CMUT interface through fourier transform methods. *Ultrasonics, Ferroelectrics and Frequency Control, IEEE Transactions on*, 52(12):2173 – 2184, dec. 2005.

[Røn08]   A. Rønnekleiv. Fast and accurate CMUT modeling using equivalent circuits with lumped parameters. In *Ultrasonics Symposium, 2008. IUS 2008. IEEE*, pages 496 –499, nov. 2008.

[Røn09]   A. Rønnekleiv. Design modeling of cmut's for medical imaging. In *Ultrasonics Symposium (IUS), 2009 IEEE International*, pages 442–450, 2009.

[SC84]   C.M. Sayers and C.E.Tait. Ultrasonic properties of transducer backings. *Ultrasonics*, 22:57–70, 1984.

[SCZ07]   K Kirk Shung, JM Cannata, and QF Zhou. Piezoelectric materials for high frequency medical imaging applications: A review. *Journal of Electroceramics*, 19(1):141–147, 2007.

[Shu09]   K Kirk Shung. High frequency ultrasonic imaging. *Journal of Medical Ultrasound*, 17(1):25 – 30, 2009.

[Sie]   Siemens Healthcare System. ACUSON AcuNav^{TM}Ultrasound Catheter.

[SLA$^+$96]   H. T. Soh, I. Ladabaum, A. Atalar, C. F. Quate, and B. T. Khuri-Yakub. Silicon micromachined ultrasonic immersion transducers. *Applied Physics Letters*, 69(24):3674–3676, 1996.

[SNI05]   Keisuke Sugawara, Morimasa Nishihira, and Kazuhiko Imano. Experimental study of acoustic properties of (0-3) composite materials for intermediate layer or backing of ultrasonic transducers. *Journal of Applied Physics*, 44:4347–4349, 2005.

[Sto04]   Peter Stott. Handbook of the vulnerable plaque. *International Journal of Clinical Practice*, 58(7):730–730, 2004.

[Wel99]   P N T Wells. Ultrasonic imaging of the human body. *Reports on Progress in Physics*, 62(5):671, 1999.

[WLNH80]   James H. Williams, Samson S. Lee, and Hamid Nayeb-Hashemi. Ultrasonic wave propagation loss factor in composite in terms of constituent properties. *Journal of Nondestructive Evaluation*, 1:191–199, 1980. 10.1007/BF00567091.

[Woo57]   R.S. Woollett. Transducer comparison methods based on the electromechanical coupling-coefficient concept. In *1957 IRE National Convention*, pages 23 – 27, 1957.

[WRC01]   Haifeng Wang, Tim Ritter, and Wenwu Cao. High frequency properties of passive materials for ultrasonic transducers. *IEEE transactions on Ultrasonics, Ferroelectrics and Frequency Control*, 48:78–84, 2001.

[YEB$^+$03]   G.G. Yaralioglu, A.S. Ergun, B. Bayram, E. Haeggstrom, and B.T. Khuri-Yakub. Calculation and measurement of electromechanical coupling coefficient of capacitive micromachined ultrasonic transducers. *Ultrasonics, Ferroelectrics and Frequency Control, IEEE Transactions on*, 50(4):449 –456, april 2003.

[YOE+05]   David T Yeh, Omer Oralkan, Arif S Ergun, Xuefeng Zhuang, Ira O Wygant, and Butrus T Khuri-Yakub. High-frequency CMUT arrays for high-resolution medical imaging. In *Medical Imaging*, pages 87–98. International Society for Optics and Photonics, 2005.

[YT56]   C. F. Ying and Rohn Truell. Scattering of a plane longitudinal wave by a spherical obstacle in an isotropically elastic solid. *Journal of Applied Physics*, 27(9):1086–1097, 1956.

[ZTZ05]   O. C. Zienkiewicz, R. L. Taylor, and J.Z. Zhu. *The Finite Element Method: Its Basis And Fundamentals*. Butterworth-Heinemann, 2005.

[ZvdB67]   A.L. Zijlstra and C.M. van der Burgt. Isopaustic glasses for ultrasonic delay lines in colour television receivers and in digital applications. *Ultrasonics*, 5(1):29 – 38, 1967.

[ZXG+07]   Qifa Zhou, Xiaochen Xu, E.L. Gottlieb, Lei Sun, J.M. Cannata, H. Ameri, M.S. Humayun, Pengdi Han, and S.K. Shung. PMN-PT single crystal, high-frequency ultrasonic needle transducers for pulsed-wave doppler application. *Ultrasonics, Ferroelectrics and Frequency Control, IEEE Transactions on*, 54(3):668 –675, march 2007.

Part II

Selected publications

Chapter 9

Paper 1

Title: Minimizing the bottom reflection in Ultrasonic CMUT Transducer backing using low profile structuring.

In: Proceedings of IEEE Ultrasonics Symposium 2009, Rome, Italy, September 20-23, pages 430-433.

Publisher: IEEE UFFC.

Minimizing the bottom reflection in Ultrasonic CMUT Transducer backing using low profile structuring.

Kamal Raj Chapagain, and Arne Rønnekleiv
Norwegian University of Science and Technology (NTNU)
Department of Electronics and Telecommunicaitons
Trondheim, Norway
Email:{kamal.chapagain, arne.ronnekleiv}@iet.ntnu.no

Abstract

Capacitive Micromachined Ultrasonic Transducer (CMUT) transducers need an acoustic backing to ensure that any acoustic signal which propagates from the transducer into the substrate is absorbed in the backing. The backing should be made such that it does not give a false echo in the signal received by or transmitted from the transducer. Ideally, this backing material should provide high attenuation and it should match the acoustic impedance of the CMUT supporting structure (usually silicon). To avoid the echoes described above, a thick backing layer is required. But in many cases, there is little space available under the transducer so that it is difficult to accommodate a sufficiently thick layer of material with realistic propagation losses, to ensure that no signal is reflected back to the transducer. In this paper, we discuss irregular structures at the bottom surface that are used to scatter the waves. The proposed structure scatters the waves into waves with significantly changed propagation directions, giving long propagation paths back to the transducer. The structure is analyzed using FEM simulations for a simple 2D case. Different ways of implementing the structure is also discussed.

9.1   Introduction

An acoustic transducer is an electronic device used to emit and receive sound waves. Acoustic transducers are used in medical imaging, non-destructive evaluation, and other applications. CMUTs are acoustic transducers that may easily be designed to operate at high frequencies [LW00]. The CMUT is basically a vibrating capacitor. A substrate contains a lower electrode, a thin diaphragm is suspended over the substrate and a metalization layer serves as an upper electrode.

If a DC bias is applied across the lower and upper electrodes, an acoustic wave impinging on the diaphragm will set it in motion, and the variation of electrode separation caused by such motion results in an electrical signal. Conversely, if an AC signal is applied across the biased electrodes, an AC forcing function will set the diaphragm in motion, and this motion emits an acoustic wave in the medium of interest [LW00]. CMUT transducers need a supporting structure with high acoustic impedance that will not absorb an appreciable amount of power from the transducer. CMUTs are usually made on silicon, which has to be backed to absorb any acoustic signals from the transducer such that they are not reflected back into the transducer and creates false echoes. Such a backing is conveniently made from epoxy filled with tungsten powder, to make it lossy with matching impedance [GGR90].

In many applications there is little space available under the transducer such that it is difficult to accommodate a sufficiently thick layer of material with realistic propagation losses to avoid echoes. Irregular structures at the bottom surface are customary used to scatter the waves, but they also take up some space. Here we suggest a low profile structure to scatter the waves. It is similar to that proposed by Khuri Yakub et al. [KYEY08].

Silicon has rather high acoustic velocities. This means that propagation of waves from the water into the backing or vice versa is, to some degree, blocked by total reflection, except for a small range of steering angles around broadside [BR05]. Hence the more cumbersome waves reaching the bottom surface will propagate close to normal to the bottom surface.

The structure proposed in [KYEY08] consists of parallel rectangular grooves with equal width and spacing of the grooves, which, in principle, gives cancellation of specular reflection of waves when the groove depth is $\frac{1}{4}$ of the acoustic wavelength at broadside. This can be estimated using delay differences of the reflected waves. This structure scatters the waves into waves with significantly changed transverse wave vectors, giving long propagation paths back to the transducer. It may also convert longitudinal waves into shear waves which normally have much higher propagation losses

in the backing material than longitudinal waves. And in the case that waves with shifted k-vectors should reach back to the CMUTs, they will, only to a small degree, interfere with the imaging in the direction of interest. They will be suppressed by focusing.

The patent [KYEY08] discuss scattering in a narrow band. We will show that the scattering can be extended to a broader frequency range by superimposing grooves with different depths and different directions or different periodicities. The principle is to provide sets of reflecting surfaces with equal areas but different depths that may be grouped in pairs such that the depths differ by a quarter of a wavelength at a set of frequencies; the grouping is different at different frequencies. Cancellation of specular reflection at two independent frequencies requires four different depths; at three frequencies it requires eight different depths. We also discuss different ways of implementing the structure.

9.2 Material and Methods

The basic effect which is utilized in the method is visualized in Fig. 9.1.
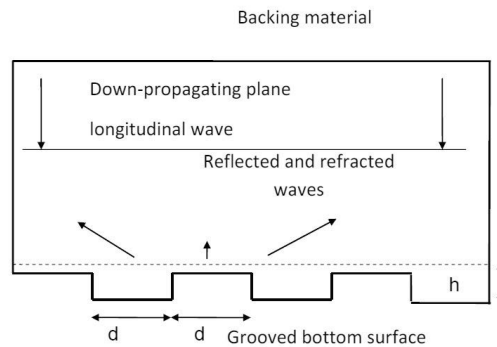
Figure 9.1: Sketch of a slab of backing material with a down-propagating plane longitudinal wave, which should be scattered and or absorbed before it returns.

A plane longitudinal wave is propagating towards a free surface which is corrugated in a periodic manner, here by rectangular grooves. The patterned grooves form a diffraction grating [KYEY08]. Diffraction gratings reflect incoming waves in normal direction as well as oblique directions to the normal. The first oblique direction for example is given by

$$\theta = \frac{\lambda}{W} \tag{9.1}$$

where $W=2d$ is the periodicity of the grating and λ is the wavelength of the wave connected to its velocity v and frequency f_R by

$$\lambda = \frac{v}{f_R} \tag{9.2}$$

The amplitudes of the diffracted orders depend on the depth of the grooves. The grooves have the same width as the distance between the grooves, d, and the groove height is h. At the dotted line, right above the bottom of the grooves, as a first approximation, there will be reflected waves with uniform amplitudes along the line, but with phase differences of $2h.2\lambda$ between regions with and without grooves.

For a phase difference of π, the groove height is related to wavelength as

$$h = \frac{\lambda}{4} \tag{9.3}$$

At a frequency where $4h = \lambda$, the phase difference is π and the amplitude of the specular reflection, the wave reflected as it would have been from a plane bottom surface, is zero. Instead the wave is converted into longitudinal and shears waves with k-vectors in the transverse direction of multiples of $\pm 2\pi/2d$. This conversion will only be effective over a rather narrow band in frequency. To be able to cover a larger band we have to use structures that effectively add several such scattering periodicities with different effective heights h. It might also be desirable that the waves are scattered more or less uniformly in all transverse directions.

We want to make several such scattering structures work independently such that each of them makes a null in the specular wave reflection coefficient at its designed frequency. To obtain this, we must arrange them such that they add $2h_i$ propagation length to signals reflected from half of the total area of any of the possible types of added propagation lengths due to the other propagation delays used. This balance in propagation delays should preferably be maintained both globally, over the complete structure, but also locally, for smaller areas everywhere in the structure.

One structure which is capable of doing this is etched squares of different sizes, where the squares of each size are organized as on a checker board. For example, the black checker board squares are etched down a certain height h_i for the ith checker board. To accommodate three heights in the balanced way described above we must scale the size of the squares in the checker boards such that there is a linear factor of at least two in size between them (two to an integer power). Four squares of the smaller pattern should be placed in one of the next larger squares and so on. Larger squares should

give cancellation at lower frequencies through choice of the height difference. The structure with three interwoven checker boards as described above is investigated by a simple numerical model. A contour plot of the height differences of the surface with such a pattern is shown in Fig.9.2. Slightly more than four by four of the larger squares (two by two of the largest periods) are shown.
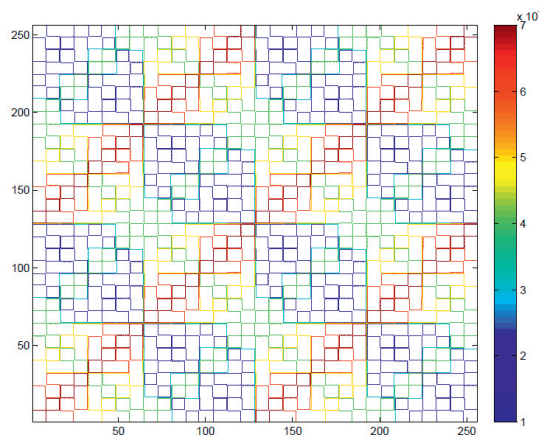
Figure 9.2: Contour plot of the heights for a part of the interwoven checker board patterns.

This structure is fairly easy to analyze, and a plot of an obtained specular reflection coefficient versus frequency is shown in Fig.9.3. The heights are chosen to give cancellation of the reflection at 15.2 MHz, 24.7 MHz, and 36.1 MHz. The cancellation at about 46 MHz is due to a 1.5λ delay difference for the 15.2 MHz structure. It is therefore less locally balanced than it could have been at this frequency.

9.3   Results and Discussion

Simulations were performed in MATLAB (The Mathworks Inc.) and COMSOL Multiphysics for some structures described above to study the reflection of waves from the bottom.

The Plain strain frequency response formulation of 2D structural mechanics module in COMSOL is used. The backing material is a composite made of epoxy with 47.5% tungsten. The epoxy is EPO-TEK 353 ND from Epoxy Tech, Inc. The material properties for the composite material are calculated using [DL80][WRC01]. The longitudinal velocity for the composite is 2024m/s and the density is 9676kg/m^3. To emphasize the effect of
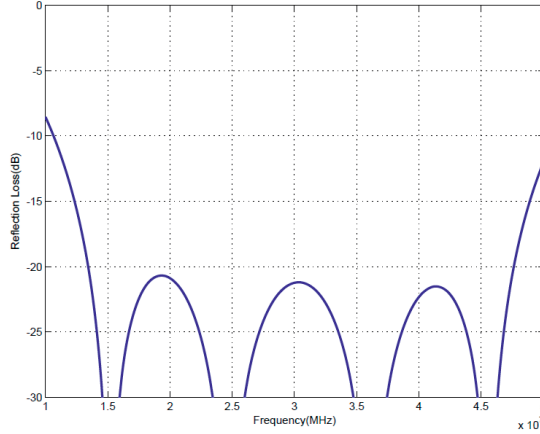
Figure 9.3: Reflection loss from the checker board structure versus fre-
quency.

the scattering, we have set the propagation losses to zero in these calcula-
tions. The uniform force is applied in longitudinal direction. To emulate the
non-reflecting boundary, perfectly matched layer (PML) is used [Com08].
To make the calculations simpler, only one period (600μm in this case) of
the structure is used with the periodic boundary condition to repeat it over
the whole structure. The structure is two-dimensional. The width and the
height of the structure are taken as 600μm and 656.625μm respectively. The
frequency analysis is performed from 10 to 40MHz.

The simulation is performed for two grooved interwoven structure as
shown in Fig 9.4. The two groove heights, h_1 and h_2 are chosen to generate
nulls at 16MHz and 25MHz. The structure shown here is the cross sec-
tion of the contour plot shown in Fig 9.2, except that the structure shown
here contains two grooved interwoven structure whereas Fig 9.2 is of three
grooved interwoven structure. As the longitudinal velocity v is 2024m/s,
the two heights as calculated using (9.3) are 31.625μm and 20.25μm.

The plot of stress and the velocity for the frequency range of 10 to 40
MHz were obtained in COMSOL. Using the plots obtained from COMSOL,
post processing is performed in MATLAB, where the obtained stresses and
velocities for the frequency range are analyzed to calculate the amplitudes of
the reflected wave in different k-directions. The obtained results are shown
in Fig 9.5 and Fig 9.6. Fig 9.5 shows the reflection loss calculated using the
delay difference method which is the ideal case and Fig 9.6 is the result as
calculated from FEM simulations. The specular reflection loss is more than
15dB for the range of frequencies from 14MHz to 28MHz. Using the FEM
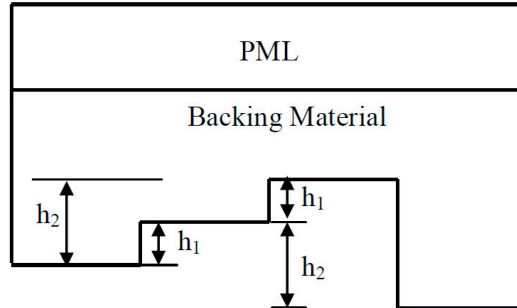
Figure 9.4: The two grooved structure in 2D showing only one period (600μm in this case) ; PML on the top of the structure is used as non reflecting boundary in COMSOL.

simulations for the two grooved structure, the reflection loss is found to be essentially the same as in ideal case.
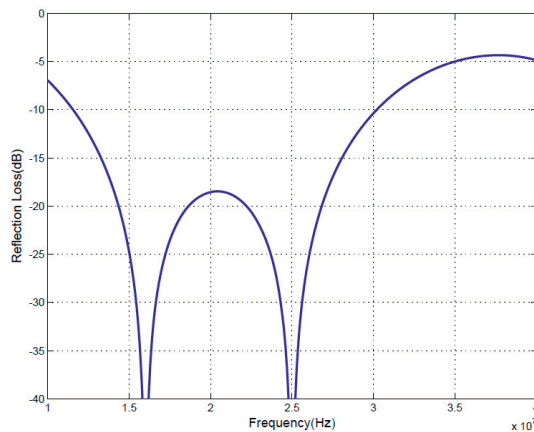
Figure 9.5: Reflection loss from the two grooved structure versus frequency using simple delay difference method.

As discussed earlier, the structure should scatter the waves in the transverse directions as longitudinal and shear waves. The amplitudes of the waves in transverse direction are plotted in Fig 9.7, which shows that these waves have large amplitude in the frequency range where there is less reflection. Furthermore, the upward shear and longitudinal transverse waves have much larger amplitudes as compared with downward waves.

This structure discussed above works well for the given frequency range but it gives large differences in linear dimensions between the low frequency
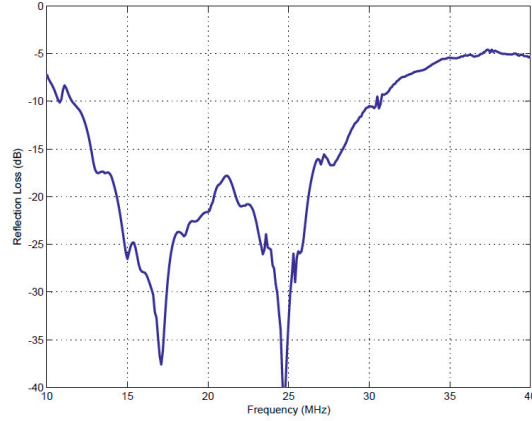
Figure 9.6: Reflection loss versus frequency for the two grooved stucture calculated using COMSOL Multiphysics.
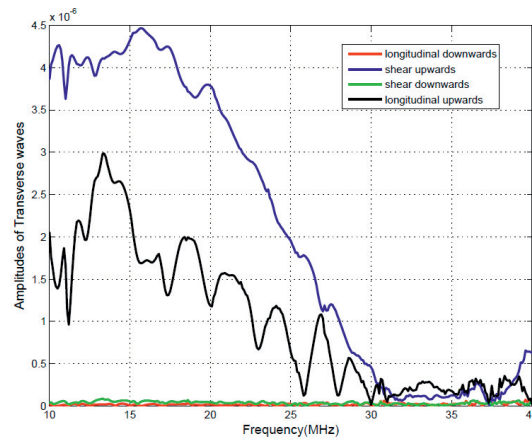
Figure 9.7: Amplitudes of particle velocity of the waves in different transverse directions.

and high frequency scatterers, with a factor of eight for a null at three frequencies. To obtain many nulls in the reflection, this means that the smallest area with full balance in reflections become fairly large. To avoid this, we could use other patterns. It is possible to use parallel grooves which have the same distance between grooves as the groove width. If we want several groove structures overlaid on top of each other such that they are all active at the same time, and balanced as described above, we may use different directions for grooves with different depth and possibly also different width which are designed to make them active at desired

frequencies.

Another possible structure is a basic pattern of two triangles which together forms a square or a rectangle. A structure which forms a balanced depth pattern combined with this could be the structure which is obtained if the square or rectangle is divided into triangles by the other of the two possible diagonals. To include more patterns one could repeat the same structure with rectangles where the dimensions in the plane are scaled up or down a factor of two.

9.4   Conclusion

The simulations presented show that the grooved structure at the bottom of the backing material adds an extra amount of loss for the plane wave propagating downwards converting them to waves in transverse directions. It, thus, helps to reduce the unwanted echoes that return back to the ultrasonic transducer.

Further work will consists of analyzing waves with different propagation directions, improving the models with different types of alternative structures described above, and investigate structures with more gradual edges that may be easier to fabricate by casting.

Acknowledgment

References

[BR05]   S. Berg and A. Rønnekleiv. Backing requirements for cmut ar-
            rays on silicon. In *Ultrasonics Symposium, 2005 IEEE*, volume 4,
            pages 1952 – 1955, sept. 2005.

[Com08]   Comsol AB. *Comsol Multiphysics 3.5, users guide*, 1998-2008.

[DL80]   A.J Devaney and H. Levine. Effective elastic parameters of ran-
            dom composite. *Applied Physics Letters*, pages 377–379, 1980.

[GGR90]   Martha G Grewe, T.R. Gururaja, and Thomas R.Shrout. Acous-
            tic properties of particle/polymer composites for ultrasonic
            transducer backing applications. *IEEE transactions on Ultra-
            sonics, Ferroelectrics and Frequency Control*, 37:506–514, 1990.

[KYEY08]   Butrus T. Khuri-Yakub, Arif S. Ergun, and Goksen Yaralioglu.
            A capacitive membrane ultrasonic transducers with reduced bulk
            wave generation and method, 2008.

[LW00]   I Ladabaum and Paul A. Wagner. Silicon substrate ringing in
            microfabricated ultrasonic transducers. *IEEE Ultrasonic Sym-
            posium*, pages 943–946, 2000.

[WRC01]   Haifeng Wang, Tim Ritter, and Wenwu Cao. High frequency
            properties of passive materials for ultrasonic transducers. *IEEE
            transactions on Ultrasonics, Ferroelectrics and Frequency Con-
            trol*, 48:78–84, 2001.

Chapter 10

Paper 2

Title: Measurement of the loss due to grooved bottom structure intended for use as a backing in Capacitive Micromachined Ultrasonic Transducers.

In: Proceedings of 34th Scandinavian Acoustics Symposium 2011, Geilo, Norway, 20 January -2 February.

Publisher: Norwegian Physical society.

Measurement of the loss due to grooved bottom structure intended for use as a backing in Capacitive Micromachined Ultrasonic Transducers.

Kamal Raj Chapagain, and Arne Rønnekleiv
Norwegian University of Science and Technology (NTNU)
Department of Electronics and Telecommunicaitons
Trondheim, Norway
Email:{kamal.chapagain, arne.ronnekleiv}@iet.ntnu.no

Abstract

The backing structure mostly used in Capacitive Micro machined Ultrasonic Transducers (CMUTs) is a composite of epoxy and tungsten powder. To be able to absorb the acoustic signals, it should have high acoustic impedance that matches with the silicon substrate (on which CMUTs are manufactured) and it should be lossy. If we are able to make this structure thick enough, then it will damp out the signal in the backing so that it would not reflect back to the transducer. But if we intend to use the transducer in applications where there is no room for the thick backing, for example in IVUS (Intravascular Ultrasound), a groove structured backing could be used [CR09]. The grooves give extra loss by scattering the waves so that a thinner backing would be enough. The scattering removes power from the specular reflection from the back surface. This reflection is otherwise harmful for the imaging. In this paper, we will present how to make such a structure. Moreover, we will present some experimental results to show that this type of structure reduces the specular reflection and compare the obtained results with theoretical calculations. It is shown that the desired reflection level for an imaging application is obtained over a wide range of frequencies around 20MHz using an absorber thickness of 200μm.

10.1   Introduction

Ultrasound transducers need an acoustic backing that ensures that any acoustic signal which propagates from the transducer into the backing is absorbed in the backing such that they are not reflected back to the transducer and create false echoes.

The backing material mostly used for ultrasonic transducers is a mixture of epoxy and tungsten powder. To be able to absorb the waves, the acoustic impedance of the mixture must be equal to that of the silicon substrate of the micromachined transducers and it must be very lossy [LW00]. If the backing is thick enough, then it will absorb most of the incoming waves. But in many applications, there is little space available under the transducer such that it is difficult to accommodate a sufficiently thick layer of material with high propagation losses. Irregular structures at the bottom surface are customarily used to scatter the waves. Here we will look at a systematic way of structuring the back surface in a way that takes little space such that it scatters the waves into waves with significantly changed propagation directions. This reduces the specular reflection, and gives long propagation paths back to the transducer for the waves. It may also convert the waves to shear waves in the backing, which normally have much higher propagation losses in the backing material than the incoming longitudinal wave.

If the irregular structure consists of parallel rectangular grooves with equal width and spacing of the grooves, it gives cancellation of the specular reflection of the waves when the groove depth is $\frac{1}{4}$ of the acoustic wavelength at broadside. This will cause strong scattering in a narrow band. The scattering can be extended to a broader frequency range by superimposing grooves with different depths and different periodicities. The principle is to provide sets of reflecting surfaces with equal areas but different depths that may be grouped in pairs such that the depths differ by a quarter of a wavelength at a set of frequencies, where high scattering is desired. Cancellation of the specular reflection at two independent frequencies requires four different depths; at three frequencies it requires eight different depths. In this paper, we have implemented a structure that gives cancellation at two independent frequencies[CR09][KYEY08].

The grooved backing structure discussed in this paper is constructed by molding the composite of epoxy and tungsten on a patterned silicon wafer. Acoustic measurements are performed on such grooved structures. Measured results are compared with theoretical calculations made for this kind of structure.

10.2 Materials and Methods

There may be different ways to create the desired type of grooved structures, such as laser micro milling, electric discharge machining (EDM), etc. Here an etched silicon wafer is chosen as a mold for making the grooved structure because of its simplicity compared to other technologies. Wet anisotropic etching of a silicon wafer with TMAH (Tetra methyl ammonium hydroxide) is implemented to create grooves because it gives smooth walls compared to other etching techniques but one possible disadvantage of this method is that it creates the smooth wall at $54.7°$ with $<100>$ plane and there is a small undercut [Liu06]. Simulations are performed on this kind of periodic structure in MATLAB using delay difference of the waves. This result was verified by implementing a FEM model for simple periodic structures using COMSOL MULTIPHYSICS (version 3.5a)[CR09][Com08]. The dimension of the structure and the depth of etching were estimated to give cancellation at two independent frequencies.

The structures prepared by anisotropic wet etching of silicon wafers were close to the design parameters used in the simulations. There were little variations around the edges and the variation of the step heights were within the tolerance limit of ± 5 to $\pm 10\%$. For the cancellation of specular reflection at two frequencies, the width of each step should be one fourth of the total period. But as we used the wet etching technique, the widths of different steps were reduced to some extent compared to the period to make them equal. Three masks are used for the creation of four step heights in the wafer. SEM pictures of the wafers after the third and the final mask are shown in figure 10.1.

For this particular case, the quarter wavelengths are chosen to give cancellation at 16 MHz and 25MHz for the epoxy and tungsten mixture. The velocity for the epoxy and tungsten composite was estimated to be 2000m/s using the Devaney model for composite materials assuming 48% tungsten by volume [DL80]. The structure is periodic with a period of 600 microns. The different depths measured were 20microns, 31 microns and 51microns. Epoxy used in the measurement is EPO-TEK 301-2 from Epoxy Technologies. The tungsten used in the experiment are mixtures of powder tungsten with different sizes ($<$1micron and 1-5microns) from Alpha Aesar company.

To estimate the loss due to the grooved structure, reflection measurement was performed using Rhodes and Schwartz vector network analyzer. Immersion type ultrasonic transducers from Olympus (Panametrics-NTD V300 series) with center frequency 20MHz were used for the experiment with the frequency swept from 10MHz to 30MHz. The obtained results

(a) (b)
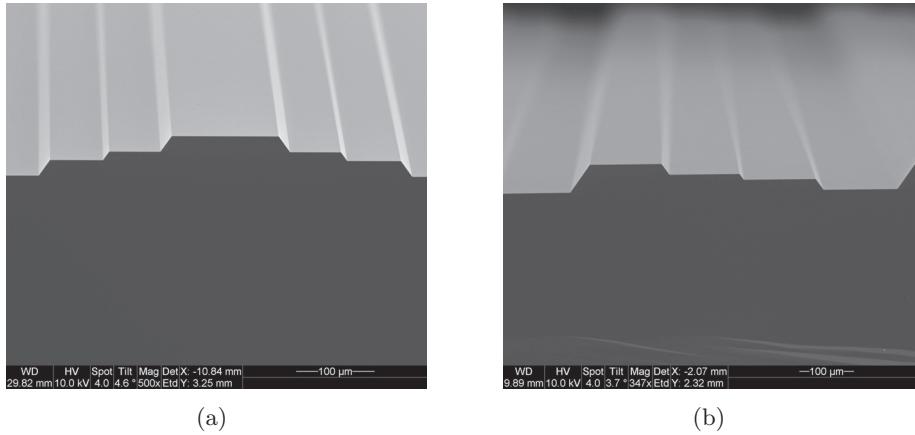
Figure 10.1: Etched silicon wafer after the third and final etch for (a) asymmetric design (b) symmetric design.

were post processed using MATLAB. Although the groove depths were optimized for the epoxy-tungsten mixture, the structures were also tested for wave propagation in water and epoxy (without tungsten). The parameters in the simulation were adjusted to give the estimated response for each case.

10.3   Results and Discussion

Acoustic measurements were performed with the grooved structure in different cases. In the first experiment, the reflection from a grooved silicon wafer, which was immersed in water, was measured with acoustic waves irradiated on grooved side. The results are shown in figure 10.2. The silicon wafers used in the measurements are 500microns thick. The experiment was repeated with a silicon wafer with the same thickness but without any grooves. The theoretical estimate of the reflection loss in water, taking velocity of water as 1500m/s, is also shown. It can be seen that the there is significant reflection loss due to grooves at 19MHz. From theoretical estimate, we would expect another dip at 12MHz. But from the measurement, we can see only a modest dip at this frequency. This is due to the reason that the signal to noise ratio is poor outside the 12-26 MHz range as 6dB bandwidth of the transducer is 48%[Oly06].

In the second case, the experiment was repeated with thin epoxy layers on silicon wafers. The wafers with epoxy were kept in water and irradiated with acoustic waves from the epoxy side, other side remaining free. Also in this case, the experiment was repeated with a silicon wafer without grooves.

(a)   (b)
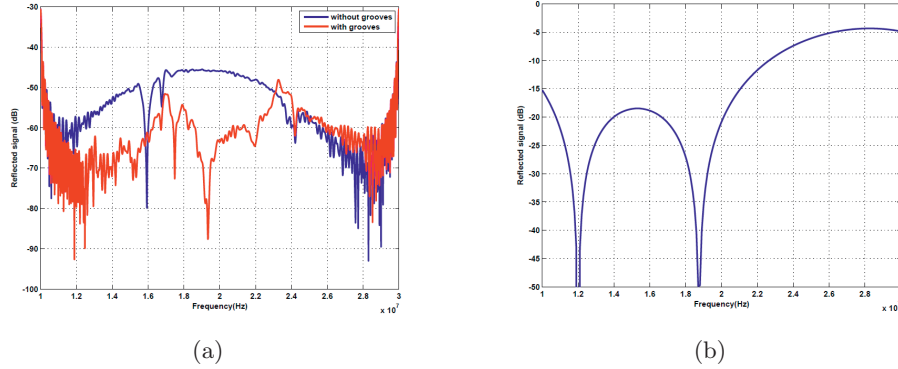
Figure 10.2: Reflection measurement with anisotropically etched silicon wafer in water (a) experimental result (b) theoretical estimate.

The results are shown in figure 10.3. We can see significant reflection loss near 20MHz which matches fairly well with the theoretical estimate. The thickness of epoxy was kept the same, 1 ±0.1mm, in both cases. Since the losses in the epoxy are very high, the signal to noise ratio is also poor in this case. From our experiment, the losses in epoxy are estimated to be 9-12dB/mm at 20MHz. For the theoretical calculation of reflection loss, the longitudinal velocity of epoxy is taken as 2500m/s. Both in the experiments with epoxy and water, dips could be seen in the curves at 16MHz and 24MHz. They are due to plate resonances in the silicon wafers. The resonance is supposed to occur at an integer m times 8 MHz ($f = m * v/2t$, velocity in silicon, v= 8000m/s and thickness, t= 500microns), which fits well with the measurements.

(a)   (b)
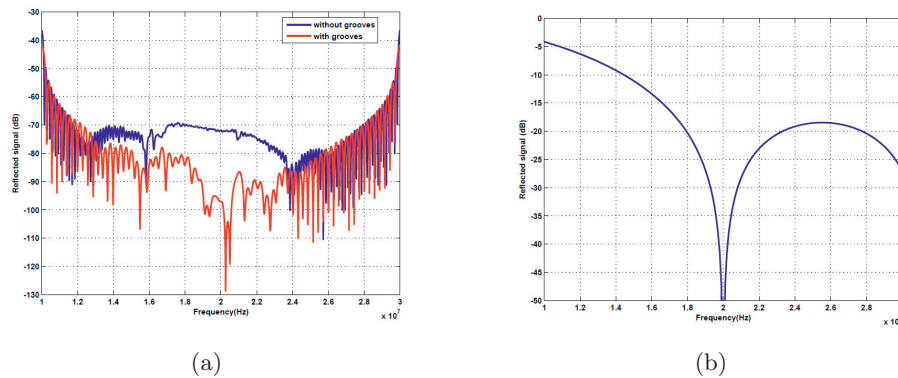
Figure 10.3: Reflection measurement with anisotropically etched silicon wafer with epoxy in water (a) experimental result (b) theoretical estimate.

The third experiment was performed with a mixture of epoxy and tung-

sten. The tungsten powder (mostly 1-5microns size and some <1microns size) was mixed with epoxy at about 40% volume fraction to get a longitudinal velocity around 2000m/s and an acoustic impedance of 12MRayl. The mixture was cast between two silicon wafers. Two samples of equal thickness were prepared, one with grooves and one without grooves. It was cured at room temperature for 24hous. The silicon wafers were covered with a thin layer of polymer so that it could easily be removed from the cured tungsten and epoxy mixture. After it was released from mold, similar measurements were repeated as in the other cases.

(a)   (b)
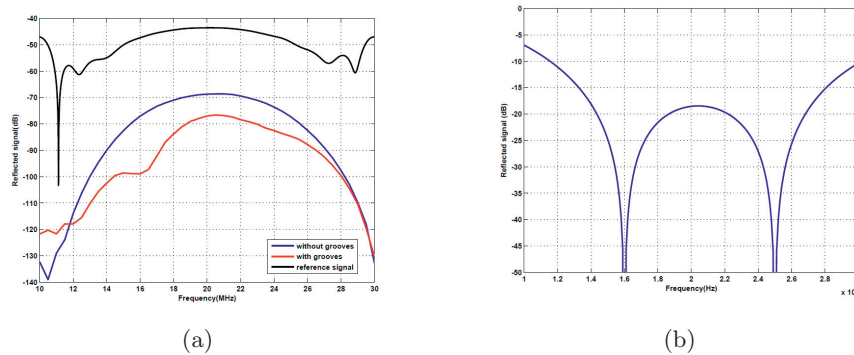
Figure 10.4: Reflection measurement with anisotropically etched silicon wafer with epoxy in water (a) experimental result (b) theoretical estimate.

As the losses in epoxy tungsten mixture is very high (30-40dB/mm as estimated from the experiment), a 200micron thick layer is used to estimate the loss due to the grooves. As the structure was thin, the echoes from the front and back surface of the specimen were superimposed in the time domain response; so it was difficult to distinguish them. To obtain the shape and level of the reflected signal from the bottom surface, we made similar reflection measurements from a single reflecting surface to get a reference signal. This signal was matched in amplitude and phase with the first part of the echo, and then subtracted from the time domain responses that we got with the epoxy and tungsten structures. In this way, we obtained an estimate of the echo from its back surface. This was done for both composite structures. These calculations assume that the epoxy tungsten mixture behaves like a uniform medium in the frequency range of interest. The experimental results along with a theoretical estimate of the scattering losses are shown in figure 10.4. It can be seen from the figure that there is significant additional reflection loss due to the grooves, about 25dB, around 16MHz, and about 10dB or more in the frequency range of 14MHz to 24MHz.
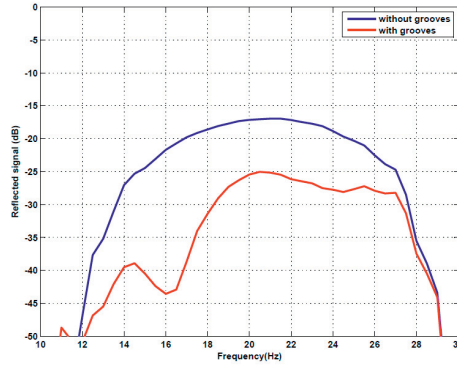
Figure 10.5: Relative reflected signal at the top of the tungsten epoxy composite with and without the grooves at the bottom.

Figure 10.5 shows an estimate of the difference in amplitude of waves going downwards and upwards at the top of the epoxy tungsten composite, both with and without grooves. This was obtained by subtracting the measured reflected signal from the bottom surface from reflected signal from top surface, and subtracting two times the transmission loss through water-composite interface, 2×4.03dB. The latter is calculated by taking the acoustic impedance of water and epoxy tungsten mixture as 1.5MRayl and 12MRayl respectively. As the noise levels are high outside 12-26MHz range, the results outside this range are somewhat uncertain.

10.4   Summary and conclusion

From the experiments, we are able to verify that the grooved structure at the bottom of the backing provide additional losses compared to a planar bottom surface. The experimental result matches fairly well with the simulation and theoretical calculations. With around 40%volume fraction of tungsten in epoxy, we were able to get additional loss of 10-20 dB in the frequency range of operation, with maximum loss of around 25dB at 16MHz, where it was designed to have a null. We would also expect additional loss at 25MHz, which is another frequency designed to have a null. At this frequency we however observe only a modest dip. One possible explanation for this could be that the top and bottom surface of the grooved structure were not exactly parallel.

Thus we can conclude that the grooved structure helps to remove the ringing effect that is encountered with most of the micromachined trans-

ducers.

Acknowledgment

References

[Com08]   Comsol AB. *Comsol Multiphysics 3.5, users guide*, 1998-2008.

[CR09]   Kamal Raj Chapagain and Arne Rønnekleiv. Minimizing the bottom reflections in ultrasonic CMUT transducer backing using low profile structuring. *IEEE Ultrasonics symposium*, pages 430–433, 2009.

[DL80]   A.J Devaney and H. Levine. Effective elastic parameters of random composite. *Applied Physics Letters*, pages 377–379, 1980.

[KYEY08] Butrus T. Khuri-Yakub, Arif S. Ergun, and Goksen Yaralioglu. A capacitive membrane ultrasonic transducers with reduced bulk wave generation and method, 2008.

[Liu06]   Chang Liu. *Foundation of MEMS*. Pearson Prentice Hall, 2006.

[LW00]   I Ladabaum and Paul A. Wagner. Silicon substrate ringing in microfabricated ultrasonic transducers. *IEEE Ultrasonic Symposium*, pages 943–946, 2000.

[Oly06]   Olympus NDT. *Ultrasonic Transducer Technical notes*, 2006.

Chapter 11

Paper 3

Title: Measurement of the added specular reflection attenuation by using a grooved bottom surface in the backing of CMUTs.

In: Proceedings of IEEE Ultrasonics Symposium 2011, Orlando, Florida, USA, October 18-21, pages 1004-1007.

Publisher: IEEE UFFC.

Measurement of the added specular reflection attenuation by using a grooved bottom surface in the backing of CMUTs.

Kamal Raj Chapagain, and Arne Rønnekleiv
Norwegian University of Science and Technology (NTNU)
Department of Electronics and Telecommunicaitons
Trondheim, Norway
Email:{kamal.chapagain, arne.ronnekleiv}@iet.ntnu.no

Abstract

The backing structure mostly used in Capacitive Micro machined Ultrasonic Transducers (CMUTs) is a composite of epoxy and tungsten powder. To be able to absorb the acoustic signals, it should have high acoustic impedance that matches with the silicon substrate (on which CMUTs are manufactured) and it should be lossy. If we are able to make this structure thick enough, then it will damp out the signal in the backing so that it would not reflect back to the transducer. But if we intend to use the transducer in applications where there is no room for the thick backing, for example in IVUS (Intra vascular Ultrasound), a groove structured backing could be used. The grooves give extra attenuation by scattering the waves in other directions so that a thinner backing would be enough. The scattering removes power from the specular reflection from the back surface. This reflection is otherwise harmful for the imaging. In this paper, we will present how to make such a structure. Moreover, we will present some experimental results to show that this type of structure reduces the specular reflection and compare the obtained results with theoretical calculations. It is shown that the desired reflection level for a medical imaging application, estimated to be about 20dB for CMUTs at the top of the backing, is obtained over a wide range of frequencies around 20MHz using an absorber thickness of 200μm.

11.1   Introduction

CMUTs comprise thin membranes which are used to transmit and receive acoustic waves. In either mode, forces are coupled not only to the membrane but also to the substrate carrying the CMUTs. This may create thickness resonances in the mounting that distorts the response of the transducer. It may also reduce the useful bandwidth of the transducer[LW00]. Thus CMUTs need an acoustic backing to ensure that acoustic signals which propagate from the transducer into the substrate are absorbed in it and are not reflected back to the transducer.

The backing material mostly used for ultrasonic transducers is a mixture of epoxy and fillers (eg. Tungsten powder, Alumina). To be able to absorb the waves, the acoustic impedance of the mixture must be equal to that of the silicon substrate of the micromachined transducers and it must be very lossy [SNI05][Hid05][SC84]. If the acoustic impedance of the silicon substrate and backing are matched, there will be no reflection back to the transducer from the interface. If it is lossy and thick enough, it would be able to absorb all the incoming waves. However, in many applications, there is little space available under the transducer so that it is difficult to accommodate a sufficiently thick layer of material with high propagation losses. Irregular structures at the bottom surface are customarily used to scatter the waves. In this paper, we will look at a systematic way of structuring the back surface such that it scatters the waves into waves with significantly changed propagation directions. This reduces the specular reflection, and gives long propagation paths for the waves going back to the transducer. It will also partly convert longitudinal waves to shear waves in the backing, which normally have much higher propagation losses than the incoming longitudinal waves [CR09].

If the irregular structure at the bottom consists of parallel rectangular grooves with equal width and spacing between them, it gives cancellation of the specular reflection of the waves when the groove depth is $\frac{1}{4}$ of the acoustic wavelength at broadside. This will cause strong scattering in a narrow band [KYEY08]. The scattering can be extended to a broader frequency range by superimposing grooves with different depths and different periodicities [CR09] . The principle is to provide sets of reflecting surfaces with equal areas but different depths that may be grouped in pairs such that the depths differ by a quarter of a wavelength at a set of frequencies, where high scattering is desired. Thus cancellation of the specular reflection at two independent frequencies requires four different depths; at three frequencies it requires eight different depths. In this paper, we have implemented a

structure that gives cancellation at two independent frequencies.

The grooved backing structure discussed in this paper is constructed by using a patterned silicon wafer as a mold for the composite of epoxy and tungsten powder. Acoustic measurements are performed on such grooved structures. Measured results are compared with theoretical calculations.

11.2   Materials and Methods

There may be different ways to create the desired type of grooved structures, such as laser micro milling, electric discharge machining (EDM), etc. Here an etched silicon wafer is chosen as a mold for making the grooved structure. Wet anisotropic etching of a silicon wafer with TMAH (Tetra methyl ammonium hydroxide) is used to create grooves because it gives smooth walls compared to other etching techniques. Possible disadvantages of this method are that it creates a smooth wall at $54.7°$ with the $<100>$ plane and there is a small undercut [Liu06]. The angle however could be advantageous as we have to demold the mixture. Simulations are performed on this kind of periodic structure in MATLAB using delay difference of the waves. This result was verified by implementing a FEM model for simple periodic structures using COMSOL MULTIPHYSICS (version 3.5a) as described in [CR09]. The dimension of the structure and the depth of etching were designed to give cancellation at two independent frequencies which requires four different step heights.

The structures prepared by anisotropic wet etching of silicon wafers were very close to the design parameters used in the simulations. There were little variations around the edges and the variation of the step heights were within the tolerance limit of ± 5 to $\pm 10\%$. For the cancellation of specular reflection at two frequencies, four step heights of equal width are needed. Thus the width of each step should be one fourth of the total period. But as we have used the wet etching technique, the widths of different steps were reduced to some extent compared to the period to make them equal. Three masks are used for the creation of four step heights in the wafer. Two different design patterns are used, one symmetric and one asymmetric. SEM pictures of the completed wafers are shown in figure 11.1.

From the figure it is clear that the surface may be split in two equal areas in two different ways, such that the height difference between the areas are $\frac{\lambda_1}{4}$ or $\frac{\lambda_2}{4}$. Hence the echoes from these surfaces cancel at λ_1 and λ_2 respectively. The structure is therefore reflection free at the wavelengths λ_1 and λ_2 for waves normal to surface. Here the two wavelengths are chosen so that the structure is reflection free at 16 MHz and 25MHz for the epoxy
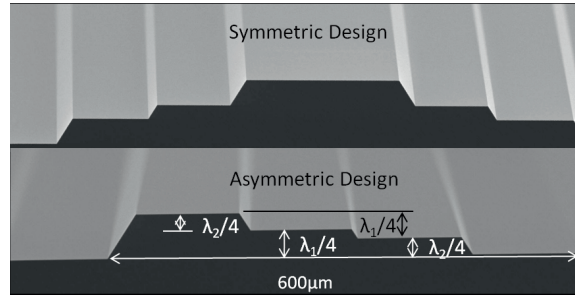
Figure 11.1: SEM images of the etched silicon wafers.

and tungsten mixture. The velocity for the epoxy and tungsten composite is estimated to be 2000m/s using the Devaney model for composite materials assuming 48% tungsten by volume [DL80][WRC01]. The structure is periodic with a period of 600μm. The different depths as designed and measured were 20μm, 31μm, and 51μm. Epoxy used in the measurement is EPO-TEK 301-2 from Epoxy Technologies. The tungsten used in the experiment are mixtures of spherical tungsten powder with different diameters ($<1\mu$m and 1-5μm) from Alpha Aesar company. To estimate the attenuation due to the grooved structure, reflection measurement was performed using Rhode and Schwarz vector network analyzer. Immersion type ultrasonic transducers from Olympus (Panametrics-NTD V300 series) with centre frequency 20MHz were used for the experiment with frequency swept from 10MHz to 30MHz. The obtained results were post-processed using MATLAB. Although the groove depths were optimized for the epoxy-tungsten mixture, the structures were also tested for wave propagation in water and epoxy without tungsten. The parameters in the simulation were adjusted to give the estimated response for each case.

11.3   Results and Discussion

Acoustic measurements were performed with the grooved structure in different cases. In the first experiment, the reflection from a grooved silicon wafer, which was immersed in water, was measured with acoustic waves irradiated on grooved side. The results are shown in figures 11.2and 11.3. The silicon wafers used in the measurements are 500μm thick. The experiment was repeated with a silicon wafer with the same thickness but without any grooves. The theoretical estimate of the reflection attenuation in water, taking the velocity of water as 1500m/s, is also shown. It can be seen that

the there is significant reflection attenuation due to grooves at 19MHz. We would also expect another dip at 12MHz based on theoretical calculations, but this is dominated by noise in our result. From the result, dips could also be seen in the curves at 16MHz and 24MHz. They are due to thickness resonances in the silicon wafers. The resonance is supposed to occur at an integer n times 8 MHz ($f = n * \frac{v}{2*t}$, where the longitudinal velocity in silicon, v= 8000m/s and silicon thickness, t= 500μm), which fits well with the measurements.
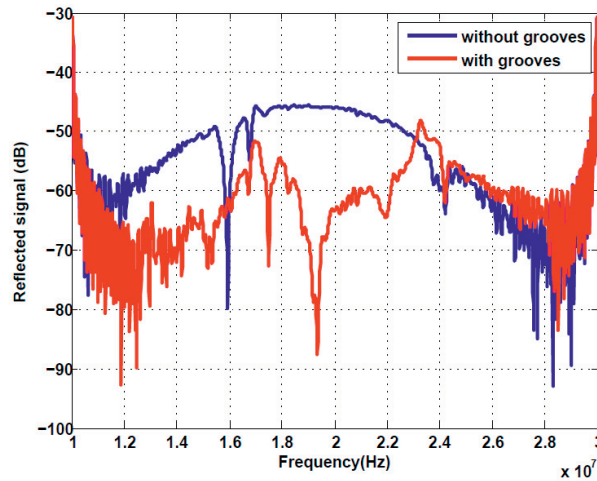
Figure 11.2: Reflected signal from silicon wafer in water with and without grooves.

In the second case, the experiment was repeated with thin epoxy layers on silicon wafers. The wafers with epoxy were kept in water and irradiated with acoustic waves from the epoxy side, the other side remaining free so that the total signal would be reflected. The experiment was also repeated with a silicon wafer without grooves. The results are shown in figures 11.4 and 11.5. We can see significant reflection attenuation near 20MHz which matches fairly well with the theoretical estimate. The thickness of epoxy was kept the same, 1$\pm$0.1mm, in both cases. Since the losses in the epoxy are very high, the signal to noise ratio is also poor in this case. From our experiment, the losses in epoxy are estimated to be 9-12dB/mm around 20MHz, which is in accordance with [GGR90]. For the theoretical calculation of reflection attenuation, the longitudinal velocity of epoxy is taken as 2500m/s. We also see that the irregularities at 8MHz and 16MHz were
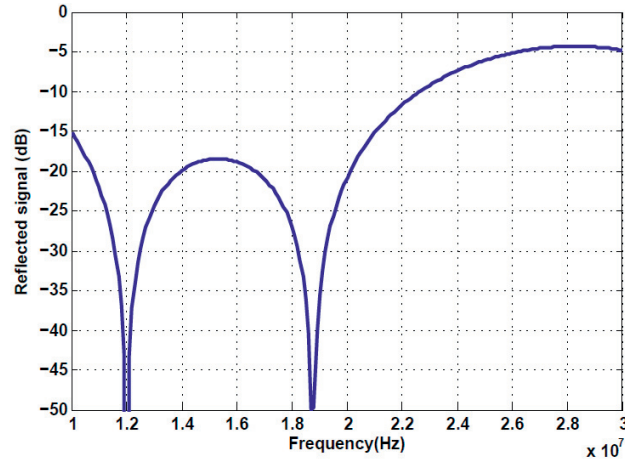
Figure 11.3: Calculated added reflection attenuation due to the grooves for silicon wafers in water.

reduced due to the presence of the grooves.

The third experiment was performed with a mixture of epoxy and tungsten. The tungsten powder (mixture of 1-5μm size (67%) and <1μm size (33%)) was hand mixed with epoxy at about 40% volume fraction to get a homogenous mixture. The mixture then was cast between two silicon wafers. Two samples of equal thickness were prepared, one with grooves and one without grooves. They were cured at room temperature for 24hours. The silicon wafers were covered with a thin layer of polymer so that it could easily be removed from the cured tungsten and epoxy mixture. After mold release, similar measurements were made as in the case of epoxy. The acoustic impedance of the composite was estimated to be about 14MRayl which was found by multiplying the longitudinal velocity with the density of the mixture. The longitudinal velocity was estimated to be about 2000m/s by the measuring the time taken by the acoustic signal to travel through the sample with known thickness. The density was estimated to be about 7000kg/m^3 by measuring the mass and the volume of the sample. Even though the percentage of tungsten in the mixture was very high, it was found to be non-conducting from electrical measurement. For electrical characterization, the capacitance was measured for a parallel plate capacitor with the epoxy-tungsten mixture as the dielectric with dimensions 20x5x1mm^3. The relative permittivity was found to be 22.5 from the experiment.

As the losses in the epoxy tungsten mixture was very high, a thin layer
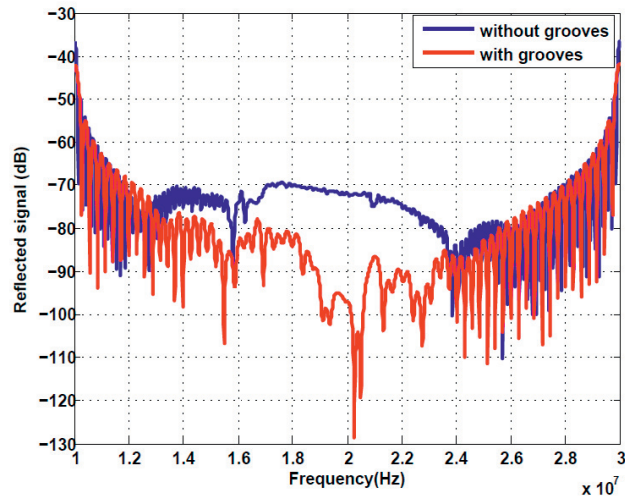
Figure 11.4: Reflected signal from the bottom side of the epoxy.
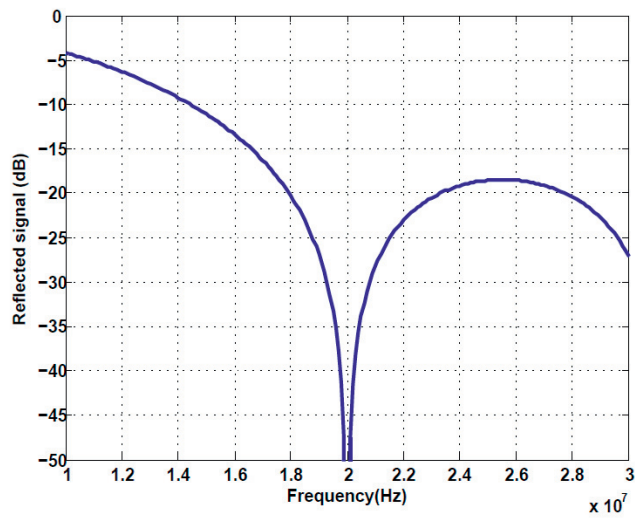
Figure 11.5: Calculated added reflection attenuation due to back side grooves for epoxy.
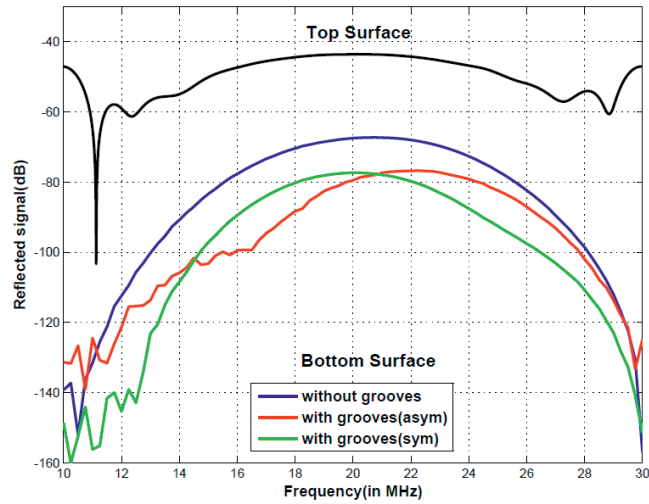
Figure 11.6: Experimental results with epoxy-tungsten composite showing reflected signal from front and back surfaces.
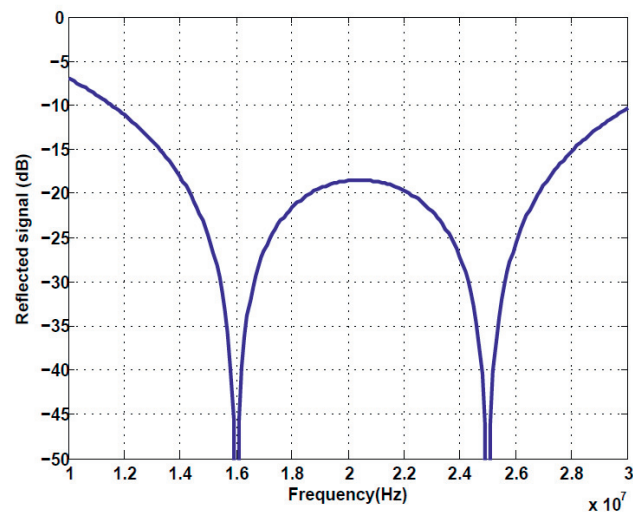
Figure 11.7: Calculated added reflection attenuation due to back side grooves for the composite.

of 200μm was used to estimate the attenuation due to the grooves. As the structure was thin, the echoes from the front and back surface of the specimen were superimposed in the time domain response; so it was difficult to distinguish them. To obtain the shape and level of the reflected signal from the bottom surface, we made similar reflection measurements from a single reflecting surface to get a reference signal. A thicker plate was used in order to separate the reflection from the front and back surface. This signal was matched in amplitude and phase with the first part of the echo, and then subtracted from the time domain responses we got with the epoxy and tungsten structures. In this way, we obtained an estimate of the echo from the back surface. This was done for all composite structures, without grooves and with grooves, both symmetric and asymmetric. These calculations assume that the epoxy tungsten mixture behaves like a uniform medium in the frequency range of interest. The experimental results along with a theoretical estimate of the attenuation are shown in figures 11.6and 11.7. For the asymmetric case, it can be seen from the figure that there is significant additional reflection attenuation due to the grooves, about 25dB, around 16MHz, and about 10dB or more in the frequency range of 14MHz to 24MHz. In the case of symmetric design, there is 10dB or more attenuation in the frequency range 13MHz to 26MHz, with a small increase in the added attenuation, to about 16dB around 25MHz.

In Figure 4(a), the reflected signal from the top surface of the composite is also shown. From the figure, the difference in amplitude of waves going downwards and upwards at the top of the epoxy tungsten composite can be estimated (both with and without grooves). This is obtained by taking the difference between the measured reflected signal from the bottom and the top surface, and subtracting two times the transmission loss through the water-composite interface, which is 4.56dB for this case. The latter is calculated by taking the acoustic impedance of water and epoxy tungsten mixture as 1.5MRayl and 14MRayl respectively. This gives a two way loss in the 200μm thick epoxy-tungsten composite as 12-14dB or 30-40dB/mm around 20MHz. The added 10dB or more attenuation from the grooves corresponds to an added thickness of the damping layer of 170μm or more. As the 6dB bandwidth of the transducer is about 48%, the result outside 13-25MHz is somewhat uncertain as it is dominated by noise [Oly06].

11.4   Conclusion

From the experiments, we are able to verify that the grooved structure at the bottom of the backing provide additional attenuation compared to a

planar bottom surface. The experimental result matches fairly well with the simulation and theoretical calculations. With around 40%volume fraction of tungsten in epoxy, we were able to get an additional attenuation of 10-20 dB in the frequency range of operation for both designs, with a maximum of about 25dB at 16MHz for the assymetric design. For the other cases where high attenuation is expected, only a modest increase at 25MHz for the symmetric case is observed. At 16MHz in the symmetric case and 25MHz in asymmetric case, no local increase in attenuation is observed. One possible explanation for this could be that the top and bottom surface of the grooved structure were not exactly parallel. In fact, there was small variations, 10-20μm, in the thickness of the sample when measured at the different points. Also non-homogeneity of tungsten powder in the epoxy-tungsten mixture along the sample dimension could cause some anomalies.

We conclude that the grooved backing structure helps to remove the ringing effect that is encountered with most of the micromachined transducers. It is particularly useful in cases where there is limited space available under the transducer. In this case, a thick backing layer could be replaced by a thin backing layer with grooved bottom surface.

Acknowledgment

References

[CR09]   Kamal Raj Chapagain and Arne Rønnekleiv. Minimizing the
           bottom reflections in ultrasonic CMUT transducer backing using
           low profile structuring. *IEEE Ultrasonics symposium*, pages 430–
           433, 2009.

[DL80]   A.J Devaney and H. Levine. Effective elastic parameters of ran-
           dom composite. *Applied Physics Letters*, pages 377–379, 1980.

[GGR90]   Martha G Grewe, T.R. Gururaja, and Thomas R.Shrout. Acous-
           tic properties of particle/polymer composites for ultrasonic
           transducer backing applications. *IEEE transactions on Ultra-
           sonics, Ferroelectrics and Frequency Control*, 37:506–514, 1990.

[Hid05]   U. Hideki. Microfabricated ultrasonic transducer with sup-
           pressed substrate modes, 2005.

[KYEY08]   Butrus T. Khuri-Yakub, Arif S. Ergun, and Goksen Yaralioglu.
           A capacitive membrane ultrasonic transducers with reduced bulk
           wave generation and method, 2008.

[Liu06]   Chang Liu. *Foundation of MEMS*. Pearson Prentice Hall, 2006.

[LW00]   I Ladabaum and Paul A. Wagner. Silicon substrate ringing in
           microfabricated ultrasonic transducers. *IEEE Ultrasonic Sym-
           posium*, pages 943–946, 2000.

[Oly06]   Olympus NDT. *Ultrasonic Transducer Technical notes*, 2006.

[SC84]   C.M. Sayers and C.E.Tait. Ultrasonic properties of transducer
           backings. *Ultrasonics*, 22:57–70, 1984.

[SNI05]   Keisuke Sugawara, Morimasa Nishihira, and Kazuhiko Imano.
           Experimental study of acoustic properties of (0-3) composite

materials for intermediate layer or backing of ultrasonic transducers. *Journal of Applied Physics*, 44:4347–4349, 2005.

[WRC01]   Haifeng Wang, Tim Ritter, and Wenwu Cao. High frequency properties of passive materials for ultrasonic transducers. *IEEE transactions on Ultrasonics, Ferroelectrics and Frequency Control*, 48:78–84, 2001.

Chapter 12

Paper 4

Grooved Backing Structure for CMUTs.

Kamal Raj Chapagain, and Arne Rønnekleiv
Norwegian University of Science and Technology (NTNU)
Department of Electronics and Telecommunicaitons
Trondheim, Norway
Email:{kamal.chapagain, arne.ronnekleiv}@iet.ntnu.no

Abstract

Capacitive Micromachined Ultrasonic Transducers (CMUTs) manufactured
on silicon substrates need an acoustic backing to suppress substrate ringing
when such transducers are in operation. The acoustic backing mostly used
for ultrasound transducers is a composite of epoxy and tungsten powder. To
absorb the acoustic energy, the backing of a CMUT should have an acoustic
impedance that matches with the silicon substrate and it should be lossy.
If the backing is thick enough, it will absorb the acoustic wave in the back-
ing without reflecting back to the transducer and thus will not create any
trailing echoes. But if we intend to use the transducer in applications where
there is no room for a thick backing, for example in IVUS (Intravascular
Ultrasound), a grooved backing structure might be used. The grooves at the
bottom of the backing provide an extra attenuation by scattering the waves
in different directions so that a thinner backing would be sufficient. The
scattering removes power from the specular reflection from the back surface
which otherwise degrades the image quality. It has been shown that this
type of structure reduces the specular reflection for a range of frequencies.
When CMUTs are used in practical applications, the propagation of waves
from a fluid medium into the backing or vice versa is blocked to some degree
by total reflection, except for a range of steering angles around broadside.
This is due to the difference in acoustic velocities of silicon and the fluid
medium. This blocking is accompanied by the generation of surface waves
in the silicon substrate, which also may impact the imaging and therefore
must be controlled. In this paper we investigate acoustic signal transmitted
into the backing relative to the signal transmitted into the fluid medium
when CMUT arrays on top of the silicon substrate are excited. Further-
more, the performance of the grooved backing structure is studied for the

waves traveling in normal as well as in oblique directions to the bottom surface of the backing.

12.1   Introduction

CMUT is an emerging technology in the field of medical imaging after its first demonstration in the early 90s [HKY94, SLA$^+$96, LJS$^+$98]. CMUT transducers promise some advantages compared to piezoelectric transducers. It may potentially become a low cost technology as it is a batch fabrication process based on micromachining of silicon. This technology makes it easy to create large 1-D or 2-D arrays. It is easy also to fabricate CMUTs that offer high bandwidths which make them useful in applications requiring good range resolution. Due to the smaller dimensions feasible with microfabrication, it is scalable to generate high frequencies, which is desirable in applications like intravascular ultrasound (IVUS) [DGK06]. And thanks to its fabrication process, it may be easy to integrate with electronics [MRW06, DWB$^+$05].

CMUTs comprise thin membranes which are used to transmit and receive acoustic waves. In either mode, forces are coupled not only to the membrane but also to the substrate carrying the CMUTs. This may create thickness resonances in the substrate that distort the response of the transducer. This effect is referred to as silicon substrate ringing [LW00]. It may reduce the useful bandwidth of the transducer and it may also lead to mechanical cross-coupling between transducer elements. Thus CMUTs need an acoustic backing to ensure that acoustic signals which propagate from the transducer into the substrate are absorbed and are not reflected back into the medium where the transducer is operating.

The acoustic backing mostly used for ultrasonic transducers is a composite of epoxy and filler particles (eg. Tungsten powder, Alumina) [SC84, NLLP96, GGR90, WRC01]. To absorb the waves efficiently, the acoustic impedance of the composite should be similar to that of the silicon substrate of the CMUT transducers, and it should be lossy [SNI05, LW05]. If the backing is acoustically perfectly matched to the silicon substrate, there will be no reflection back to the transducer from the silicon-backing interface. And if the backing is lossy and thick enough, it will absorb all the incoming waves. However, in many applications there is little space available under the transducer so that it is difficult to accommodate a sufficiently thick layer of material with high propagation losses. For example, in a catheter based ultrasound imaging system, ACUSON AcuNav^{TM}[Sie], the available space for acoustic backing material with adequate attenuation at 4MHz is 0.5mm

or less [PTBR05]. Irregular structures at the bottom surface are often used to scatter the waves and thus to reduce the specular reflection. The ultimate goal of our transducer design is to obtain a high suppression of the specularly reflected waves by combining material loss with scattering from the structured surface of the backing. In this paper we propose a systematic way of structuring the back surface such that it scatters the incoming waves into waves with significantly changed propagation directions. This reduces specular reflection, and gives effectively longer propagation paths for the waves before they eventually may appear at the transducer. It will also partly convert longitudinal waves to shear waves in the backing, which normally have much higher losses than the longitudinal waves. In the case that waves with shifted k-vectors should reach back to the CMUTs, they will only to a small degree interfere with the imaging as they will be further suppressed by the focusing of the array.

If the structure at the bottom consists of parallel rectangular grooves with equal width and spacing between them, ideally it gives cancellation of the specular reflection of normally incident waves when groove depth is a quarter of the acoustic wavelength at broadside. This will cause strong scattering in a narrow frequency band as explained by Khuri-Yakub *et al.* [KYEY08]. The scattering can be extended to a broader frequency range by superimposing grooves with different depths and different periodicities [CR09]. The principle is to provide sets of reflecting surfaces with equal areas but different depths that may be grouped in pairs such that the depths differ by a quarter wavelength at a set of frequencies, where high scattering is desired. Thus cancellation of the specular reflection at two independent frequencies requires four different depths; at three frequencies it requires eight different depths. In this paper we investigate a structure that gives cancellation of the specular reflection at two independent frequencies.

The work presented in this paper is an extension of works presented in [CR09] and [CR11]. In [CR09] the simulation of a backing structure for CMUT was described which provides scattering over a frequency range. This approach contains a structure of two interwoven parallel grooves at its bottom. In [CR11] experiments were performed to demonstrate the validity of the simulation. It has been shown that the described structures at the bottom of the backing would contribute to an additional attenuation of about 15-20dB for a wide range of frequencies around 20MHz. In [CR09] absorption loss in the epoxy tungsten composite was not included in the simulation to investigate the reduction in specular reflection that is solely due to grooves at the bottom of the structure. The results are improved in this paper by including the absorption loss along with the scattering loss.

The structures are referred to as grooved backing structures in this work.

The longitudinal wave acoustic velocity in silicon is about six times that of water [Che12]. This means that propagation of waves from a fluid medium through the silicon substrate into the backing or vice versa is, to some degree, blocked by total reflection, except for a range of steering angles around broadside [BR09, BR05]. Hence the waves reaching the bottom surface will propagate close to normal to the bottom surface. In [CR09] and [CR11] the structure was studied only for waves propagating normal to the bottom surface. In this paper we investigate the longitudinal waves that reach the backing when CMUT arrays on top of the silicon substrate are excited. At the same time, the performance of the grooved backing structure is studied when waves are incident in normal as well as in oblique directions to the bottom of grooved backing structures. Both normal and oblique incidence cases are simulated using the finite element analysis software COMSOL Multiphysics (version 3.5a), whereas the results are post-processed using Matlab. The structure is considered to be infinite in the direction of the grooves here. Therefore the simulation is performed for a 2D case. It means that tilt along the grooves is not possible. Tilt along the grooves is expected to change the results less than tilt in the orthogonal direction discussed here as shading effects of the groove walls are avoided. But it would require 3D simulations and hence much larger computational resources to do such calculations. The analysis further assumes that both the CMUT array and the backing structure are infinitely wide. For a finite array width, this will be a good approximation, provided that the period of the structure is a small fraction of the total array width.
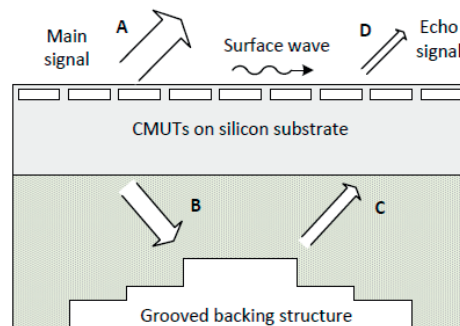
Figure 12.1: An illustration of a CMUT array on silicon substrate with grooved backing structure operating in a fluid medium.

A CMUT array on a silicon substrate with such a grooved backing structure operating in a fluid medium is illustrated in Figure 12.1. In this work

we mainly focus on issues related to the excitation of acoustic waves in the substrate, not on fluid coupled crosstalk due to neighbor coupling of CMUTs. The acoustic waves include surface acoustic wave, SAW, on the silicon fluid interface and bulk waves propagating into the backing that may be reflected back into the fluid. Both may degrade the imaging. As shown in [BR12], a thick silicon substrate gives strong coupling to SAW, and hence large degradations, but as shown here it also gives some degree of total reflection of tilted bulk waves at the fluid silicon interface. It therefore reduces the degradation due to bulk waves reflected from the bottom of the backing. Hence the thickness of the silicon substrate shown in the figure is a critical parameter. The silicon substrate may consist of several silicon wafers for electronics with bonding layers in between. In the case of several silicon wafers, we assume that the bonding between the layers are acoustically perfect. In order to bond thin layers together, there exists different techniques such as solid-liquid interdiffusion (SLID) bonding, direct fusion bonding, and anisotropic conductive adhesives (ACA). Berg *et al.* [BR12] have shown that the direct fusion bonding technique provide acoustically good bonding between the thin silicon wafers. Unlike the high temperature wafer bonding technique used for manufacturing CMUTs, the fusion bonding discussed in [BR12] is a low temperature, non-adhesive covalent bonding technique that allows high interconnect density. It uses metal-to-metal connections at the bond points using through silicon vias. The other techniques mentioned above could also be beneficial if the bonding layer thickness is very small, but at present some improvements are needed for them when it comes to bonding layer thickness. However, there are many possible ways for the integration of CMUT and electronics [DWB+05, WZY+08].

When CMUT arrays on top of the silicon substrate are excited, the bulk waves may reflect back into the fluid medium after propagating through the substrate and backing. This result in a delayed transmit signal echo which, if strong enough, will degrade the image quality. When ultrasound transducers are used for medical imaging, the resulting echo signal must be suppressed compared to the main signal to avoid image degradation. The requirements for suppression depend on the required dynamic range of the imaging system, which may vary with the medical applications. Somewhat arbitrarily we chose this to be 40dB in transmission or reception in the present paper. Referring to Figure 12.1, if A is the main signal and D is the resulting echo signal, we can write

$$\left(\frac{D}{A}\right)_{dB} = \left(\frac{D}{C}\right)_{dB} + \left(\frac{C}{B}\right)_{dB} + \left(\frac{B}{A}\right)_{dB} \leq -40dB \qquad (12.1)$$

The grooves created at the bottom of the backing will reduce the specular reflection from the backing and therefore reduce the second term of (12.1). This will be discussed in detail in sections 12.3 to 12.6 below. In section 12.2 we will calculate the first and the last terms when well backed CMUT transducers are excited in a fluid medium. The first term gives the coupling of the acoustic signal reflected from the backing into the fluid medium, and the third term gives the acoustic signal transmitted into the backing relative to the signal transmitted into the fluid medium.

To ease the calculations we perform the calculations in the Fourier domain, i.e. considering signal in frequency and k-vector space. It should be realized that the structures we consider are linear, meaning that time and spatial functions could be obtained from the spectra by an inverse complex Fourier transform. We look at the CMUT array only in transmission. Our main interest here is to establish the relative level of trailing echoes in the output signal, which may cause false delayed echoes in the imaging. Since the structure mainly is linear including the mechanical part of the CMUT array, similar trailing echoes will be generated also in reception.

A different fabrication process for CMUTs that helps to minimize the effect of substrate ringing has been suggested. This process known as *Reverse fabrication* is proposed by Caliano *et al.* [CCS$^+$05, CCS$^+$08]. In this process, the bulk silicon substrate is removed and only a few micron thick layer of silicon nitride is present under the cavity. Thus the substrate ringing effect which is due to the thickness resonances is much reduced. Acoustic backing, however, is needed to provide the mechanical support for the device. Such a backing layer does not have any requirements to match acoustically to silicon, so they are fairly easy to define. But there are still possible problems with echoes which must be removed for good performance of CMUTs.

This means that regardless of the fabrication techniques, acoustic backing is always needed for CMUTs. And the grooved backing structure would help to minimize the space requirement for the transducer assembly as it contributes additional attenuation by scattering.

12.2   Wave propagation in a CMUT backing stack

To integrate electronics with CMUTs, electronic circuits and CMUT arrays made on separate wafers can be bonded together with acoustic backing to form a 3D stack. Surface acoustic waves (SAW) might be generated when such devices are used in a fluid medium with off axis beam steering [BR09, JDC$^+$98]. These waves may contribute to the total acoustic crosstalk

in CMUT arrays. The response of a CMUT array as discussed above is degraded not only due to SAW waves but also due to excitation of bulk waves that propagate through the substrate and reflect back to the transducer. Berg *et al.* [BR12] have shown that for a stack of CMUTs including wafer electronics and different bonding layers, an acoustic backing layer that provides 20dB loss at the bottom of the stack for specular reflection can reduce the ringing due to the propagation of such bulk waves to acceptable levels for the investigated cases.
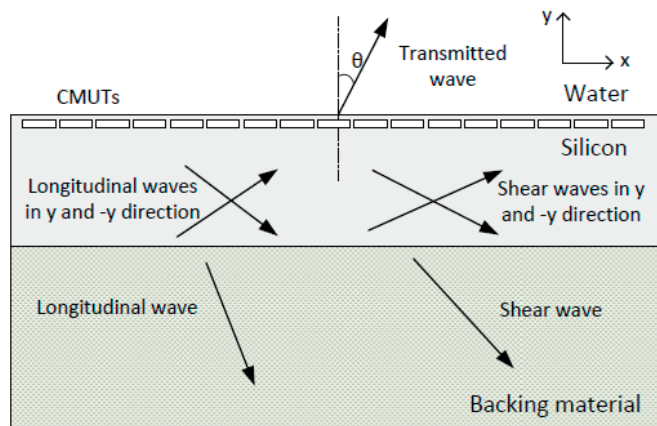
Figure 12.2: Transmitted wave into water, and transmitted longitudinal and shear waves in silicon-backing stack operating in water when CMUTs on top of the silicon substrate are excited.

In this section, we discuss how factors other than the reflectivity of the backing influence the signal degradation for the CMUT array. In the discussion we assume water as the fluid medium and look in detail at the transmission case, but due to reciprocity the results are valid also in reception. The theory considers plane waves propagating in several layered media bounded by infinite, parallel interfaces based on Auld [Aul90]. The backing material is assumed to be cured directly at the bottom of the silicon substrate without any glue layer. The waves excited in various layers due to CMUTs vibrating on top of the silicon substrate are shown in Figure 12.2. The center frequency of the CMUT is chosen to be 25MHz. The grooved backing structure which will be discussed in sections from 12.3 to 12.6 is therefore designed to provide low specular reflection for a frequency range from 12.5MHz to 37.5MHz.

There is a wide variety of possible CMUT designs. For the calculations in this section we assume a simple idealized CMUT structure. It is a massless layer between the fluid and the substrate which may be expanded

and compressed vertically in response to an exciting voltage. This gives its top surface a vertical velocity, v_{ex}, compared to its bottom surface. It has an acoustic impedance which matches to the impedance of the fluid for all steering angles, provided that the substrate is infinitely stiff. A real CMUT will differ from this idealized model in several ways. It will include mass in the CMUT plate and there will be reactive forces accelerating the fluid. Further limited coupling coefficient and electrical parallel capacitances means that the CMUT will not be electrically matched to acoustic load as assumed here. This will in most of the cases mean that at the center frequency the CMUTs will be acoustically softer than given by our model. The forces acting on the substrate will be non-uniform on the scale of CMUT and element diameters. However due to the high acoustic velocities in silicon compared to water, it will only be an average value of these forces that excite the propagating waves in silicon. Even though the calculation shown here is for an idealized CMUT which can not be realized, we believe it gives for many cases a conservative estimate of the degradation for reasonably designed CMUTs over a large bandwidth.

Table 12.1: Material properties of silicon and backing material

Material	Density (kg/m^3)	Longitudinal velocity (m/s)	Shear velocity (m/s)
Silicon	2340	8836	5294
Backing	9000	$2000 \left(1 + j\frac{0.08}{2}\right)$	$1000 \left(1 + j\frac{0.8}{2}\right)$

The material properties of the silicon and the backing used in the calculations are shown in Table 12.1. Silicon is an anisotropic material with elastic properties varying with crystal orientation. Isotropic approximations are normally used for silicon to make the calculations simpler. For micromachining of MEMS devices, (100) wafers are commonly used. For a (100) silicon wafer, Young's modulus of silicon varies from 130GPa to 170GPa depending on crystal orientations [HNK10]. Following [Liu12], silicon is considered here as an isotropic material with a Young's modulus of 160GPa and a Poisson's ratio of 0.22. Compared to an anisotropic model, the error in longitudinal velocity is within ±5% whereas the error in shear velocity is within ±12% with this approximation. The material properties of the backing material are chosen to match it fairly well acoustically to silicon for normal incidence of longitudinal waves. The longitudinal and shear loss factors for the backing material are chosen to be 0.08 and 0.8, respectively.

These loss factors account for absorption losses in the backing material. This will be discussed in more detail in section 12.4 describing modeling of loss for the grooved backing structure. The thicknesses of the silicon are chosen to be 60μm and 100μm in two investigated cases. When CMUTs on top of the silicon substrate are vibrating, longitudinal and shear waves are excited in various layers of the stack. Each layer is characterized by four waves: two longitudinal and two shear waves propagating or damped in positive and negative y-directions. The backing material in this section is assumed to be thick enough so that no waves are reflected back from the bottom of the backing. Therefore the backing layer is characterized by only two waves propagating or damped in negative y-direction as shown in Figure 12.2. Horizontal shear waves are not excited and not taken into account in the calculations. The amplitudes of particle velocities of different transmitted and reflected waves shown in Figure 12.2 are formulated by calculating particle velocities and stresses for each layer as described by Auld [Aul90]. Using continuity of velocities and stresses at the boundary between the two media, the equations are solved to calculate the amplitudes of reflected and transmitted longitudinal and shear waves in all layered media. Similar formulation has also been shown by Brekhovskikh [BB60] for calculations of reflection and transmission coefficients for elastic waves in solid layered media using a transfer matrix approach.

The amplitudes of particle velocities of different waves when CMUT array is excited at 25MHz frequency are calculated for the two different thicknesses of the silicon substrate for different steering angles. The ratio of amplitudes of the particle velocity in water to the exciting velocity, v_{ex}, of the idealized CMUT structure are shown in Figure 12.3. As the wave velocity in water is much smaller than the wave velocity in silicon, angles that the longitudinal and shear waves in the silicon make with the surface normal are much larger than the angle in water. At an angle of about $10°$ in water, the longitudinal wave in silicon propagates along the surface. For larger angles, the longitudinal wave in silicon is evanescent. At an angle of about $17°$, the shear wave will propagate along the surface. These angles are also known as the first and the second critical angles for the interface [RD00]. Dips are clearly observed at these angles for a thick silicon layer. For an angle slightly above the second critical angle, there is an existence of a wave propagating along the surface which is the SAW wave modified by the backing. This effect is more pronounced when the thickness of the silicon is increased further above 100μm. As the SAW is exponentially damped into the silicon substrate, the substrate should be thin compared to the characteristic wavelength in order to allow the acoustic backing layer

at the bottom of the substrate to absorb these waves. This could be seen in Figure 12.3 for 100μm substrate compared to 60μm substrate where the dip in the response above $17°$ steering angle is much reduced for 60μm substrate. The result shown in Figure 12.3 supports the conclusion made by Berg *et al.* [BR12] that a well backed 60μm silicon substrate may be used to carry CMUTs with a 25MHz center frequency.
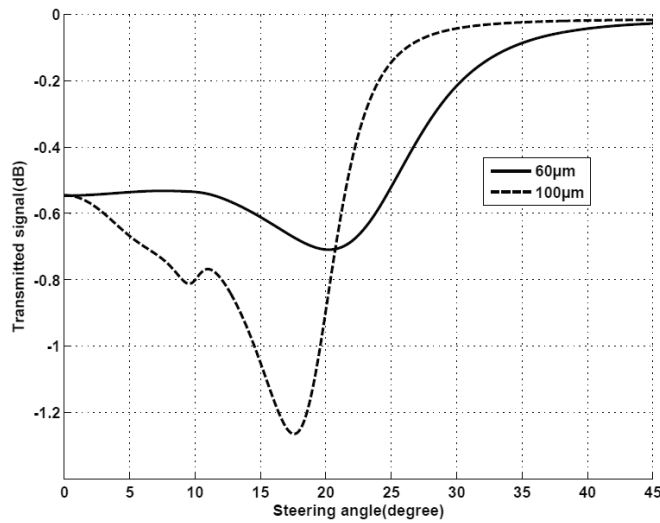
Figure 12.3: Amplitude of particle velocity in water compared to amplitude of exciting velocity, v_{ex}, of the CMUT structure when CMUTs on top of the silicon substrate are excited at 25MHz for two different thicknesses of silicon.

In this work we make grooves at the bottom of the backing material. Therefore we are interested in longitudinal waves transmitted into the backing material. As the shear waves have much higher losses than the longitudinal waves, they are properly attenuated in the backing. The amplitudes of longitudinal waves at the top of the backing are shown in Figure 12.4 for the two different thicknesses of the silicon as a function of steering angle in water. These are 20-30dB below the transmitted wave into water and the values will be even smaller when they are reflected back from the bottom as they are partly absorbed in the backing structure and partly scattered by the grooves. This also applies for the waves above $20°$ to $30°$ steering angle which are already small at the top of the backing. Therefore, for incidence angles above these values, the reflected waves will cause small perturbations only. This gives us an estimate of third term of (12.1). To
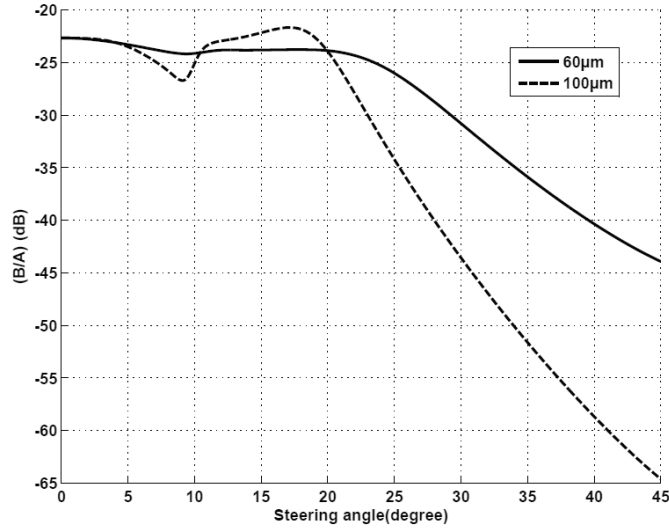
Figure 12.4: Amplitude of particle velocity of transmitted longitudinal wave at the top of the backing (B) compared to amplitude of particle velocity in water (A) for two different thicknesses of silicon versus steering angle in water.

get an estimate of first term of (12.1), similar calculation is repeated for a longitudinal wave excited at the top of the backing towards silicon and water. The transmitted longitudinal wave in the water is then calculated. The obtained results are shown in Figure 12.5 for the same two thicknesses of silicon. The velocity amplitude of the transmitted wave in water in this case is about 0-10dB below the input longitudinal wave velocity. This also decreases rapidly above 20° to 30° steering angle in water for both thicknesses of the silicon substrate.

The results shown here are for the idealized CMUT model. Referring to Figure 12.4, in a real CMUT there will be reactive forces accelerating the CMUT membrane and the fluid, and these forces will make the force on the fluid and the silicon different, not equal as assumed in the model. However as those forces are in quadrature with the radiation forces, the amplitude of the force on the substrate will not change much. As mentioned earlier the acoustic impedance of the CMUT around the center frequency is probably much smaller than assumed here in our model. This would mean that the CMUT layer is even easier to compress than we have assumed, and hence less movement will be transferred to the fluid compared to our result in Figure 12.5. This is probably the largest difference between our model and
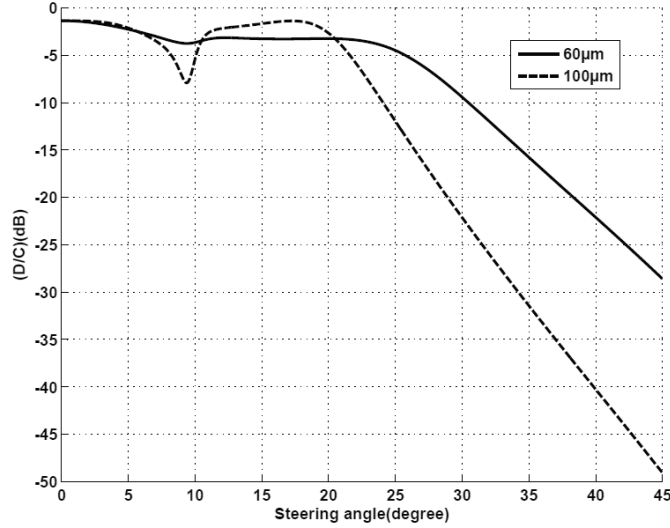
Figure 12.5: Amplitude of particle velocity of transmitted wave in water (D) compared to amplitude of particle velocity of longitudinal wave in the backing (C) for two different thicknesses of silicon versus steering angle in water.

a real CMUT structure.

From our calculation results we know that a 60μm or thinner silicon substrate works well for degradations due to SAW. The thicker substrates on the other hand are better for bulk wave reduction, especially at high steering angles, but they give degradations due to SAW. A 60μm or thinner silicon substrate is therefore recommended for our case. We then look at the combined echo suppression from the first and the last terms of (12.1) for a 60μm thick silicon substrate versus steering angle, $0°$ to $45°$, and frequency, 10MHz to 40MHz. This is shown in Figure 12.6. At high steering angles our goal of 40dB suppression is obtained from these terms alone at high frequencies. For steering angles up to $20°$ to $30°$, the combined echo suppression is 25-30dB for essentially the whole frequency range. This means that here an additional 10-15dB attenuation in the backing is required to avoid signal degradation in CMUT arrays. The second term of (12.1) should then provide this value for 100% bandwidth of the transducer for steering angles up to $20°$ to $30°$. In the following sections, we analyze the performance of the grooved backing structure for different steering angles and frequencies to get an estimate of the second term of (12.1).
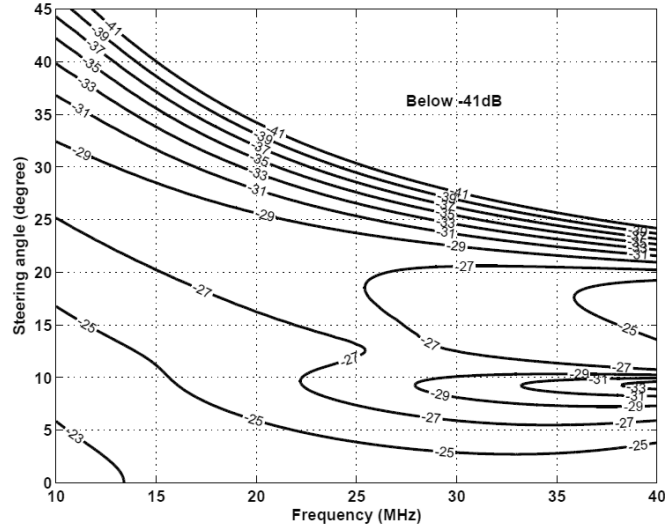
Figure 12.6: Combined echo suppression (dB) from the first and the last terms of (12.1) for 60μm thick silicon substrate as a function of frequency and steering angle in water, 2dB between contour lines. The steering angle is now shown as the y-axis in contrast to Figure 12.4 and Figure 12.5 to ease comparison with simulation results in the following sections.

12.3 Simulation of the grooved backing structure

Many physical phenomena in engineering and science are generally modeled by differential equations, but solving these equations by classical analytical methods is straightforward for a few simple geometries only. The finite element method (FEM) is a numerical approach by which these differential equations can be solved approximately for more complex geometries [OP92]. For the finite element simulation of the grooved backing structure, the structural mechanics module of COMSOL Multiphysics (version 3.5a) is used here. This module is suitable for analysis of components and subsystems when it is necessary to evaluate the deformations under loads [Com08]. The analysis is performed here for a 2D case. Plain strain formulation is used to study displacement, stress, and strain. A frequency response analysis is performed by solving the response from harmonic excitation.

The geometries for the grooved backing structures are defined as shown in Figure 12.7 and Figure 12.8. Two different designs are used, one is symmetric and the other is asymmetric. Neglecting effects of vertical surfaces and corners, both designs should provide the same response. They may

also have different advantages/disadvantages during manufacturing. The cross sectional shape of the grooves may also be important, and it surely is of great importance for the fabrication process. We have chosen simple rectangular grooves here, see Figure 12.7 and Figure 12.8. In [CR11], a fabrication process that provides groove walls with a tilt angle of 54.7° is described. Analysis shows that these grooves provides results that are very similar to those obtained here [CR11].

The backing material chosen here is a composite of epoxy and tungsten powder. To define the material properties of the backing, a model proposed by Devaney *et al.* [DL80] is used. Their theory is based on a self-consistent formulation of multiple scattering to estimate the mechanical properties of composite materials. Experiments have been performed with tungsten epoxy composites to study their mechanical properties for different volume fractions of tungsten [NLLP96, SNI05]. We have chosen the Devaney model because it shows good agreement with the experiments. To match the acoustic impedance of silicon using this model, the volume fraction of tungsten in the composite should be about 49%. In this work the volume fraction of tungsten is chosen to be 44% which is a value that could be achieved in practice using simple technique such as hand mixing [CR11]. For higher volume percentage of tungsten than this, the mixture becomes difficult to work with and it would require some special techniques to make the composite [BML^{+}04]. Using the volume percentage about 44% in the Devaney model, the longitudinal velocity for the composite is found to be about 2000m/s and the density is found to be about 9000kg/m^3. This yields a mechanical impedance of 18MRayl which is comparable to the mechanical impedance of silicon of about 20MRayl.

In this work the backing material is defined in terms of its Young's modulus, Poisson's ratio and density. We assume that the composite of tungsten and epoxy behaves as a homogeneous isotropic material. Using the values for velocity and density obtained from the Devaney model, the Young's modulus obtained for the composite is 24.3GPa with a Poisson's ratio of 0.33.

To emphasize the effect of the scattering from this type of structure, we have set the absorption losses in the composite material to zero in the initial calculations. The effect of finite losses within the composite material will be discussed in section 12.4. A uniform harmonic force is applied in the y-direction to excite a plane wave propagating in a direction normal to the bottom of the structure. In section 12.6, we will also deal with waves that are incident from oblique directions. To include both cases, a general expression is set up for the k-vector and its components as a function of incident angle.
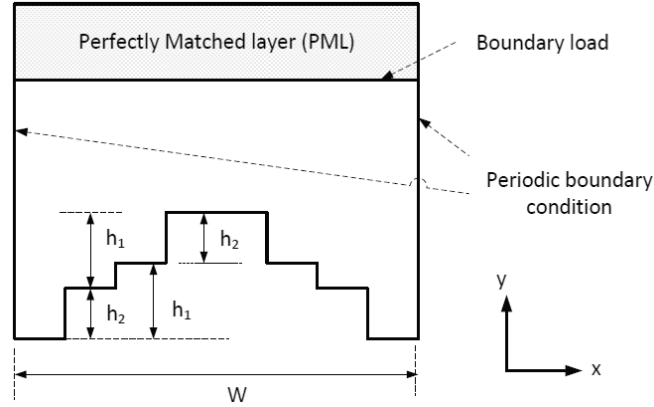
Figure 12.7: Grooved backing structure, symmetric design (figure is not to scale).
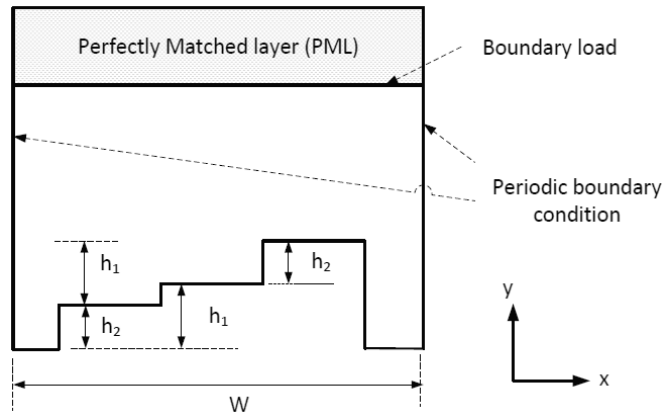
Figure 12.8: Grooved backing structure, asymmetric design (figure is not to scale).

The generalized term for the force could then be represented by $e^{-jk_x x - jk_y y}$, where k_x and k_y are the two components of the k-vector along the x and y directions, respectively.

The structure used here has two interwoven parallel grooves at its bottom. This means that the structure gives cancellation of the specular reflection for the normally incident waves when one of the groove heights h_1 or h_2, as shown in Figure 12.7 and Figure 12.8, is one quarter of the acoustic wavelength. The grooved structure is designed to give nulls in the reflection coefficient at the two frequencies 16MHz and 25MHz. This gives the values of h_1 and h_2 respectively as 31.25μm and 20μm with a longitudinal velocity

of 2000m/s. The period of the structure is chosen to be 600μm, which gives a cumulative total width of each step of 150μm. The height of the structure is taken to be 650μm and the thickness of a perfectly matched layer (PML), see next paragraph, is taken to be 400μm.

For the structures, our interest is to find how much of the incident longitudinal waves is specularly reflected, i.e. as plane waves with unchanged k_x vector. The top layer of the structure is assumed to be a non-reflecting boundary so that the specularly reflected wave and other backscattered waves are absorbed in it. To emulate the non-reflecting boundary, the perfectly matched layer (PML) is used on the top of the structure [Ber94]. In this work a PML layer with absorption in y-direction is used so that the reflected wave from the bottom surface would be absorbed in it. For frequency response analysis, a parameter called PML width is set to one wavelength in the medium so that the PML layer works properly [Com08]. The PML width is the actual modeled thickness of the PML, along the coordinate axis in which the PML absorbs. For obliquely incident waves, the PML width is divided by absolute value of the cosine of the incident angle to preserve the same amount of attenuation as the normally incident waves.

To make the calculations simpler, only one period of the structure is included in the simulation. Periodic boundary conditions are used to make the structure act as if it is infinite in x-direction. The bottom surface of the structure is kept free. This means that all incident waves will be reflected back into the medium without any loss at the interface.

In this work calculations are done in Fourier domain which makes calculations simpler due to the periodic excitation. If a property $P(x)$ is found to be

$$P(x) = P_p(x)e^{-jk_x x}, 0 < x < W \tag{12.2}$$

by this method, then $P(x)$ is given by the same expression for any x, provided that $P_p(x)$ is periodic with period W. Here k_x is the x-component of the exciting k-vector and W is the period of the structure in x-direction.

As $P_p(x)$ is periodic in x, it may be written as a sum of Fourier components as:

$$P_p(x) = \sum_n P_n(k_{nx})e^{-jk_{nx}x} \tag{12.3}$$

where $k_{nx} = \dfrac{2\pi n}{W}$ and n is any integer. Combining (12.2) and (12.3), we find the total k-vector in x-direction of the spectral component P_n of $P(x)$

to be

$$k_{nx} = k_x + \frac{2\pi n}{W} \qquad (12.4)$$

In this way the spectral components, P_n, can easily be calculated using the Fast Fourier transform (FFT) of one period of $P_p(x)$.

In the simulation, triangular elements are chosen to generate the finite element mesh. The mesh size is chosen such that a wavelength consists of at least 8 to 10 elements. All simulations are solved with standard settings for the solvers. The frequency is scanned from 10MHz to 40MHz which includes 100% bandwidth of the transducer. Although there are post-processing options available in COMSOL, Matlab is chosen for the post-processing of the result because of its greater flexibility. The output from the structural mechanics module are displacements in x and y directions from which particle velocities together with stresses in both directions could easily be obtained. The amplitudes of the waves traveling in different k-directions can be calculated at a cross section of the structure using the Fourier transform. When the amplitudes of waves traveling in different k-directions are found, the reflection coefficient of the waves from the grooved structure could easily be determined. This way of finding the waves traveling in different k-directions is also known as plane wave decomposition.

12.4   Modeling of acoustic attenuation

In order to study the attenuation provided solely by scattering from the grooves, the absorption loss in the medium is not included in the first part of the simulation. But for a realistic modeling of the backing structure, the acoustic attenuation due to the composite material should also be accounted for. Two models are widely used for damping, one is the *Rayleigh damping*, and the other is *Loss factor damping*. In the Rayleigh damping model the damping is defined in terms of mass and stiffness. But the challenge with this model is to choose values for different damping parameters that give a good representation of the actual damping [LG95]. Also the assumption of a damping factor that is proportional to both mass and stiffness have effects which are difficult to justify physically.

In this paper the loss factor damping model is used. As discussed earlier, the backing material is modeled with the help of Young's modulus and Poisson's ratio. In loss factor damping, complex values for Young's modulus and Poisson's ratio are used to represent the loss. This could be obtained

with complex values of longitudinal and shear velocities as [Kal07]:

$$
\begin{aligned}
{v_l}^2 &= {v_l'}^2(1 + j\eta_d) \\
{v_s}^2 &= {v_s'}^2(1 + j\eta_s)
\end{aligned}
\tag{12.5}
$$

where η_d and η_s are respectively the dilatational and the shear loss factors. The loss factor η_s is generally chosen to be higher than η_d as viscous loss is higher for shear waves than for longitudinal waves [KFCS00]. This is also the reason for not choosing the built-in loss factor model of COMSOL, which uses uniform losses for both longitudinal and shear waves [Com08, Kal07].

The backing material is assumed here to be an isotropic solid which means that the material properties could be described in terms of only two parameters, c_{12} and c_{44}, of the stiffness matrix. These parameters are also known as Lame's constants for an isotropic solid. They can easily be calculated from the velocities and the density of the material, and the Young's modulus and the Poisson's ratio for the material used are then found from the Lame's constants.

This model gives a value of acoustic attenuation which is linearly dependent on frequency. The backing structure used in this work is a composite material that consists of tungsten particles in an epoxy matrix. The acoustic property of such a composite material depends upon different manufacturing parameters such as working temperature, mixing, pressure, and the curing period [BML+04]. It also depends on shape, size and density of the inclusions [GGR90, WRC01]. Therefore, accurate determination of loss in this case is possible only by experimental methods. From our measurement results in [CR11], attenuation obtained in tungsten epoxy composite is about 30dB/mm around 20MHz for about 40% volume fraction of tungsten. The experimental determination of the loss variation with frequency is somewhat uncertain but it seems to vary less with frequency than assumed in this model. In this work, the values of the dilatational loss factor, η_d, and the shear loss factor, η_s, are chosen to be 0.08 and 0.8 respectively. These values provide an attenuation of about 1dB/mm MHz for the longitudinal waves. These values do not correspond to the measurements, but are close to them or lower for most of the frequency range used in the simulations.

12.5   Simulation results for a wave propagating normal to the bottom surface

In this case, the specular reflection of the waves from the grooved backing structure is calculated for normal incidence. After the problem is solved in

COMSOL, the displacements in x and y directions are obtained. It is also possible to obtain the values for velocities and stresses for the structure in these directions. After these parameters are found, the amplitudes of longitudinal waves propagating both in y and $-y$ directions can be calculated as follows. Referring to Figure 12.9, for a down propagating wave there will be a specularly reflected wave and other reflected waves with k_x vectors that are multiples of $\pm \left(\dfrac{2\pi}{W} \right)$. At a horizontal cross section of the structure above the grooves, the Fourier transform of the obtained velocities and stresses are computed. This gives the amplitudes of waves with different k-vectors in x-direction. The amplitudes of longitudinal waves with $k_x = 0$ propagating in upward and downward direction are calculated from the following equation:

$$\left[\begin{array}{c} v_y \\ T_{yy} \end{array} \right] = \left[\begin{array}{cc} 1 & 1 \\ Z_l & -Z_l \end{array} \right] \left[\begin{array}{c} A_l \\ B_l \end{array} \right] \tag{12.6}$$

where A_l and B_l are the amplitudes of waves propagating respectively in downward and upward directions in the grooved structure, v_y is the zeroth component of the FFT of the particle velocity in the y direction, T_{yy} is the zeroth component of the FFT of the longitudinal stress in the y-direction, and Z_l is the value of the longitudinal acoustic impedance of the backing material. The ratio of the amplitudes $\left(\dfrac{B_l}{A_l} \right)$ gives the value of the specular reflection coefficient at a particular frequency. The process is repeated for all frequencies and the results obtained from the simulation for the structures are shown in Figure 12.10. The specular reflection obtained for both symmetric and asymmetric designs are almost identical, except the exact value of specular reflection at the two chosen cancellation frequencies.

The obtained results match well with theoretical calculations shown earlier for such a structure using the simple delay difference method as described in [CR09]. For the grooved structure, besides two nulls in the frequency range, the specular reflection is less than -15dB in the range of frequencies from 12MHz to 28MHz. The frequency range where added attenuation is available depends on the chosen cancellation frequencies. To make this frequency range even broader, nulls can be chosen at more frequencies.

To estimate the attenuation due to the grooved structure only, absorption loss in the material is not taken into account in this case. This means that the grooved structure by itself is capable of providing 15dB or more attenuation in the frequency range of 12MHz to 28MHz. In section 12.4, we discussed how absorption loss due to the tungsten epoxy composite could
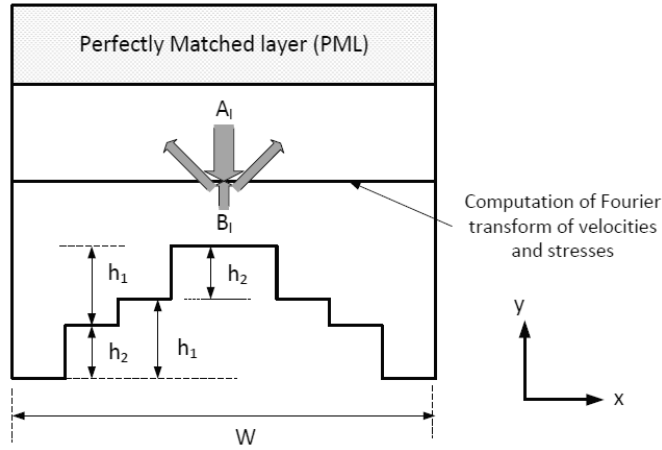
Figure 12.9: Calculation of specular reflection coefficient for the grooved backing structure.
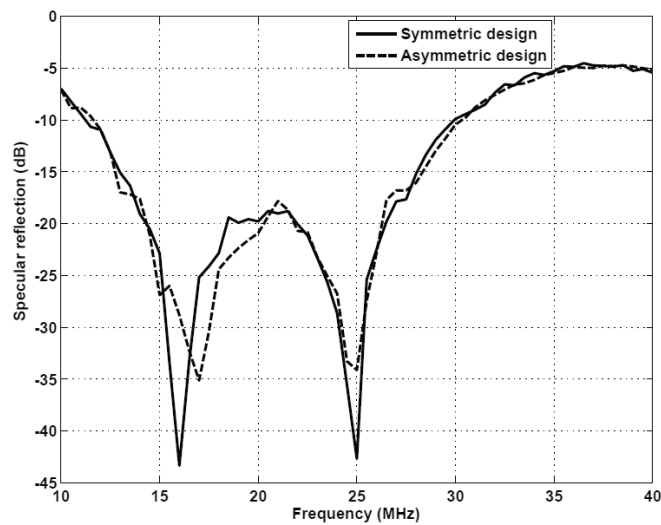
Figure 12.10: Specular reflection from grooved structure for normal incidence designed to give nulls at 16MHz and 25MHz without absorption losses.

be included in the simulation. The results for the grooved backing structures including the loss factors are shown in Figure 12.11. The reflection is evaluated at a height of 150μm above the lowest surface in the backing. The results are very similar for both designs in this case as well. The loss model used here depends linearly on frequency. That is why loss is observed to increase with increasing frequency. But the nulls in the specular reflection are
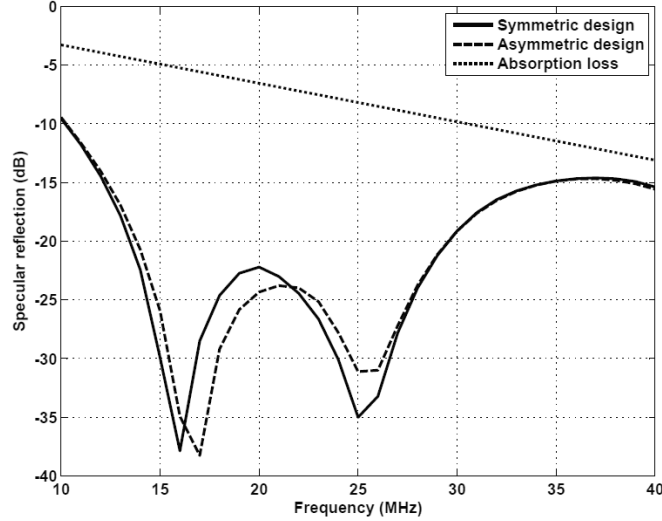
Figure 12.11: Specular reflection from grooved structure for normal incidence including the absorption loss with loss factors $\eta_d = 0.08$ and $\eta_s = 0.8$ evaluated at a height of 150μm above the lowest surface in the backing.

still present at roughly the same frequencies. It is clear from Figure 12.11 that the grooved structure provides attenuation of about 15dB and more for 100% bandwidth of the CMUT transducer with center frequency 25MHz, and a maximum thickness of 150μm.

We can see that the addition of absorption loss and scattering loss does not exactly yield the total attenuation as shown in Figure 12.11. This is because the absorption loss shown here is for a 150μm thick epoxy tungsten composite without grooves, whereas the actual thickness changes due to the presence of the grooves.

12.6   Simulation results for oblique incidence

Section 12.5 discussed waves at normal incidence. In this section, the same process is repeated for angles of incidence different from zero. For a longitudinal wave incident on a plane free boundary, there will be a reflected longitudinal wave as well as a reflected shear wave when the angle of incidence is different from zero. But due to the presence of grooves at the bottom surface, the wave is also converted into longitudinal and shear waves with k-vectors in the transverse direction which are multiples of $\pm \left(\dfrac{2\pi}{W} \right)$ in addition to the k_x of the incoming wave. Here, W is the period of the

structure in x-direction. The calculation shown below gives the wave that is specularly reflected from the structure for different incident angles. It also includes the absorption loss in the backing material. The material loss factors used are the same as in the earlier case.

The plane strain formulation in the structural mechanics module of COMSOL solves the waves for displacements in x and y directions. From this solution, particle velocity and stress in both directions can be computed. The solid medium here is the backing material with known material properties and density. If v_x and v_y are particle velocities in x and y directions, the longitudinal stress, T_{yy}, and the shear stress, T_{xy}, are given by [Aul90] :

$$T_{yy} = \frac{c_{12}}{j\omega}\frac{\partial v_x}{\partial x} + \frac{c_{11}}{j\omega}\frac{\partial v_y}{\partial y} \tag{12.7}$$

$$T_{xy} = \frac{c_{44}}{j\omega}\left(\frac{\partial v_y}{\partial x} + \frac{\partial v_x}{\partial y}\right) \tag{12.8}$$

Using (12.7) and (12.8) the stresses T_{xy} and T_{yy} in the material are calculated. The velocities and the stresses may be represented in a matrix form as follows:

$$\begin{bmatrix} v_y \\ v_x \\ T_{xy} \\ T_{yy} \end{bmatrix} = \begin{bmatrix} -\cos\theta_l & \cos\theta_l & -\sin\theta_s \\ \sin\theta_l & \sin\theta_l & \cos\theta_s \\ \frac{c_{44}\sin 2\theta_l}{v_l} & -\frac{c_{44}\sin 2\theta_l}{v_l} & -Z_s\cos 2\theta_s \\ -\frac{c_{11}\cos^2\theta_l + c_{12}\sin^2\theta_l}{v_l} & -\frac{c_{11}\cos^2\theta_l + c_{12}\sin^2\theta_l}{v_l} & -Z_s\sin 2\theta_s \end{bmatrix} \begin{bmatrix} A_l \\ B_l \\ B_s \end{bmatrix} \tag{12.9}$$

Here θ_l is the incident angle, θ_s is the angle of the reflected shear wave with the k-vector component k_x in x-direction, A_l is the amplitude of the incident longitudinal wave, B_l is the amplitude of reflected longitudinal wave, B_s is the amplitude of the reflected shear wave, v_l is the longitudinal wave velocity, Z_s is shear acoustic impedance, and c_{11}, c_{12} and c_{44} are the stiffness parameters of the backing material. The angle of the reflected shear wave, θ_s, is given by $\sin^{-1}\left(\frac{v_s}{v_l}\sin\theta_l\right)$, where v_s is the shear wave velocity in the backing material.

To solve the problem, oblique waves are excited with the help of k-vectors in x and y directions. The waves are excited using the "boundary load" feature of COMSOL. The boundary conditions and the solver settings are similar to that for normal incidence case. After solving the problem, the displacements in the x and y directions are obtained at each frequency, and the corresponding stresses in x and y directions are computed. These

parameters are found for a cross section of the geometry above the grooves as in the case of normal incidence, where the reflection coefficient is to be evaluated. The Fourier transform of particle velocities and stresses are obtained at this cross section. But before taking the Fourier transform, the spatial velocities and stresses are multiplied by a factor $e^{jk_x x}$. For the calculation of the reflection coefficient over a range of frequencies, (12.9) is solved and the ratio $\left(\dfrac{B_l}{A_l}\right)$ is obtained for each frequency. The parameters on the left hand side of (12.9) are all the zeroth component of the FFT of velocities and stresses obtained over a cross section of the structure above the grooves. These equations also give the result for waves propagating in normal direction to the bottom surface when the value of the incident angle, θ_l, is set to zero.
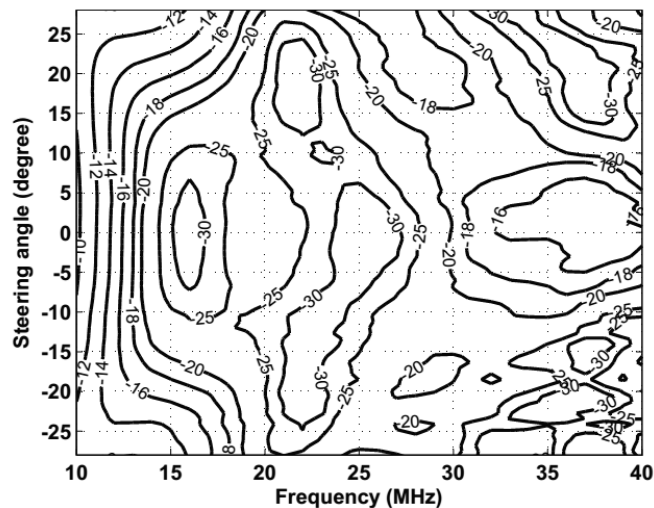
Figure 12.12: Specular reflection (dB) from the grooved backing structure for different steering angles in water with a period of 600μm (symmetric design), contour lines below -30dB are not shown in the figure.

The results obtained for different incidence angles for the frequency range are shown in Figure 12.12 and Figure 12.13 respectively for symmetric and asymmetric designs. To ease the comparison with calculations in section 12.2, the results are shown for steering angles in water, not in the backing, as used in (12.9). Neglecting effects of vertical surfaces and corners, both designs should work in the same manner. They have similar responses for waves propagating normal to the bottom surface of the structure. But they have slightly different responses for the oblique inci-
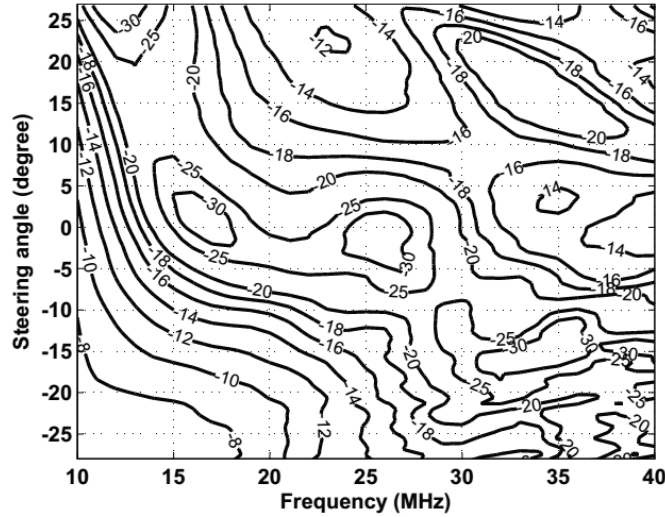
Figure 12.13: Specular reflection (dB) from the grooved backing structure for different steering angles in water with a period of $600\mu m$ (asymmetric design), contour lines below -30dB are not shown in the figure.
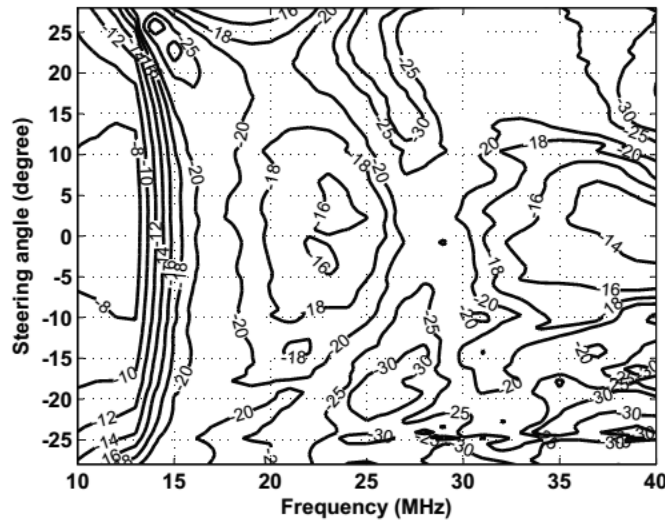
Figure 12.14: Specular reflection (dB) from the grooved backing structure for different steering angles in water with a period of $150\mu m$ (symmetric design), contour lines below -30dB are not shown in the figure.

dence case. As seen from the figures, the specular reflection obtained for small steering angles are close to that of normal incidence. But as the
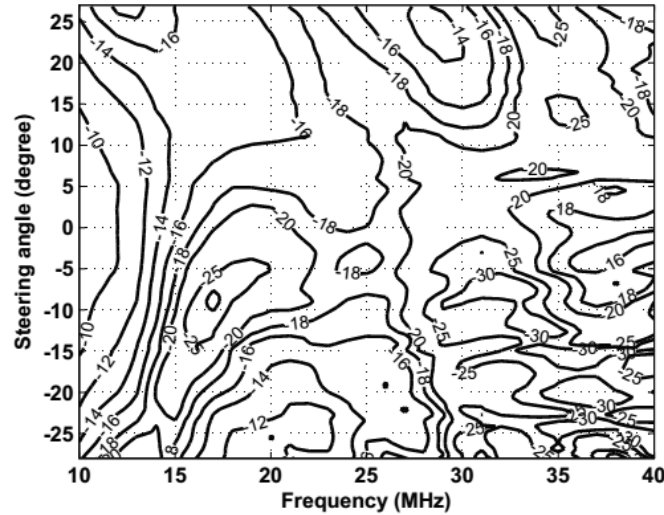
Figure 12.15: Specular reflection (dB) from the grooved backing structure for different steering angles in water with a period of 150μm (asymmetric design), contour lines below -30dB are not shown in the figure.

steering angle becomes larger, the nulls in the specular reflection disappear. It can also be seen from the figures that the symmetric design performs slightly better than the asymmetric design. Unlike the asymmetric design, the symmetric design gives a result that is symmetric with respect to the steering angle, except at certain points which is due to numerical errors associated with the finite element analysis. For both designs, for steering angles smaller than $\pm 15°$, the specular reflection is not distinctly different from the results obtained for normal incidence. For larger steering angles the deviation is more pronounced. Multiple reflections at different steps in the grooved structure could be one of the reasons for this. Also conversion of longitudinal waves into shear waves could take place at the backing-air interface for larger input angles. A careful investigation of the results shows that there is an additional attenuation for all steering angles compared to the structures without grooves.

The performance of the grooved structure is studied for different periods smaller than 600μm in the frequency range from 10MHz to 40MHz. For this frequency range the performance is essentially the same when the period is reduced down to 200μm. The performance becomes somewhat different as the dimensions become smaller than 200μm. The results obtained with a period of 150μm for the frequency range are shown in Figure 12.14 and Figure 12.15 respectively for symmetric and asymmetric designs. The

performance of the grooved structure is still acceptable at 150μm, but it is more random. For smaller periods, the asymmetric structure has a better performance. This seems reasonable since the symmetric design divides the period into smaller parts compared to the asymmetric design. If we add the the specular reflection shown in Figure 12.14 and Figure 12.15 to the combined echo suppression from Figure 12.6, we find that our 40dB goal is obtained except for a small region at low frequency band edge around broadside for all steering angle below 45° and for the bandwidth from 12.5MHz to 37.5MHz. Already at 15MHz the suppression at broadside is at 40dB. This is also true for thinner silicon substrates than 60μm.

The simulations shown here are valid for structures that are infinite in lateral directions. It is clear that for the grooved backing structure to perform well, there should be a balance in cumulative total width of each step [CR09]. However, real CMUT transducers will be limited in lateral dimensions. To perform like an infinite structure it is therefore important that the lateral period is small. As an example let us look at an array which is 1.5mm wide. This equals 25 acoustic wavelengths in water at 25MHz. Here we would have 10 periods across the aperture using the structure with 150μm period with the properties shown in Figure 12.14 and Figure 12.15. Further, somewhat dependent on the shape of the aperture, the grooves in the backing could be tilted relative to the edges of the aperture. In this case we believe that the backing will provide the required balance in cumulative width or area of each step in groove depth with sufficient accuracy to perform almost as the infinite structure.

12.7 Discussion and Conclusion

In this paper we discuss a grooved backing structure for CMUT transducers. The grooves are designed to give cancellation of specular reflection at two frequencies, 16MHz and 25MHz. It is shown that the grooves provide an attenuation of about 10dB or more for essentially the whole 100% bandwidth of the transducer. This attenuation is due to scattering by the grooves which comes in addition to what the epoxy tungsten composite provides by itself. The additional attenuation together with absorption loss of the composite is adequate to avoid signal degradation in CMUT transducers.

In section 12.6, we have shown that the grooved structure provides a total attenuation which is not much different from what is obtained for normal incidence when the steering angle in the fluid medium is within 0-15° to the surface normal. The results are slightly different for symmetric and asymmetric designs, but in both cases there is an attenuation of about

10-20dB or more for the entire frequency range. The grooved structure also provides total attenuation of about 10-20dB or more for steering angles larger than 15° even though the response is different from that of normal incidence. From section 12.2 we know that the waves that reach into the backing from the CMUT transducer with significant power are mainly in the range of 0-20° to 0-30° steering angle in the fluid medium. Most of these fall in the region where the grooved structure performs well. Thus we conclude that the grooved backing structure always provides an additional attenuation to the waves that are normal to as well as in oblique directions to the bottom of the backing structure when they are used with CMUT transducers in practical applications.

This means that a thick backing layer for CMUT transducers could be replaced by a backing layer with grooves at its bottom surface which provides an equal amount of attenuation with a reduced thickness. This makes the CMUT transducers with grooved backing structure more useful in applications like IVUS, where there is little space available under the transducer.

This work, however, has some limitations. The grooved backing structure is considered to be infinite and uniform in the direction of the grooves in the calculations, and the acoustic beam is always normal to the grooves. This allows us to use 2D FEM simulation which has moderate requirements on computational resources. But it also means that it is not possible to study the beams tilted along the grooves.

Acknowledgment

References

[Aul90]   B.A. Auld. *Acoustic Fields and Waves in Solids*. Krieger Publishing Company, 1990.

[BB60]   L.M. Brekhovskikh and R.T. Beyer. *Waves in layered media*, volume 4. Academic press New York, 1960.

[Ber94]   Jean Pierre Berenger. A perfectly matched layer for the absorption of electromagnetic waves. *Journal of Computational Physics*, 114(2):185 – 200, 1994.

[BML+04]   C.E. Baumgartner, D.M. Mills, R.S. Lewandowski, L.S. Smith, and D.G. Wildes. Backing material for micromachined ultrasonic transducer devices, dec. 2004. US Patent 6,831,394.

[BR05]   S. Berg and A. Rønnekleiv. Backing requirements for CMUT arrays on silicon. In *Ultrasonics Symposium, 2005 IEEE*, volume 4, pages 1952 – 1955, sept. 2005.

[BR09]   S. Berg and A. Rønnekleiv. Challenges with acoustic backing of CMUT arrays on silicon with integrated electronics. In *Ultrasonics Symposium (IUS), 2009 IEEE International*, pages 980 –983, sept. 2009.

[BR12]   S. Berg and A. Rønnekleiv. Acoustic backing in 3D integration of CMUT with front-end electronics. *Ultrasonics, Ferroelectrics and Frequency Control, IEEE Transactions on*, 59(7):1537 – 1549, july 2012.

[CCS+05]   G. Caliano, A. Caronti, A. Savoia, C. Longo, M. Pappalardo, E. Cianci, and V. Foglietti. Capacitive micromachined ultrasonic transducer (cMUT) made by a novel "reverse fabrication process". In *Ultrasonics Symposium, 2005 IEEE*, volume 1, pages 479 – 482, sept. 2005.

[CCS+08]   A. Caronti, A. Coppa, A. Savoia, C. Longo, P. Gatta, B. Mauti,
           A. Corbo, B. Calabrese, G. Bollino, A. Paz, G. Caliano, and
           M. Pappalardo. Curvilinear capacitive micromachined ultra-
           sonic transducer (CMUT) array fabricated using a Reverse pro-
           cess. In *Ultrasonics Symposium, 2008. IUS 2008. IEEE*, pages
           2092 –2095, nov. 2008.

[Che12]   J David N Cheeke. *Fundamentals and applications of ultrasonic
           waves*. CRC PressI Llc, 2012.

[Com08]   Comsol AB. *Comsol Multiphysics 3.5, users guide*, 1998-2008.

[CR09]   K.R. Chapagain and A. Rønnekleiv. Minimizing the bottom re-
           flection in ultrasonic CMUT transducer backing using low pro-
           file structuring. In *Ultrasonics Symposium (IUS), 2009 IEEE
           International*, pages 430 –433, sept. 2009.

[CR11]   Kamal Raj Chapagain and Arne Rønnekleiv. Measurement of
           the added specular reflection attenuation by using a grooved
           bottom surface in the backing of CMUTs. In *Ultrasonics Sym-
           posium (IUS), 2011 IEEE International*, pages 1004 –1007, oct.
           2011.

[DGK06]   F.L. Degertekin, R.O. Guldiken, and M. Karaman. Annular-ring
           CMUT arrays for forward-looking IVUS: transducer character-
           ization and imaging. *Ultrasonics, Ferroelectrics and Frequency
           Control, IEEE Transactions on*, 53(2):474 –482, feb. 2006.

[DL80]   A.J Devaney and H. Levine. Effective elastic parameters of ran-
           dom composite. *Applied Physics Letters*, pages 377–379, 1980.

[DWB+05]   C. Daft, P. Wagner, B. Bymaster, S. Panda, K. Patel, and
           I. Ladabaum. cMUTs and electronics for 2D and 3D imaging:
           monolithic integration, in-handle chip sets and system implica-
           tions. In *Ultrasonics Symposium, 2005 IEEE*, volume 1, pages
           463 – 474, sept. 2005.

[GGR90]   Martha G Grewe, T.R. Gururaja, and Thomas R.Shrout.
           Acoustic properties of particle/polymer composites for ultra-
           sonic transducer backing applications. *IEEE transactions on
           Ultrasonics, Ferroelectrics and Frequency Control*, 37:506–514,
           1990.

[HKY94]   M.I. Haller and B.T. Khuri-Yakub. A surface micromachined electrostatic ultrasonic air transducer. In *Ultrasonics Symposium, 1994. Proceedings., 1994 IEEE*, volume 2, pages 1241 – 1244 vol.2, 31 1994-nov. 3 1994.

[HNK10]   Matthew A Hopcroft, William D Nix, and Thomas W Kenny. What is the young's modulus of silicon? *Journal of Microelectromechanical Systems*, 19(2):229–238, 2010.

[JDC+98]   X.C. Jin, F.L. Degertekin, S. Calmes, X.J. Zhang, I. Ladabaum, and B.T. Khuri-Yakub. Micromachined capacitive transducer arrays for medical ultrasound imaging. In *Ultrasonics Symposium, 1998. Proceedings., 1998 IEEE*, volume 2, pages 1877 –1880 vol.2, 1998.

[Kal07]   Anthony J. Kalinowski. Acoustic transparency of non-homogeneous plates (with repeating inclusions) using periodic structures methodology. In *Proceedings of the COMSOL Conference, Boston*, 2007.

[KFCS00]   Lawrence E. Kinsler, Austin R. Frey, Alan B. Coppens, and James V. Sanders. *Fundamentals of Acoustics*. John Wiley and Sons Inc., Newyork, USA, 2000.

[KYEY08]   Butrus T. Khuri-Yakub, Arif S. Ergun, and Goksen Yaralioglu. A capacitive membrane ultrasonic transducers with reduced bulk wave generation and method, 2008.

[LG95]   Man Liu and D.G. Gorman. Formulation of Rayleigh damping and its extensions. *Computers & Structures*, 57(2):277 – 285, 1995.

[Liu12]   Chang Liu. *Foundation of MEMS, second edition*. Pearson Education limited, England, 2012.

[LJS+98]   I. Ladabaum, Xuecheng Jin, H.T. Soh, A. Atalar, and B.T. Khuri-Yakub. Surface micromachined capacitive ultrasonic transducers. *Ultrasonics, Ferroelectrics and Frequency Control, IEEE Transactions on*, 45(3):678 –690, may 1998.

[LW00]   I Ladabaum and Paul A. Wagner. Silicon substrate ringing in microfabricated ultrasonic transducers. *IEEE Ultrasonic Symposium*, pages 943–946, 2000.

[LW05]   Igal Ladabaum and Paul A. Wagner. Microfabricated ultrasonic transducer with suppressed substrate modes, 2005.

[MRW06]   K. Midtbø, A. Rønnekleiv, and D.T. Wang. Fabrication and characterization of CMUTs realized by wafer bonding. In *Ultrasonics Symposium, 2006. IEEE*, pages 938 –941, oct. 2006.

[NLLP96]   T.N. Nguyen, M. Lethiecq, F. Levassort, and L. Pourcelot. Experimental verification of the theory of elastic properties using scattering approximations in (0-3) connectivity composite materials. *Ultrasonics, Ferroelectrics and Frequency Control, IEEE Transactions on*, 43(4):640 –645, jul 1996.

[OP92]   Neils Ottosen and Hans Petersson. *Introduction to the finite element method*. Pearson Education limited, 1992.

[PTBR05]   T.L. Proulx, D. Tasker, and J. Bartlett-Roberto. Advances in catheter-based ultrasound imaging intracardiac echocardiography and the ACUSON AcuNav^{TM} ultrasound catheter. In *Ultrasonics Symposium, 2005 IEEE*, volume 1, pages 669 – 678, sept. 2005.

[RD00]   Daniel Royer and Eugene Dieulesaint. *Elastic Waves in Solids, Volume I*. Springer, 2000.

[SC84]   C.M. Sayers and C.E.Tait. Ultrasonic properties of transducer backings. *Ultrasonics*, 22:57–70, 1984.

[Sie]   Siemens Healthcare System. ACUSON AcuNav^{TM}Ultrasound Catheter.

[SLA$^+$96] H. T. Soh, I. Ladabaum, A. Atalar, C. F. Quate, and B. T. Khuri-Yakub. Silicon micromachined ultrasonic immersion transducers. *Applied Physics Letters*, 69(24):3674–3676, 1996.

[SNI05]   Keisuke Sugawara, Morimasa Nishihira, and Kazuhiko Imano. Experimental study of acoustic properties of (0-3) composite materials for intermediate layer or backing of ultrasonic transducers. *Journal of Applied Physics*, 44:4347–4349, 2005.

[WRC01]   Haifeng Wang, Tim Ritter, and Wenwu Cao. High frequency properties of passive materials for ultrasonic transducers. *IEEE transactions on Ultrasonics, Ferroelectrics and Frequency Control*, 48:78–84, 2001.

[WZY$^+$08] Ira O Wygant, Xuefeng Zhuang, David T Yeh, Omer Oralkan, A Sanli Ergun, Mustafa Karaman, and Butrus T Khuri-Yakub. Integration of 2d cmut arrays with front-end electronics for volumetric ultrasound imaging. *Ultrasonics, Ferroelectrics and Frequency Control, IEEE Transactions on*, 55(2):327–342, 2008.